

A Flex-Rigid, Multi-Channel ECoG Microelectrode Array: Reliable Electrical Contact & Long-Term Stability in Saline

Elena Tolstosheeva



University of Bremen 2017

Entwicklung hochflexibler
Multikanal-Mikroelektroden für die
Neuroprothetik:
zuverlässige Aufbau & Verbindungstechnik
und
langfristige Stabilität in Kochsalzlösung

Vom Fachbereich für Physik und Elektrotechnik
der Universität Bremen

Zur Erlangung des akademischen Grades eines

Doktor-Ingenieur (Dr.-Ing.)

genehmigte Dissertation

von

Dipl.-Ing. Elena Tolstosheeva

aus Lipezk, Russland

Referent: Prof. Dr.-Ing. Walter Lang

Korreferent: Prof. Dr. rer. nat. Andreas Kreiter

Eingereicht am: 14. 09. 2017

To My Mother

Acknowledgments

”If I have seen further it is by standing
on the shoulders of giants.”

Isaac Newton

Herewith I would like to thank all who supported me throughout the making of this Thesis:

- Prof. Lang for the opportunity to work on this PhD project, and for his overall support,
- Prof. Kreiter, Sunita Mandon, Dieter Gauck and Victor Gordillo-Gonzalez for the fruitful brainstorming and hands-on experience on noiseless measurements,
- Volker Biefeld for the clean-room support and overall advice,
- Mohammad Shafi and Kai Syrnik for advices on photolithography and electroplating,
- Ludger Kempen for the very first DRIE etch,
- Eva-Maria Meyer for sputtering and SEM-imaging,
- Ibrahim Ersöz and Ingrid Michels for wafer-sawing and wire-bonding,
- Ismail Baser for the constant supply of electrical components,
- Kirstin Hoppe for the precautions on wet chemical etching,
- Adam Sklorz for the discussions on automation of electrical tests,
- Safir Issa for motivating me to start well in advance with the writing,
- Azat Ibragimov, Denis Petrov and Dmitriy Boll for the discussions on analytic calculations,
- Anderas Schander, Tobias Tessmann, Thomas Hertzberg, Jan-Peter Hoffmann, Jonas Pistor, Tim Schellenberg, David Rothermund and Dieter Gauck for the neuro-meetings,
- Praveen Pratti, Mahmuda Akhtar, Maryam Kahali, Benjamin Schittowski and Marcus Spence, for their student projects,
- Kai Burdorf for his true-to-life explanations of physical phenomena,
- Protron Mikrotechnik GmbH for the clean-room support,
- Harrie Maas for the priceless microfabrication tips and motivation,
- My Father, my Family and Friends for their constant Love.

Abstract

An Electrocorticography Micro-Electrode Array (ECoG MEA) is a promising signal-acquisition solution for weakly-invasive brain-computer interfaces. This PhD Thesis proposes a microfabrication scheme for a high-density ECoG MEA and investigates its long-term performance in saline.

The ECoG device contains 124 circular electrodes of 100, 300 and 500 μm diameters, situated on concentric hexagons (150 mm^2 total recording area). The reference electrode, situated beside them, is to be bent to the array backside to become a skull-facing electrode (2.5 mm^2 surface area). Metallization paths connect the electrodes to the assembly pads of 4×32 SMD Omnetics connectors.

The ECoG device was realized as a polyimide-metal-polyimide stack on a silicon wafer. A DRIE process shaped a silicon interposer out of the carrier wafer, serving as mechanical platform for the assembly of fine-pitch electrical connectors.

Electrical characterization was performed by means of electrochemical impedance spectroscopy. The electrode impedance scaled with electrode area. The strength of the solder joints was tested by means of pull tests. Electrical and mechanical tests revealed that removing the bottom polyimide from the solder-joint area enables a more reliable electrical contact.

The array was implanted on the primary visual cortex (V1) of a macaque and recorded natural electrophysiological signals: the larger the electrode, the larger the signal. The skull-facing reference electrode provided signals of greater average Power Spectral Density (PSD) than common average referencing. However, the onset of parasitic short-circuits formation was encountered ca. 3-4 months after implantation.

Accelerated soak tests were performed on planar-capacitor IDE structures to simulate the formation of parasitic short-circuits. The influence of curing, adhesion and sterilization on the water-barrier properties of polyimide and parylene coatings was monitored. Based on the results, a new ECoG MEA was fabricated and stored under accelerated soak conditions.

The proposed ECoG MEA can be beneficial for the design, microfabrication and long-term stability of future flexible microdevices.

Zusammenfassung

Elektrokorticale Mikroelektroden-Arrays (ECoG MEAs) können in Zukunft als wenig invasive Signalerfassungseinheiten für Gehirn-Computer-Schnittstellen dienen. Diese Arbeit präsentiert ein mikrosystetechnisches Herstellungsverfahren für ein hochdichtes ECoG-MEA und untersucht deren Langzeitstabilität in Salzwasser.

Das ECoG Array hat 124 kreisförmige Elektroden (100, 300 und 500 μm Durchmesser), die auf konzentrischen Hexagonen (150 mm^2 Gesamtfläche) positioniert sind. Die Referenzelektrode, die sich neben dem größten Hexagon befindet, wird auf die Array-Rückseite gebogen (skull-facing, 2.5 mm^2 Gesamtfläche). Die Elektroden sind mit metallisierten Leiterbahnen mit 4×32 SMD Stecker-Pads verbunden.

Das Array wird als Polyimid-Metall-Polyimid Schichtsystem auf einem Siliziumwafer aufgebaut. Eine DRIE-Ätzung verwandelt das Elektrodenarray in eine freistehende Membran, die durch flexible Bänder mit dem Wafer verbunden ist. Dies ermöglicht die monolithische Integration eines Silizium-verstärkten Interposers in eine hochflexible Folie.

Die Elektroden wurden durch elektrochemische Impedanzspektroskopie charakterisiert. Die Elektrodengröße spiegelt sich in dem gemessenen Impedanzbetrag wieder. Mechanische und elektrische Tests zeigen, dass das Entfernen der unteren Polyimid-Schicht von dem Interposer-Bereich zu einer wesentlichen Kontaktverbesserung führt.

Das Array wurde über dem primären visuellen Kortex (V1) eines Makaken implantiert und ermöglichte die Aufnahme natürlicher elektrophysiologischen Signale: je größer die Elektrode, desto größer das Signal. Die Referenzelektrode nahm Signale mit größerer Leistungsdichte (γPSD) als Common-Average-Referencing auf. Jedoch wurde eine steigende Anzahl an kurzgeschlossenen Elektroden ca. 3-4 Monate nach der Implantation beobachtet.

Dieses Degradationsverhalten wurde im Labor mit Accelerated-Aging-Tests auf Interdigital-Mikrostrukturen untersucht. Der Einfluss von Aushärten, Haftung und Sterilisation auf die Wasserbarriereigenschaften von Polyimid und Parylen wurde untersucht. Basierend auf den Ergebnissen wurde ein neues ECoG Array hergestellt und in einem Accelerated-Aging-Test monatelang auf Kurzschlüsse untersucht.

Die Ergebnisse dieser Arbeit könnten das Design, Mikroherstellung und Langzeitstabilität zukünftiger flexibler Mikrosystemen vorantreiben.

Contents

1	Physiology of Visual Perception	3
2	Vision of a Cortical Interface	9
2.1	Vision of Attention-Driven BCI	9
2.2	Recording of Brain Rhythms	11
2.3	Origin of ECoG Potentials	13
2.4	ECoG Recordings for Attention-Driven BCIs	17
3	Microfabrication of ECoG MEAs	23
3.1	State of the Art	24
3.2	Flex-Rigid Microfabrication Concept	27
3.3	Mechanics of Flexible Materials	28
3.4	Electrode-Electrolyte Interface	32
3.5	Scope of This Thesis	37
4	A Multi-Channel, Flex-Rigid ECoG MEA for Visual Cortical Interfacing	41
4.1	Design	42
4.2	Development of Fabrication Process	47
4.2.1	Microfabrication	47
4.2.2	SMD Assembly	50
4.3	Troubleshooting: a Reliable Electrical Contact	52
4.4	Final Fabrication Flow	54
4.5	In-Vitro Characterization of ECoG MEA Electrodes	58
4.6	In-Vivo Characterization of ECoG MEA	61
4.7	Summary	65
5	Long-Term Stability of BPDA-PPD Polyimide in Saline	67
5.1	State of the Art	68
5.2	IDE Sensors: Materials & Methods	75

5.2.1	Theory: Choice of Optimal Parameters	76
5.2.2	Design & Microfabrication	90
5.2.3	Results	95
5.3	ATR-FTIR Analysis of Polyimide Foils	101
5.4	XRD Analysis of Polyimide Foils	101
5.5	Water-Vapour Permeability of Polyimide Foils	104
5.6	Summary	104
6	Long-Term Stability of ECoG MEAs	107
6.1	Long-Term Stability of ECoG MEA In-Vitro	107
6.2	Long-Term Stability of ECoG MEA In-Vivo	110
7	Summary & Outlook	111
	Bibliography	115
	Appendices	129
A	ECoG MEA's Design	i
A.1	Bending of a Beam in an Arc	i
A.2	Electrode Layout of the ECoG MEA	iii
B	ECoG MEA's Microfabrication Flow	v
C	Resist Reflow	ix
D	Pull Tests	xi
E	Long-Term Stability of Polyimide	xiii
E.1	E-Field Distribution of Coplanar-Plate Capacitor	xiii
E.2	Hands on Measurements of IDE sensors	xiv
E.3	Long-term Stability of Parylene vs. Polyimide	xv
E.4	Hands on Inter-Electrode Impedance Measurements	xvi
F	Author's Publication List	xxi

Chapter 1

Physiology of Visual Perception

”To See a World in a Grain of Sand
and Heaven in a Wild Flower,
Hold Infinity in the Palm of your Hand
and Eternity in an Hour.”

William Blake, *Auguries of Innocence*

The human brain is comprised of 10^{11} nerve cells, interlinked by 10^{15} connections [1], making it ”the most complex and orderly arrangement of matter in the universe” [2]. Our brain is the core unit in our interactions with the world: it reads the five senses and sends responses accordingly, and enables logical thought, imagination, dreaming and artistic inspiration [3].

Insights into how the brain works have been gained by recording its electrical or magnetic activity with Electroencephalography (EEG), Electrocorticography (ECoG), intracortical or Magnetoencephalography (MEG) methods¹ [3]. While most of our knowledge was gained within the past 30 years, major research focus was set on Brain-Computer Interfaces (BCIs). They record activity patterns of ongoing processes in the brain (motor or cognitive processes). The recorded patterns are converted into control signals for external electrical devices e.g. control of a mouse cursor [4]. In some cases BCIs may be used to intervene in the brain’s subtle data processing. Purpose of these interventions is to bypass natural biological pathways in order to enable, for example, the blind to see [5].

This Work is part of a research initiative on an ECoG-based BCI for recording electrophysiological signals from the primary visual cortex [6]. This Chapter introduces the visual pathway from the eye to the primary visual cortex.

To perceive an image seems to be a straightforward process, and yet it is highly sophisticated one, with many behind-the-scenes stages [7]. The ease we perceive the world around us is what

¹EEG has been applied since 1924, intracortical recording since 1950, and MEG since 1968.

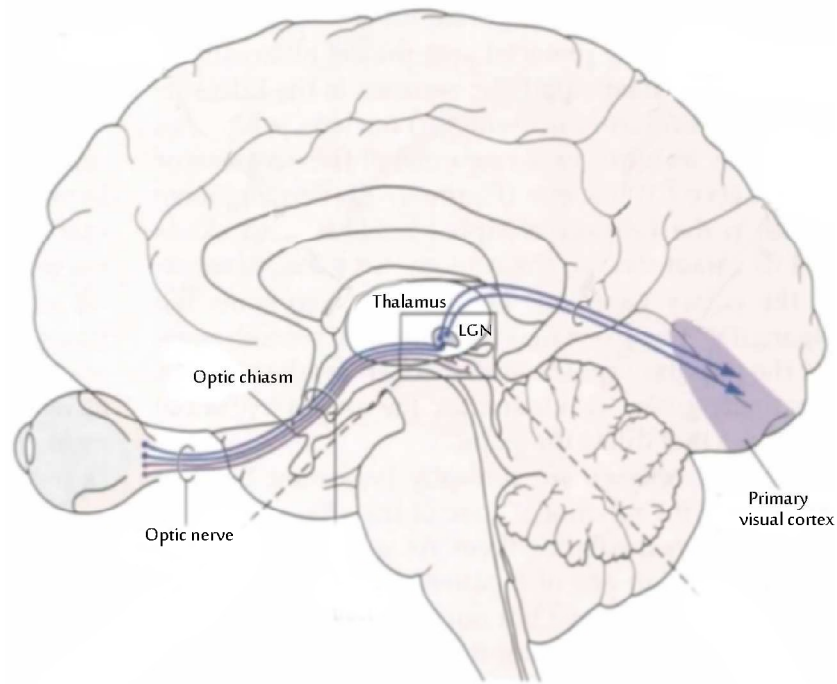


Figure 1.1: Visual pathway from the eye to the primary visual cortex [9].

misled scientists in 1960s to consider engineering "artificial vision" as a simple summer project [8]. Today this project has still to be solved.

Fig.1.1 shows the visual pathway from the eye to the visual cortex. This pathway begins with the retina, where light is translated into electrochemical impulses (action potentials), and initial image processing takes place. Pre-processed information of the image leaves the retina in form of electrochemical impulses which travel along optical axons. These become bundled in the optic nerve and terminate at the thalamus. Axons leave the thalamus to terminate at the primary visual cortex. The thalamus receives all sensory signals and acts as a gateway between the senses² and the cortex³. The primary visual cortex is the place where cortical processing of an image begins. The visual process takes up 1/3 of the total cortex processing.

Vision begins when light reflected by an object (a coffee cup) enters the eye (see Fig.1.2.A). The opening of the iris (pupil) adjusts the amount of light and the eye lens inverts and focuses⁴ the image on the retina [7]. The retina not only senses light by its photoreceptors, but also performs initial image processing by its neural network (see Fig.1.2B). Photoreceptors respond to light by sending graded potentials, whereas their membrane potential will be gradually

²Hence, the thalamus controls which sensory input to pass or to suppress.

³Cerebral cortex is the outermost sheet of the human brain, ca. 2-4mm thick.

⁴The eye lens is made of jelly-like material, which enables it to change shape quickly from spherical to flat, and hence change focus from near objects to far objects [7].

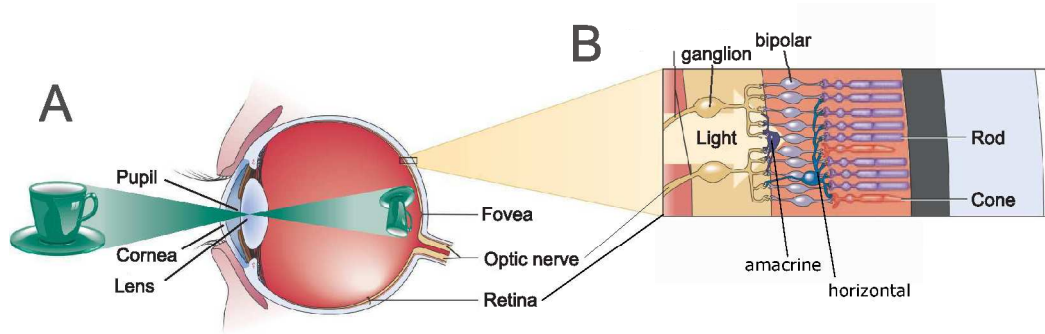


Figure 1.2: (A) An image is inversely mapped on the retina; (B) The retina is build up from photoreceptors and a neural network of a direct pathway (bipolar cells) and indirect pathway (horizontal and amacrine cells); images adapted from [7].

changed in accordance with the light intensity. Photoreceptors come in two types, called cones and rods. The cones sense red, green and blue light, one cone type per each of the light wavelength ranges. The rods sense dim light. There are 6 Mio cones and 120 Mio rods, in total. The retina contains an area of highest spatial resolution called fovea. It contains only cones. It is the place where the focus of the coffee-cup image falls (see Fig.1.2) [7].

Once the cones/rods transform a light pattern into electrochemical impulses, these are then processed by a retinal neural network (see Fig.1.2.B). It consists of a direct pathway (bipolar cells) and inhibitory pathway (horizontal and amacrine cells). Ganglion cells receive electrochemical impulses directly from the bipolar cells and also from the inhibitory cells. The axons of ganglion cells merge together and leave the eye via the "blind spot" towards the thalamus (see Fig.1.1). This retinal network performs preliminary processing of the coffee cup. In reality we perceive only the outlines of the coffee cup, but not its interior. The retina can be divided into two regions, fovea and periphery, in accordance with the distribution of the rods and cones. The fovea contains only cones i.e. it is the spot of best colour vision. Each cone sends its electrochemical impulses via a bipolar cell to its "dedicated" ganglion cell (1:1 mapping). This enables us to perceive the fine details of an image e.g. the letters of this text. The periphery contains both cones and rodes, whereas the rods prevail over the cones. Each ganglion cell receives signals from ca. 120 rods and 6 cones (convergence). Hence, our image perception is "blurred" and most sensitive to shades of gray (dim light).

In total, 2 Mio ganglion axons leave both eyes, become grouped into nasal and temporal bundles, and cross at a structure called *optic chiasm* (see Fig.1.3). Temporal and nasal bundles from each eye continue to each of the brain hemispheres. Temporal right-eye and nasal left-eye bundles go to the right hemisphere, where they terminate within the thalamus. In there, 10%

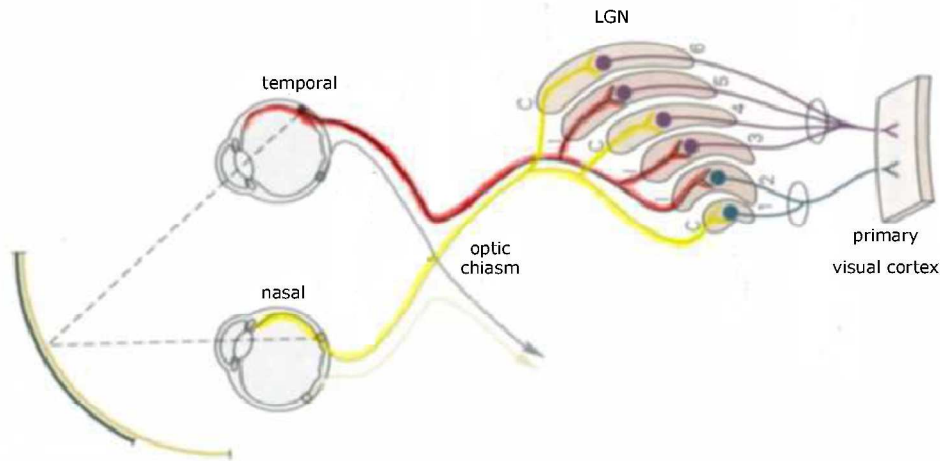


Figure 1.3: Mapping of ganglion axons from the retina to the LGN [9].

of the axons project to the *superior colliculus*, responsible for eye movements, and the rest land in the LGN. The brain has adopted this crossing-projection not only for visual stimuli, but also for pain, touch and partially for hearing. The reason for this cross projection has not yet been understood [10].

The LGN itself is comprised of 6 cell layers arranged in parallel-plate fashion. The right-hemisphere LGN layers 2,3,5 receive signals from the right eye, and layers 1,4,6 receive signals from the left eye (see Fig.1.3). The LGN cells respond in a similar way to stimuli as the retinal ganglion cells. Each LGN cell receive simultaneously inputs from the retina, the primary visual cortex, the brain stem and other LGN neurons [7], [10].

Receptive fields of neurons along the visual pathway Light patterns can trigger unique cascades of electrochemical impulses along the visual pathway: similar impulses in retinal and LGN neurons, and different ones in neurons of the primary visual cortex (V1). Each neuron along the visual pathway will respond to a light pattern situated in a confined region of the visual space, the region being called receptive field (RF). For example, if a spot of light is situated in the center of the visual field, this will activate only neurons in the fovea [7].

In the retina and LGN, the cells have receptive fields of center-surrounded configuration and come in two types: on-center and off-center.

On-center cells increase their firing rate, when the light intensity in the RF-center increases (see ii in Fig.1.4). If light falls only into the surround region, firing rate decreases below the spontaneous rate (see iii). This mechanism serves as basis for the detection of contrast edges.

Off-center cells will react to spots of light exactly oppositely to on-center cells i.e. only when

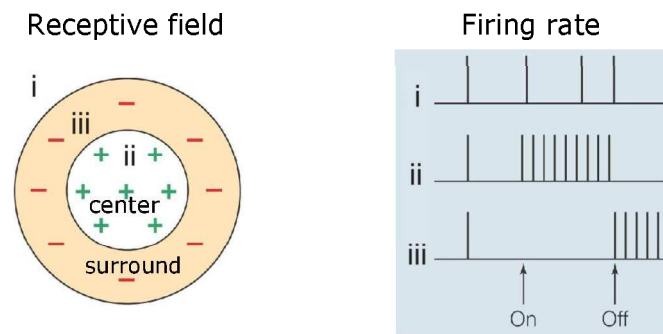


Figure 1.4: Response of an on-center neuron to light stimulation: i). if the light spot is larger than the RF, no change in neuron's activity will be observed, ii). if the light spot is confined within the RF-center, the neuron will respond with high firing rate, iii). if the light spot confines also the surround region, then the neuron will not respond at all as long as the light spot shines, however will send a burst of impulses the moment the light is switched off; images adapted from [7].

the surround region is illuminated by light, then the neuron will increase its firing rate.

In the primary visual cortex (V1) neurons will not react readily to light spots, but to bars of light which move at micro pace across the receptive field or light patterns which move into the receptive field e.g. a project slide while being inserted in a projector. Nevertheless, the preferred stimulus of retinal and LGN neurons is a spot of light.

Two types of neurons prevail:

Simple cells respond to specifically oriented bars, which appear or move across the visual field at micro-pace. For example, one type of simple cortical cells will respond best to a vertical bar by a high firing rate (25 impulses per second) and once the bar is slightly tilted off, the firing rate will drastically decrease (see Fig.1.5B,C). Other types of simple cells respond selectively to other bar orientations [10]. Specific feature of all simple cells is, that their response depends on where in the RF the light stimulus appears, similarly to retinal and LGN cells (see Fig.1.4).

Complex cells are also orientation selective, similarly to simple cells⁵ (see Fig.1.6B) [7].

In summary, perception is based on environmental stimuli being translated into electrical impulses, or per Goldstein *"I can tell that there is a coffee cup sitting on the table... I know that this feeling ... is largely an illusion...created through the actions of photoreceptors that change environmental stimulation into electrical signals and by the actions of convergence, excitation,*

⁵Originally, Hubel and Wiesel used small light spots as test stimuli. However, they found out that most of the neurons in the visual cortex simply did not respond to these stimuli. The breakthrough came when upon inserting a glass slide into their light projector (see Fig.1.5A), a cortical neuron "went off like a machine gun" [7], Goldstein cited this description from Hubel et. al. 1982.

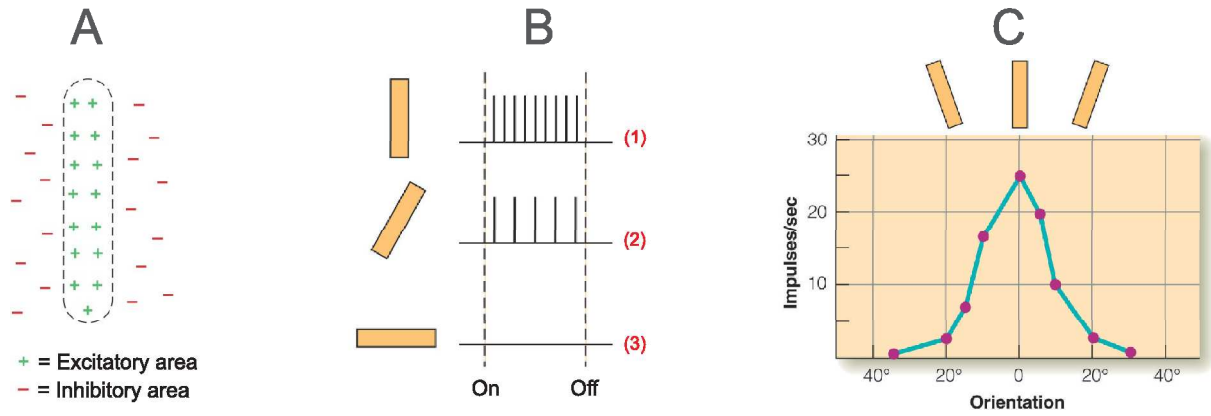


Figure 1.5: (A) Receptive field configuration of neurons in the visual cortex; (B)&(C) Response of a simple cortical cell to a vertical bar; images were adopted from [7].

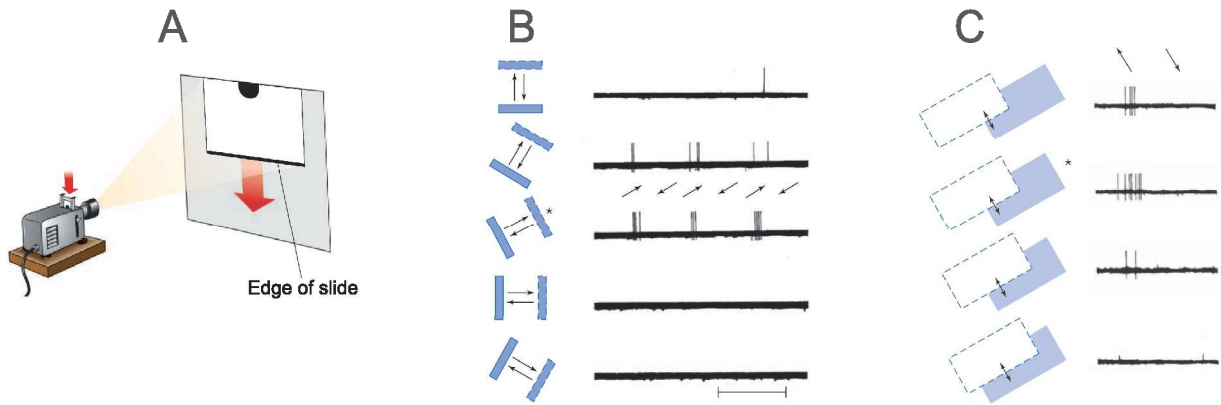


Figure 1.6: (A) Hubel's test set-up to stimulate complex cortical cells; (B) Response of a complex cortical cell to a specifically oriented moving bar; (C) Response of an end-stopped cell to oriented moving bars of a specific length; images adopted from [7], Goldstein adopted B and C from *Hubel et al. 1965*.

and inhibition“ [7].

Chapter 2

Vision of a Cortical Interface

”The highest activities of consciousness
have their origins in physical
occurrences of the brain,
just as the loveliest melodies are not too
sublime to be expressed by notes.”

Somerset Maugham

When a ray of light falls onto the retina, it stirs a cascade of electrochemical impulses within the brain. This highly coordinated cascade occurs within and across neuronal networks that synchronize the firing rates of their electrical impulses, similar to an orchestra [11]. The brain rhythms, these networks produce, can be recorded by means of several methods: EEG, ECoG and intracortical electrodes. This Chapter focus is set on ECoG recordings as newly emerging discipline as it can serve as very promising signal-acquisition platform for novel, weakly-invasive, attention-driven BCIs.

2.1 Vision of Attention-Driven BCI

In 1964 Dr. Grey Walter implemented one of the first brain-computer interfaces (BCIs): a person could activate a slide projector only by thinking about it (without performing any finger movements). Today we know that just a person’s intent can trigger sophisticated brain rhythms which in turn can be used as communication or control signals in external electronic devices and thus directly translate a person’s intent to a piece of hardware [12].

When used for communication means, such a brain-computer interface could profoundly improve the lives of fully paralyzed (locked-in) persons¹. Hochberg et al. [14] implanted pen-

¹People that cannot move their muscles, “but retain all sensation, consciousness and cognition” [13].

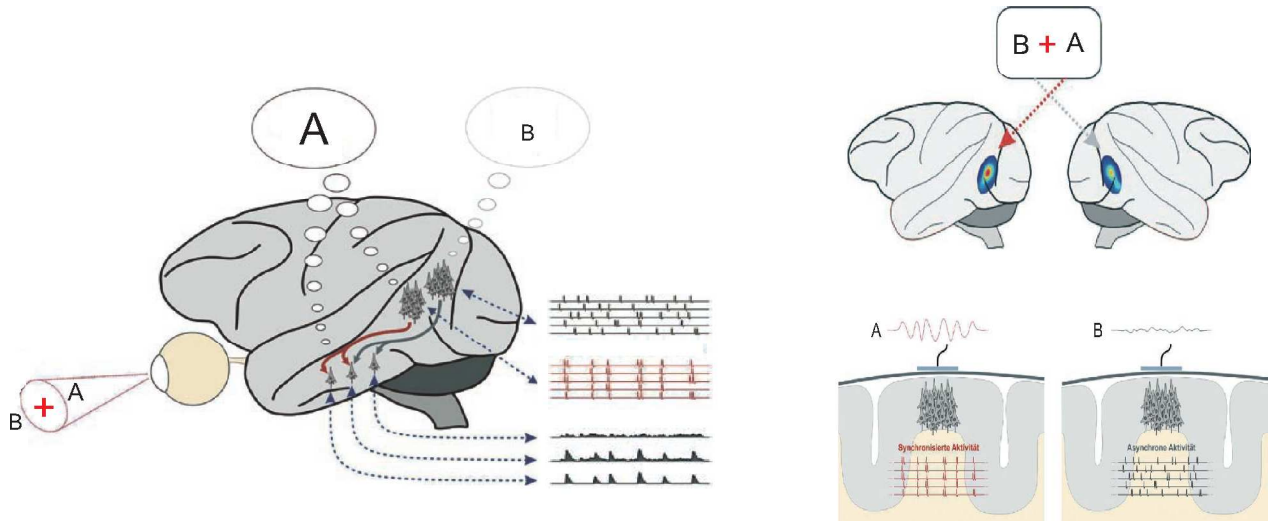


Figure 2.1: (Left) An attended object will induce synchronization of the firing of action potentials, in contrast to the rest of the visual field; (Top right) A gaze fixed at the center-cross, but attention focus on the right structure, will induce a high synchronized electrical activity in the left hemisphere; (Bottom right) This synchronized electrical activity can be measured for example with electrodes placed on the cortex (ECoG); images adopted from [15].

etrating electrodes into the motor cortex of paralyzed people. The brain rhythms acquired by the electrodes were used by a brain-computer interface to allow the control over a robotic arm. However, penetrating electrodes (intracortical) are highly invasive recording means. Recordings from the head skin (EEG), on the other hand, are non-invasive. However, on the way to an EEG electrode brain rhythms become highly attenuated, for example by the skull² and details about specific states of motion or cognition become lost.

As an alternative, ECoG devices are implanted on/below the dura matter, do not penetrate the gray matter, and are therefore less invasive than intracortical electrodes. ECoG electrodes are situated beneath the skull, and hence provide higher signal resolution than EEG recordings. Recently, the research group of Prof. Kreiter [15] showed first proves that ECoG recordings could enable a BCI based on selective visual attention to help fully-paralyzed people communicate with their surroundings by means of a virtual keyboard. Fig.2.1 illustrates how selective visual attention could enable a virtual keyboard BCI [4]. When person's gaze is fixed at a central point marked with +, attention can be can be shifted voluntarily sideways (covert at-

²Brain rhythms arrive also at the EEG electrode in a highly averaged state, because the field potentials of millions of nerve cells, situated in the vicinity of the EEG electrode, superimpose themselves in a destructive manner. Hence, only strong oscillatory field signals, which superimpose themselves constructively (in phase), have the chance to be sensed by the EEG electrode.

tention³). With gaze fixed at + and attention shifted sideways, for example in the direction of letter A, will trigger neuronal populations fire action potentials in coherent manner within the gamma frequency range (40-160 Hz). If a recording electrode is positioned in a location corresponding to the letter A, this electrode will record an increase in neuronal activity in comparison to the same object when letter B is attended [15].

2.2 Recording of Brain Rhythms

A virtual-keyboard BCI can mature toward real-world applications provided brain rhythms are recorded with high spatial and temporal resolution. Currently, there are three basic methods to record brain rhythms with electrical means – EEG, ECoG and intracortical electrodes – ordered according to their distance from the source of a brain rhythm (EEG is most distant).

- **EEG** is the most common recoding means in humans as it is a non-invasive recoding technique. The electrodes are positioned on the scalp and can acquire electrical potential traces with amplitudes in the 100 μ V range (see Fig.2.2.A). The EEG signals span the 1-50 Hz frequency range and reveal basic levels of consciousness – whether a person is awake, in light or deep sleep, or not alive – and record bursts of electrical activity associated with epilepsy [17]. However, EEG recoding are able to capture only global cortical phenomena – as brain rhythms, generated in the uppermost neuronal layers, need to travel through the skull they become low-pass filtered which limits the spatial and temporal resolution of EEG traces. This hinders the localization of centers of epileptic seizures with high precision, not mentioning natural cognitive activity of much lower amplitudes [11] such as selective visual attention i.e. the EEG-based BCI performance is not always reliable [18].
- **intracortical** recording technique is the most common invasive method in animals. The electrodes are inserted into the cortical tissue and can sense the extracellular electrical activity of a few neurons i.e. of exceptionally high signal resolution. When an electrode is positioned next to a neuron, it records all trans-membrane potentials in the vicinity of the electrode tip. These electrical potentials reflect (1) ion currents originating from action potentials, frequency range 300 Hz -5 kHz [19], [20], and (2) 1-150 Hz local-field potentials i.e. post-synaptic currents at the dendrites of the neuron and the associated *return currents* [21], as illustrated in Fig.2.3. Oscillatory activity in the gamma band (>35 Hz) has attracted much interest as it is related to perceptual and cognitive processing in the visual

³If you are looking and listening to your companion in a restaurant, your visual attention can shift sideways to the people on the next table even without moving your eyes [16].

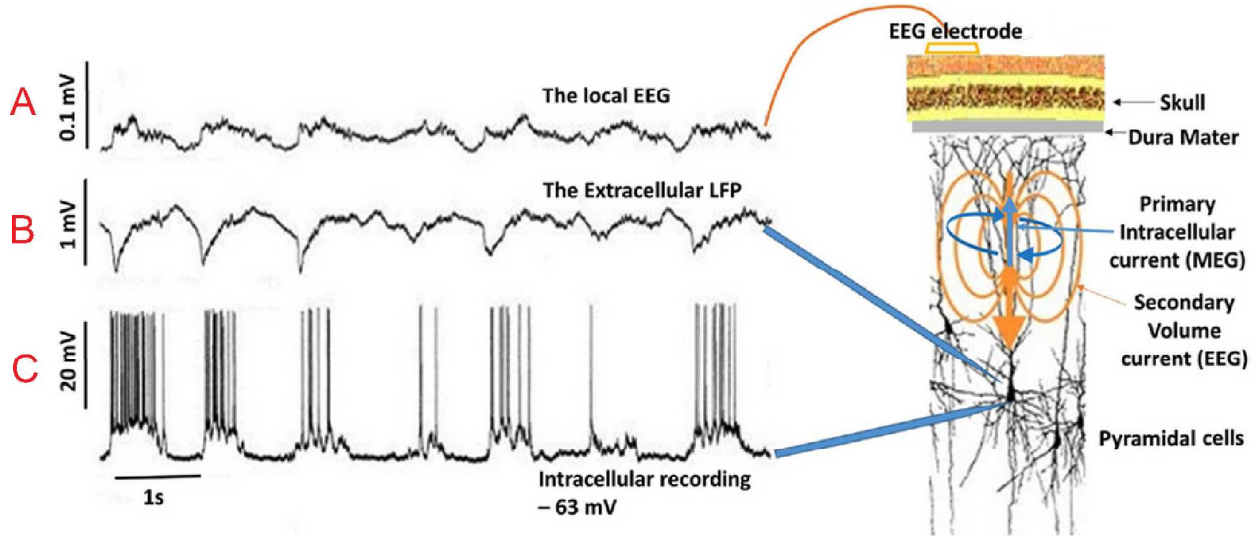


Figure 2.2: Electrical activity recorded from a cat pyramidal neuron during deep sleep: (A) an EEG signal; (B) LFP activity; (C) Action potentials (spikes); adopted from [19].

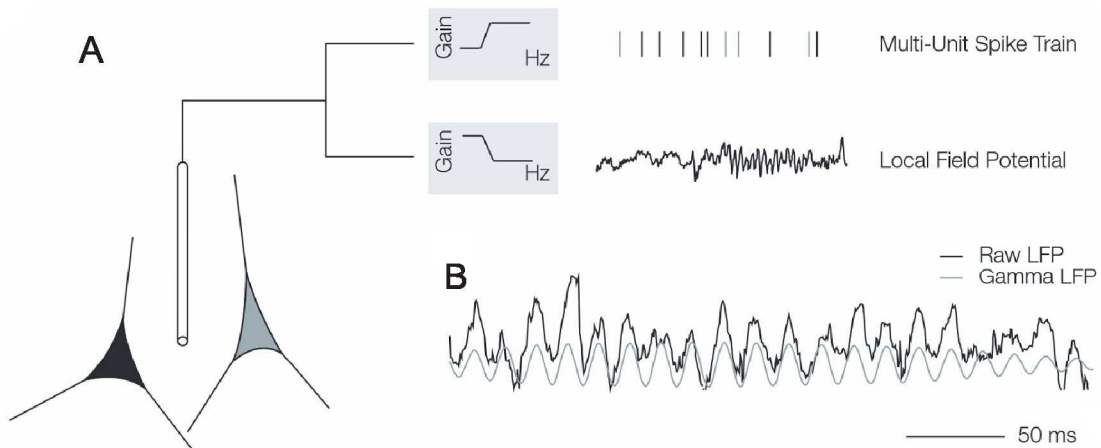


Figure 2.3: (A) An intracortical electrode senses spikes and local field potentials, the latter contains gamma-band oscillations evoked by light stimulation (B); adopted from [20].

cortex. In short, intracortical electrodes can record brain rhythms of exceptionally high spatial and temporal resolution and therefore can potentially enable multi-dimensional BCIs. However, the electrodes irreversibly damage neurons upon implantation, which in turn diminishes the signal quality up to complete signal loss [18].

- **ECoG** waveforms, recorded directly from the cortical surface, offer an intermediate signal resolution. As the skull is eliminated as signal attenuator/low-pass filter, ECoG recordings excel EEG ones in signal quality: (1) ten times higher in amplitude (50-100 μV than the

max. 10-20 μV of EEG signals [18], [22]) and (2) cover much broader frequency range (0-500 Hz vs. 0-40 Hz of EEG [18], [22]). When compared to intracortical recordings, ECoG electrodes do not damage any neuronal tissue upon implantation⁴ and thus offer robust signal-acquisition for long periods of time [18], [22]. And yet, the most essential feature of ECoG waveforms is that they contain the gamma frequency band. Selective visual attention is a cognitive process which “extracts” only the most relevant features from an image – e.g. a friend’s face from a crowd – by modulating the gamma band activity and thus enhancing the neuronal processing [23]. Based on this, ECoG electrode arrays can enable novel BCIs based on selective visual attention [4].

2.3 Origin of ECoG Potentials

Recording electrophysiological activity from the cortical surface is an optimal signal-acquisition method for future BCIs in terms of invasiveness and signal quality. Situated far away from a single neuron ECoG electrodes cannot resolve a single spike but rather the electrical activity of whole neuronal populations. But what aspect of the neuronal activity does the ECoG waveform reveal?

Fig.2.4.A illustrates two epidurally implanted ECoG electrodes – a recording electrode (“recorder”) facing the cortex, and a reference electrode facing the skull. Provided a change in the electrical activity of a neuronal population is evoked – e.g. by stimulating the retina with a bar of light – then a potential difference will be measured between the recorder and the reference⁵. For example a bar of light evokes electrical activity within the retina, which in turn maps it to specific columns of the visual cortex. An ECoG electrode will sense the cortical activity associated with this bar of light only if the electrode is situated in the vicinity of these specific cortical columns⁶. Such a column occupies ca. $300 \times 300 \mu\text{m}^2$ portion on the cortical surface, span all six layers of the cortex and contains ca. 10 000 neurons – 80% excitatory and the rest inhibitory. The excitatory neurons have either spherical or pyramidal shapes, whereas inhibitory neurons come in many different shapes. Pyramidal excitatory neurons have long apical dendrites which span several cortical layers⁷, “considered to play an important role in

⁴ECoG electrodes rest either on the dura matter (epidural) or under the dura (subdural).

⁵The potential acquired by an ECoG recorder swings from positive values to negative values with respect to a (skull-facing)reference.

⁶The area of the activated cortical region depends on the size of the light stimulator. For example, each neuron in V1 processes a portion of the visual field, the portion’s diameter equal to $0.5 - 1^\circ$ visual angle i.e. a receptive field. Neighbouring neurons acquire inputs from neighbouring receptive fields. The neurons will be activated, which receive inputs from light-stimulated receptive fields.

⁷Pyramidal cells are triangular-shaped neurons found in layers 3 and 5 of the cortex [24].

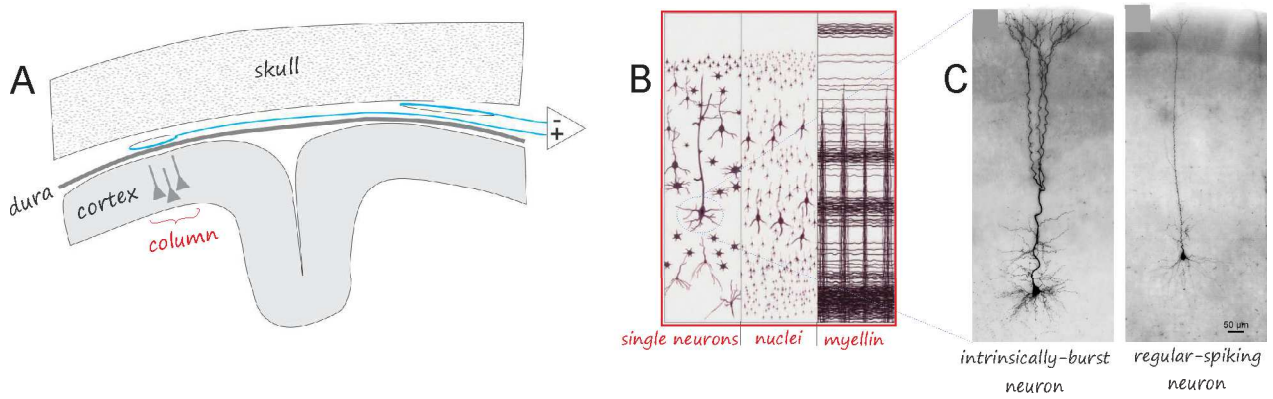


Figure 2.4: (A) Electrode configuration to acquire ECoG electrophysiological activity; (B) Layers of the cortex, image adopted from [24], (C) Pyramidal neurons from layer 5 of the cortex – an intrinsically burst spiking and a regularly spiking one, adopted from [25].

intracolumnar and transcolumnar signal processing” [25] for reasons explained below. Such a pyramidal neuron is shown in image C – a bursting neuron⁸ and a regularly spiking one [25] (consider the much thicker dendrite structure of the bursting neuron).

Pyramidal neurons essentially contribute to the waveform of EEG [26] and herewith to ECoG potentials, because (1) electrical charge of opposite polarity is separated from each other over the surface of these neurons, giving rise to a dipole, and (1) pyramidal neurons are oriented perpendicularly to the cortical surface which results in the parallel alignment of many dipoles [26]. Fig.2.5 illustrates how such a dipole is formed. The activity of a pyramidal neuron is modulated by many other neurons – either excitatory or inhibitory. As excitatory inputs outnumber inhibitory inputs by eight times, and most of all inputs are situated at the top portion of the neuron – far away from its cell body (soma) – predominantly positive charge (Na^+ ions) will be injected at the top portion of the pyramidal neuron (see Fig.2.5). As the extracellular space is electroneutral, this flow of positive ions will leave a negative charge behind, called an excitatory post-synaptic potential (PSP). As neurons cannot accumulate charge, this overdosis of positive ions at the top of the neuron (inside its intracellular space) should be compensated by an outflow of positive ions taking place at its soma. This outflow – coined as “return currents” – gives rise to positive potentials in the extracellular space near the soma. Integrating all negative and positive extracellular potentials (post-synaptic potentials and potentials due to return currents), will give rise to a relatively large dipole (see Fig.2.5).

But what does the ECoG signal waveform mirror – (1) post-synaptic potentials and their return currents, or some other accumulation of charge? In theory, every potential generated

⁸Bursting neurons can fire repetitive spike sets; between each set there is a period of “silence”, Wikipedia.

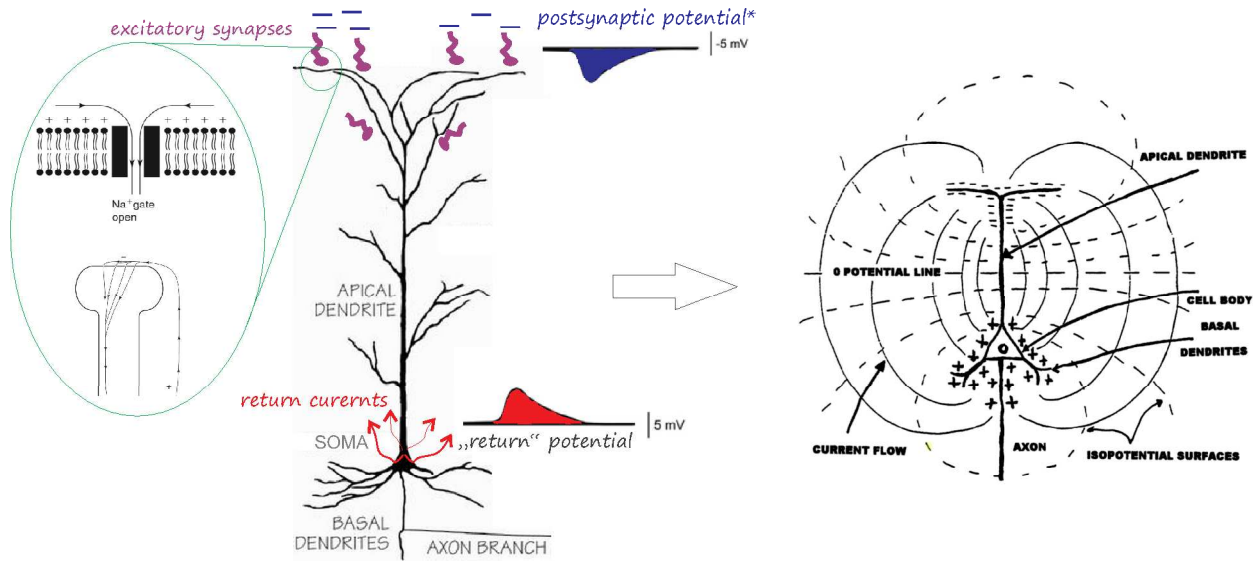


Figure 2.5: Spatial separation of excitatory post-synaptic potentials (blue) and potentials due to rerun currents (red) at the top and bottom portion of a pyramidal neuron, respectively. The sum of these opposite potentials gives rise to a dipole, images adopted from [27], [28], [26].

within the extracellular space which can reach the recoding ECoG electrode will contribute to it. The larger the distance from the potential source, the less informative is the recorded signal, because the potential amplitude scales with the inverse of the distance and/or interfering signals may stand in the way of the signal (spatial averaging) [29].

Considering the three basic sources of extracellular potentials, the following conclusions of how they modulate the ECoG waveform can be deduced:

- **Post-synaptic potentials** The amplitude of a postsynaptic potential (generated by a single synapse) is 1-2 mV and as the potential dissipates by diffusion currents, its amplitude decreases in time/space. Hence, a single post-synaptic potential is several times smaller in amplitude when compared to the 100 mV of a Na⁺ spike (action potentials). Nevertheless, even if postsynaptic potentials are of short duration, they “dissipate” by slower (diffusion-driven) ion currents than the Na⁺ spikes (1 ms range), and last for much longer time. Hence, the probability of postsynaptic potentials to superimpose at a given spot far way from the neuronal source is much higher than that of spikes [11], [30]. Further, the number of generated postsynaptic potentials exceeds the number of generated spikes, as within a given volume of neurons only a small group can reach the spike threshold at a given moment [11]. Further, once generated, both postsynaptic signals and spikes need to travel via the membranes of neurons, glia matter and blood vessels⁹ to reach the recoding

⁹potentials decrease by $1/d$ with the distance d from the source/sink, whereas dipoles by $1/d^2$

electrode. The low-resistance nature of the extracellular fluid (shunting effect) and the fact that non-active neurons act as low-pass filters favours the propagation of postsynaptic potentials towards the recording electrode and hinders the spikes [11].

- **Na⁺ spikes** give rise to the strongest currents in the cortex, but because their duration of 2 ms is rather short, they are thought to contribute little to the Local Field Potentials (LFPs) and herewith to the ECoG waveform. Additionally, neurons fire seldom Na⁺ spikes synchronously. And yet, under certain circumstances neuronal populations tune the firing of their Na spikes (or spike trains) which can contribute a lot to the higher frequency part of the LFP and thus to the high-frequency ECoG waveforms and reveal the distribution of spiking populations in time [29] (see synchronous oscillations).
- **Ca²⁺ spikes** are of much longer duration (10 -100 ms) than Na⁺ spikes, have amplitude of 10-50 mV and can therefore contribute substantially to the LFP. However, little information is present for Ca²⁺ spikes in vivo [29].
- **Synchronous oscillations** Even if a cortical region has highly aligned pyramidal cells with strong dipoles as a result of post-synaptic potentials, this alone will not give rise to large ECoG signals. For large ECoG signals to be generated, network oscillations should be highly synchronized i.e. many neurons firing Na spikes in form of repetitive bursts in a synchronous manner¹⁰ [29]. Even if neighbouring neurons rarely fire synchronously, neuronal populations situated across larger distances from each other can synchronize their firing rates, when triggered by specific stimuli. Herewith, these highly synchronous spiking activities can contribute to the high-frequency component of LFP and herewith to ECoG signals. For example, some neurons respond best to specific frequency bands e.g. they resonate in the 30-90 Hz gamma range upon visual stimulation [29].

In short, ECoG waveforms reflect predominantly the dipoles of postsynaptic potentials (and the associated return currents) of highly aligned long pyramidal cells. The ECoG amplitude is strongly modulated in the gamma-frequency range by neuronal populations highly synchronizing the timing of their post-synaptic potentials [11]. Further, the ECoG amplitude is determined by the architectural structure of the cortex at the site of the recording electrode, as well as the geometry of cells (highly oriented pyramidal cells contribute most) and several other factors [29]. As ECoG waveforms reflect neuronal oscillations in the gamma band (among several

¹⁰Most regularly spiking neurons can fire a burst of spikes if stimulated with a slowly-changing sinus-shaped current “that slowly drives the neuron above and below the firing threshold”. On the other hand, there are intrinsically bursting neurons which possess slowly-changing intrinsic currents. From Wikipedia

other electrical activities), this makes them highly attractive for robust BCI systems based on selective visual attention.

2.4 ECoG Recordings for Attention-Driven BCIs

Until a few years ago it was unclear if LFPs carry information about meaningful states of brain activity. Mehring and colleagues [31] showed that LFPs from the motor cortex contain information about parameters of hand movements. Surprisingly, the LFPs and the spikes contained partly independent information which could be combined to achieve a better reconstruction of the observed hand movement. This result showed that measurements of averages over larger neuronal populations can be used for neuro-prosthetic applications. However, the long term stability of LFP recordings for medical applications is problematic. A more long-term stable way to measure the required neuronal signals, compared to LFPs, are epidural or subdural ECoG recordings.

On the one side of the observed population size is the LFP (small populations) and on the other side the EEG (very large populations). While the LFP is highly informative, the EEG is known to be much more limited in its information content [32]. For some time it was unclear how much information can be extracted from ECoG signals (which lies in between LFP and EEG in population size), especially the less invasive version: the epidural ECoG. An additional question was if there is an alternative source for BCIs than the motor cortex and if it is unsuitable due to e.g. degeneration caused by a neurological disease.

In [4, 33] both questions were addressed. It was shown that epidural ECoG recordings are good signal source for BCIs and that it is possible to use neuronal activity patterns from the V4, modulated by the selective visual attention, for a brain computer interface. Only a few 100ms of multi-channel ECoG data was enough to reliably determine the position of visual selective attention [33], which can be used to establish a fast interface between a handicapped patient and an external decoding system (a speller or controller of external devices).

The goal of current research is to build such a visual BCI that operates in real time. To accomplish it, selective visual attention needs to be shifted as fast as possible between different symbols (e.g. letters of a spell-board). The maximum amount of information (bit per time) is determined by: (1) the frequency at which attention can be shifted between letters, (2) the time required for the decoder to localize the focus of attention, (3) the spatial resolution of decoding the focus of attention. However, the quality of these decisions (e.g. % correct) also influences the extracted information per decision and time. Rotermund et al. [33] investigated both, the influence of the length of the time series and the distance between the two symbols, as follows: the animal under test had to fixate gaze on a rectangular dot which served as a

gaze fixation point on a computer screen. An ECoG array was implanted epidurally over the visual cortical regions V1 and V4. Two trial objects were presented to the animal. These objects 'morphed' their shape over the trial independently. At the beginning of the trial the animal was informed which one of those objects is behaviourally relevant¹¹. The animal had to memorize the shape of the original object and in case of re-occurrence, had to release a lever. Parameters of the timing were changed pseudo-randomly, to prevent the animal from guessing the timing without observing the computer screen¹². This experiment was conducted in two different configurations:

- **Configuration I:** two small visual stimuli, placed in close proximity on the computer screen which are processed within the same brain hemisphere (Fig.2.6.Left.B)
- **Configuration II:** two large visual stimuli, placed at positions on the computer screen which corresponds to two different brain hemispheres (Fig.2.6.Left.A)

Configuration I is highly interesting concerning high-performance BCIs. The result shows that it is possible to place two objects in very close proximity and still be able to distinguish which one of the objects is attended. This is very surprising because the regions in the brain which process these objects strongly overlap. This suggests that placing many different objects (e.g. the whole alphabet) on a computer screen seems possible, which would substantially increase the amount of information per decision.

Selected time intervals of the time series and electrode positions were spectrally analyzed with methods from machine learning (Support Vector Machine), showing that even several 100 ms of the recorded time series are enough to perform a reliable estimation on which of the two objects attention was placed.

The ECoG recordings were performed by 36 Teflon-coated Pt-Ir wires (50 μm in diameter, obtained from Science Products), as shown in Fig.2.6.Left.D & E. The Teflon-insulation was removed at one end of each electrode, and each of these pieces "was bent into a loop of 210-220 μm diameter", which resulted in impedances of 25 k Ω at 100 Hz. The wires were positioned at 3 mm interdistance on a 0.1 mm thick Silicone foil (Goodfellow) and covered by a silicone film (Dow Corning 734). The reference signal was obtained by two Pt-Ir electrodes placed frontally (150 μm diameter) and a third electrode was positioned on backside of the electrode array, serving as a skull-facing reference. The obtained ECoG signals were magnified $\times 40\,000$ within the 1-150 Hz range.

¹¹Relevant means that the animal had to observe this object closely (continuously focus attention on this object while keeping the gaze on the fixation point) and ignore the other one.

¹²Check [23] for more details, especially concerning the timing of the visual stimulation, about this experiment.

An example of the recorded ECoG signals is shown in Fig.2.6 (right side). These signals were recorded while the animal was fixating its gaze on the fixation point and directed its selective attention to one of the two objects on the computer screen (configuration I). Sub-image C shows raw ECoG signals. The upper time series was obtained when the selective attention was directed towards the visual object that was represented by the brain hemisphere which was covered by electrode grid (the electrode grid covered only part of V1 of one brain hemisphere). The lower time series was recorded with attention directed to the object represented by the other brain hemisphere. By comparing the spectral components of both time series in sub-plot C, it is possible to determine the location of attention. The upper time series stands out by its high frequency component (50-150 Hz), which implies that selective attention increases the power in high-frequency components of ECoG signals [23].

The analysis is strongly based on a spectral decomposition of the ECoG signals, before the classification with methods from machine learning. In the following it will be explained how this pre-processing was applied. Within the brain, electrical currents flow into nerve cells, as well as flow out of these cells, approximated by electrical dipoles. The local field potentials, and also ECoGs, reflect this continuously occurring shift of dipoles within local regions of the brain. Typically, these measurements are referenced against a special and distant electrode (with respect to the recording electrodes). This makes the signals vulnerable to perturbations that are conducted via the brain from distant current sources to the electrodes [34]. To get rid of these effects and "minimize spatial smearing" [35], it is possible to calculate a scalar density map over all the electrodes of the current sources via the Poisson equation. The result of this operation is called current source density (CSD).

This CSD distribution is then spectrally decomposed using a Wavelet transformation [36]. Such a Wavelet transformation can be roughly understood as a Fourier transformation of only short segments of the time series. For each short segment the corresponding complex Fourier coefficients are calculated. The selection window is moved from the beginning of the time series to its end in small time steps. In the end this creates a 2D matrix representation of the original time series. One dimension represents the time over the time series. The other dimension corresponds to the frequencies contained in the signal.

Using such a short-term windowed Fourier transformation has several problems. One problem arises from the Heisenberg uncertainty principle. A good time resolution results in a bad frequency resolution and a good frequency resolution results in a bad time resolution. Thus, an optimal balance of both is required for every frequency band that is analyzed. A second problem is that short and simple (e.g. box shaped) selection time-windows cause deformations in the resulting spectra. The smaller the window, the stronger the deformation effect. Both aspects lead to the requirement of a well-formed selection time-window which has a size that depends

on the individually analyzed frequency band. One way to solve this boundary conditions is to use a Waveform transformation instead of a windowed Fourier transformation.

In [4] the so called Morlet mother-wavelets were used to create a suitable filter for every frequency band. These Morelet wavelets provide a good compromise between time and frequency resolution for analysis of neuronal signals. Based on the complex wavelet coefficients a time-frequency power spectrum is calculated [37]. Subplot A in Fig.2.6.Right shows an example for such a time-frequency spectral power distribution for ECoG signals recorded under different conditions of selective visual attention.

In this plot, the spectral power was normalized by the baseline activity which was acquired in the time interval before the onset of the visual stimulation presenting the shape objects. This allows to highlight the part of the neuronal activity which was induced by the task [38]. The shown time-frequency spectral power density "was averaged over several hundred trials" [4] to reduce noise [37]. The figure shows that the first two trial phases contain (in all frequency bands) a lower spectral power compared to the putative behaviourally relevant trial phases.

In trial phase one, the animal has to memorize the shape of the object which is marked in green. Beginning with phase two, the object's shape transforms (morphs) continuously into another shapes. After phase two, the animal has to observe the actual shape of the object and compare it to the memorized shape. In the case of a reoccurrence of that shape, the monkey has to release a lever for getting reward. In the following trial phases an evident increase in spectral power in the gamma range (30-100 Hz) was found.

Subplot B (right), in the same figure, presents the difference in normalized spectral power between the condition with attention and without attention focused on the object, which is observed by the epidural ECoG electrode array. Subplot B reveals a strong influence of selective visual attention on the neuronal activity measured via epidural ECoG array.

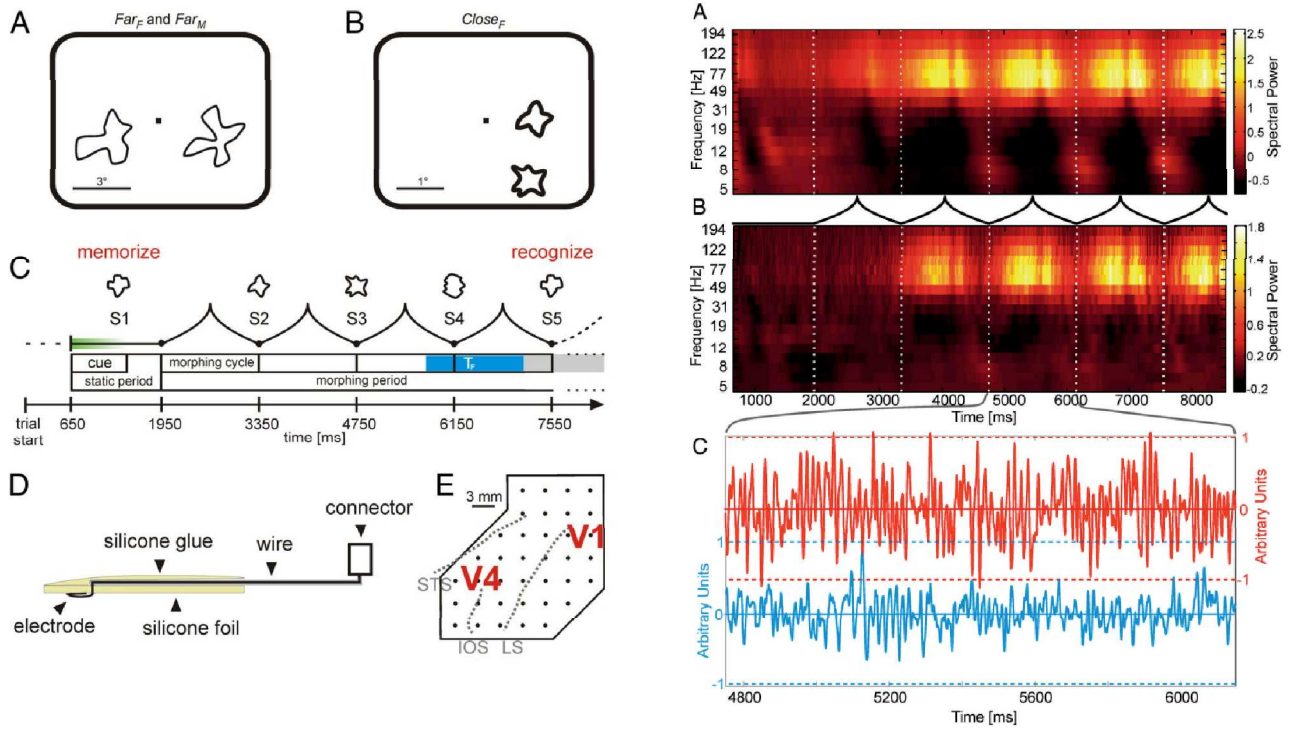


Figure 2.6: (Left A,B) Two different stimuli configurations were used. (Left A) In configuration "Far", two star-like objects were shown on a computer screen. The shapes were placed far apart such that each object was processed by primary visual cortex of different brain hemispheres. Only for one of these objects the corresponding neuronal activities were recorded by an epidural ECoG array. (Left B) In the other configuration "Close", both objects were placed near each other. Here the neuronal activities evoked by both objects were recorded. Furthermore, a fixation point was shown on the computer screen and eye-tracker measured the direction of the monkey's gaze during the trial. When the animal stopped fixating on the fixation point, the trial was stopped. (Left C) Temporal development of the stimuli. For a short duration, one of the two irregularly star-shaped object was marked in green and its position/shape had to be memorized. The other object served as distractor and had to be ignored. After 1950ms, both objects changed continuously and independently until the memorized shape reappeared and the monkey had to release a lever. For a correct response the animal was rewarded [23]. (Left D) Schematic of the implanted epidural ECoG MEA. (Left E) Positions of the individual electrodes in reference to the covered brain regions of the visual cortex. (Right A) Average spectral power of one electrode for the attended object during the complete trial cycle in the "far configuration". (Right B) Difference between the neuronal activity of one electrode in the attended condition (attended object is covered by the electrode array) and non-attended condition (attended object is represented by the other brain hemisphere and is not covered by the electrode grid). (Right C) Examples of a time series which was used in the analysis. The red curve represents the attended condition and the cyan curve the non-attended condition. Images adopted from [4].

Chapter 3

Microfabrication of ECoG MEAs

”Biology is soft, elastic, and curved;
silicon wafers are not.”

John A. Rogers

Recordings of brain rhythms from the cortical surface reveal highly synchronized neuronal activities which can serve as triggers for attention-based, weakly-invasive BCIs for locked-in persons. Rotermund et al. [4] has shown that ECoG electrodes can record cognitive states of selective visual attention with until recently unexpected spatial resolution. Stimuli situated within the overlapping area of two neighbouring receptive fields could be resolved from each other. This finding paves the road toward attention-driven BCIs which, due to their multiple degrees of freedom, could translate the intent of a locked-in person to an external computer, thus enabling real-time communication. To turn this vision into reality requires engineering a signal-acquisition device which can record ECoG potentials with high spatial resolution i.e. incorporating multiple recoding channels on a minimal area. The multi-channel ECoG recorder should be highly flexible in order to adopt the curvilinear shape of the cortical surface and at the same time thin enough to slip in between the 1 mm-thick gap between cortex and skull.

Microsystems technology is a good choice for multi-channel fabrication. And yet, this technology is based on inorganic materials, such as silicon (Si), formed into planar, rigid wafers. Silicon was originally chosen because it has tunable electric properties which enabled the monolithic integration of countless number of transistors on a single wafer. Its superior mechanical properties borne electromechanical micro-devices such as gyroscopes, resonators and mechanical switches [39]. Fortunately enough, at a later stage, organic materials such as polyimide have been introduced because the spin-casting of polyimide easily smoothed the severe topographies of integrated circuits (ICs) created by CVD-oxide deposition [40]. It was exactly such a polyimide layer that accidentally detached from its carrier wafer, peeling off the underlying

microelectronic circuits. Electrical tests revealed still intact electronic circuits. Situated on the polyimide film, these electronics were highly flexible and bendable and paved the way to the CIRCONFLEX technology [41]. Tomorrow's applications range from Chip-in-Paper devices [42] to flexible sensors wrapped around medical guiding wires¹ [43], to biomedical implants such as ocular or cortical implants [44], [45], [46].

This Chapter begins with a review on current ECoG recoding electrodes of highly flexible nature with a focus set on microfabrication schemes, methods to assemble connectors and optimal electrode dimensions to record electrophysiological potentials. Mechanics of flexible materials and electrospectroscopy of metal-electrolyte interfaces are addressed. In the end, an overview of what is to be encountered throughout this Thesis is presented.

3.1 State of the Art

Current ECoG electrode arrays are passive devices² incorporating metal electrodes, which serve as recoding channels and are embedded in polymeric insulating materials. Electrical connectors, mounted onto the flexible pads of the ECoG devices, provide link to external signal amplifiers, as illustrated in Fig.3.1.Left. There are two major groups of ECoG recording means: (1) macro-ECoG devices used mainly for clinical use, and (2) micro-ECoG recorders of much higher spatial resolution, applied primarily in animal studies.

Macro-ECoG devices employ Pt-plates as electrodes and Pt-wires as their electrical connections to external electronics. This Pt-metallization is embedded in a relatively thick insulation silicone material³ (a soft and biocompatible polymer). The size and distance of the electrodes is mainly dictated by the specific application of these macro-ECoG recorders. With 1 - 2.3 mm exposed electrode diameter and 10 mm inter-electrode distance, these devices are used pre-operatively to localize centers of epileptic seizures or tumors bordering motor/speech cortical regions [18], [48]. The electrodes are arranged in 8×8 grids or 4 - 6 strips, usually implanted for time periods ranging from several days to 1-2 weeks [18]. In order to slightly increase spatial resolution, silicone-based ECoG devices of higher electrode density have been implanted together with the macro-ECoGs for research purposes (70-1500 μm electrode diameters and 1-4 mm inter-electrode distance) [49], [50]. The macro-ECoG recorders fulfill their clinical purpose, but their fabrication technology has more or less reached the maximum of spatial resolution.

¹for minimally invasive medical imaging

²containing no active components such as transistors; An exception is the work presented in [47], an ECoG device which contains embedded transistors.

³400-600 μm -thick Silastic[®] base

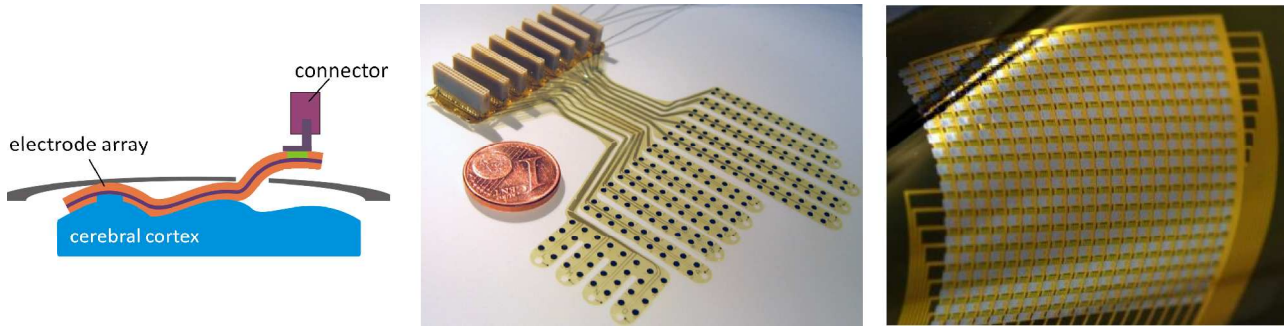


Figure 3.1: (Left) An ECoG electrode array implanted on the cortical surface with electrical connectors kept outside. (Middle) A large-area polyimide-based ECoG MEA. (Right) An active polyimide-based ECoG device containing flexible transistors, images adopted from [51] and [47].

Micro-ECoG electrode arrays have been recently engineered making use of the highly miniaturizing property of Microsystems technology. They have more complex fabrication process, which provides smaller structures and hence higher spatial resolution, and higher degree of mechanical flexibility to better adopt to the curvilinear surface of the brain. State-of-the-Art multi-channel microelectrode arrays (MEAs) have been presented by Rubehn et al. [51], Viveti et al. [47] and Ledochowitch et al. [52] (see Fig.3.1). These highly flexible devices are of high electrode number (> 64), only several microns thick ($> 10\mu\text{m}$) and of relatively large area, all these properties enabled by compliant and mechanically strong polymers such as polyimide or parylene C. Noble metals such as platinum [51], [52] or gold [53], [54], [55] serve as thin-film metallization. Additionally, PEDOT, a conductive polymer, deposited galvanically from an aqueous solution on top of the noble metal accounts for much lower electrode/electrolyte impedance [56]. Typical electrode sizes in these large-area ECoG MEAs are 1 mm diameter [51] or $300 \times 300 \mu\text{m}$ [47]. Even if the effect of electrode size on the coherence of ECoG signals has already been studied, this was performed with electrodes larger than 1 mm and at inter-electrode distances greater than 1 mm [57], [58] i.e. the optimal electrode size/interdistance, e.g. for an attention-driven BCI, is still to be determined.

Connector Assembly on micro-ECoG MEAs The micro-ECoG electrode arrays are fabricated as a polymer-metal-polymer stack on a rigid wafer and eventually peeled off the wafer to become a highly compliant electrical device. This is a straightforward way to process such a MEA which fully adopts the curvilinear shape of the cortical surface. And yet, the challenge to assemble bulk SMD connectors on such flexible device calls for smarter solutions.

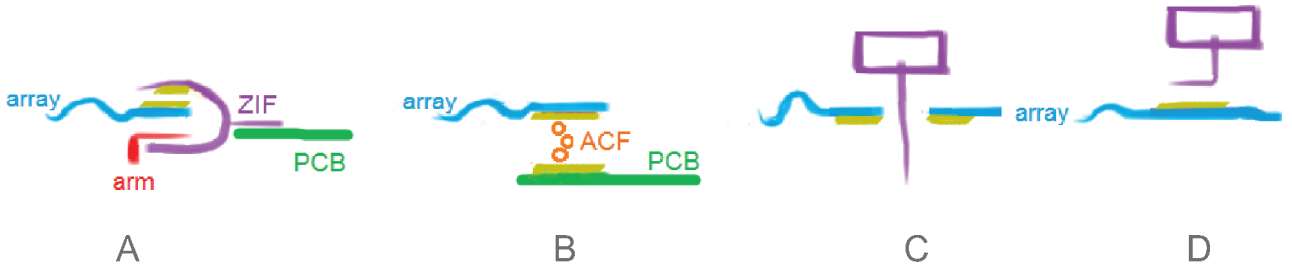


Figure 3.2: Overview of electrical connection methods for micro-ECoG MEAs: (A) ZIF; (B) ACF; (C) Through-hole Omnetics; (D) SMD Omnetics.

zero-insertion-force connectors (ZIF) were used mostly for ECoG arrays of relatively low electrode count [59]; [60], [61] and [62], whereas the pad-end of the array is inserted into the connector and a sliding arm is pushed in place, causing the connector to "grip" the array pad-end, as shown in Fig.3.2A.

anisotropic conductive film (ACF) was borrowed as assembly technology from the domain of liquid crystal displays. An ACF film is applied between the pad-end and a fan-out⁴ printed-circuit board (PCB) as an electrical link in the ECoG devices of [63], [52], [64], [47]. By applying a thermo-compression step, the ACF film is modified to provide electrical conduction only in the vertical direction (see Fig.3.2B).

Omnetics miniature connectors⁵ were soldered directly to ECoG arrays, either through-hole [51], [53] and [65] or SMD-connectors [54]. The pins of the through-hole connectors penetrate the flexible arrays via pre-designed holes (see Fig.3.2C), while SMD connectors are mounted on the top surface of the ECoG pads (see Fig.3.2D). Further, Baek et al. [53] designed an ECoG electrode array for a through-hole connector assembly, and the donut-shaped pads were connected by means of a novel electroplating technique directly to a fan-out PCB.

Alternatively, isotropic conductive epoxy was used in the works of [66], [67], [68] and solder-less snap-in connectors were applied to sandwich the pad sites of the electrode array [55].

While this assembly spectrum is ingenious, it reveals certain limitations for a multi-channel MEA of minimal connector-assembly area, the latter an essential prerequisite for in-vivo applications on freely-moving animals. Most ECoG devices containing up to 20 electrodes were

⁴the spacing between the output channels is larger than the one between the input channels

⁵Omnetics is a favorite connector brand (www.omnetics.com) for most research groups which record electrophysiological signal in-vivo due to its miniature size and until recently the smallest inter-pad distance and highest price of 30-50 \$ per piece (Hirose-connectors were recently introduced with even smaller inter-pad distance and < 1 \$ price, www.hirose.com).

connected with ZIF connectors or silver epoxy (higher electrode count would result in an extensive increase of assembly area). ECoG arrays with up to 64 electrodes were connected to a fan-out PCB either by anisotropic conductive film [53], which still ends up in a relatively large assembly area. Multi-channel ECoG MEAs (> 200 electrodes) – as presented in [51] and [65] – were connected directly by through-hole connectors, which penetrated the highly flexible array via ring-shaped connector pads. The latter approach enables the integration of maximal number of pads on a minimal assembly area. However, a custom-made array holder is required to fix the array in place during connector-assembly in [51], and a custom-made laser-structured ceramic platform in [65], which increases the overall complexity and reliability⁶ of the assembly process.

3.2 Flex-Rigid Microfabrication Concept

Alternatively, Ronald Dekker et al. [69] avoided soldering elements directly to a highly flexible micro-stack⁷, but carved a rigid Si-block from the wafer backside by means of DRIE etching and used it as interposer during mounting and assembly of connectors (see Fig.3.3). As thin flexible systems tend to roll and stick together, the whole device should be kept spanned to its mother wafer as long as possible by means of some straps. Provided polyimide is chosen as a flexible material for the overall device, it can also be used as building material for the straps. In sum, this solution requires a DRIE etch. Nevertheless, the time/costs invested in the DRIE process are well paid off during the assembly of electrical components by providing a flat and rigid soldering platform. Aside from DRIE, Guo et al. [70] integrated a PCB in the microfabrication flow of a PDMS-based microelectrode array, the PCB serving as a rigid interposer for the assembly of electrical connectors.

Micro-ECoG Challenges Although micro-ECoG technology has advanced very rapidly within the recent years, there are still basic goals to be met. Considering optimal array design, the effect of electrode size and inter-distance on the ECoG signal quality needs to be investigated, especially with respect to high-density devices (for electrodes smaller than 1 mm in diameter). Next, the ultra-flexibility of the ECoG arrays is challenging for the establishment of electrical connections – from the electrode sites to the inputs of the signal-amplifiers. Because the assembly of electrical connectors and components has been developed for fully rigid

⁶A major drawback of these donut-shaped connector holes of [51] is that when made too narrow the connector pins may crack their metallization and when too large the solder may flow in between the connectors pins and short circuit them.

⁷It took 3 years to grasp the do-not-solder-on-polyimide message for reasons stated in the coming Chapter.

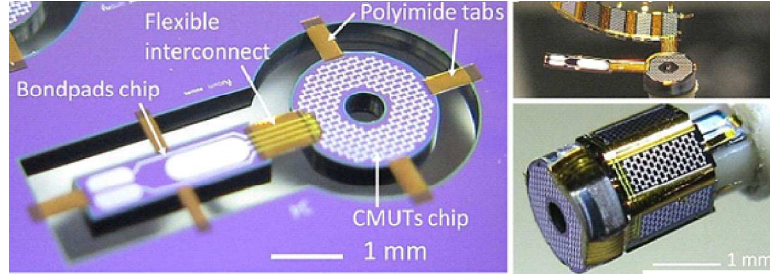


Figure 3.3: Flex-2-Rigid assembly approach: polyimide bridges mechanically hold the overall device to its mother wafer (left image). By disconnecting the polyimide bridges the device can be released from its wafer (top right image) and wrapped around curvilinear shapes (bottom right image) [43].

and planar devices, any out-of-plane buckling and even the slightest misalignment will most probably end up in contact loss. The in-vivo environment is a major challenge considering the long-term stability of an ECoG array in-vivo (long-life implants are a basic requirement for a BCI to enter the market). The ECoG in-vivo environment is represented by a relatively mild salt solution (saline at 37°C) which can diffuse into the flexible insulation film of the ECoG implant and account for the formation of parasitic short-circuits between the electrodes.

3.3 Mechanics of Flexible Materials

The flexibility of a given material is a function of its elasticity and geometry. The elasticity of a given material is defined by the Young's modulus E according to Hooke's law:

$$\sigma = E\epsilon \quad (3.1)$$

whereas σ is the the tensile stress per unit area applied at a specimen of that given material and ϵ is the elongation of the specimen defined as strain. Stiff materials possess large E magnitudes (ceramics and metals), flexible materials such as some classes of polymers have low E modulus, whereas elastomers such as silicone rubber have one of the lowest E moduli (see Fig.3.4, left image). For most metals E ranges between 45 GPa (for Magnesium) and 407 GPa (for Tungsten), while for polymers it belongs to a lower range – between 7 MPa to 4 GPa. Maximum elongation of metals is less than 5 %, whereas some elastic polymers can sustain strains greater than 1000 % [71].

Although Hooke's law defines a linear stress-strain function, this holds true for a limited region of the stress-strain diagram of a given material. As shown in Fig.1B three different stress-strain relationships are found for polymeric materials: brittle, plastic and highly elastic

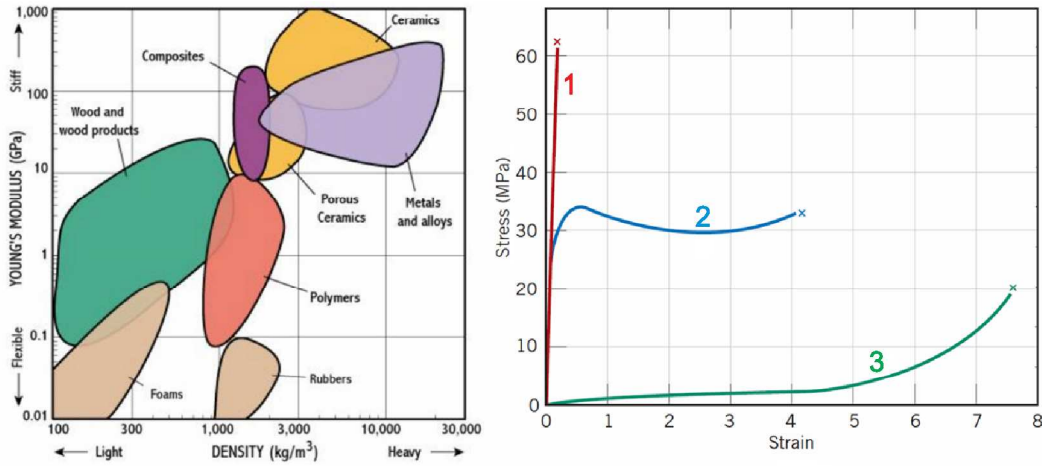


Figure 3.4: (Left) Young's modulus-density selective chart [76]. (Right) Strain-stress relationships of: (1) brittle, (2) plastic, and (3) highly elastic polymers [71].

ones (see Fig.3.4, right image): (1) brittle polymers behave similarly to Si as they undergo elastic deformation before fracture and follow a truly linear stress-strain relationship with a relatively steep slope i.e. a high Young's modulus; (2) plastic polymers behave similarly to metals – an initial elastic deformation is followed by plastic deformation before fracture; (3) some polymers show a truly elastic behavior – the stress-stress relationship has a low slope angle i.e. low Young's modulus; their strain-stress relationship is linear and reversible even for large strains [71], which is typical for silicone rubbers, applicable for stretchable biosensors [69].

The fact that polymers have much lower Young's modulus than Si (130 GPa for $< 100^\circ$ orientation [72]), made them attractive for the microfabrication of highly-flexible biomedical sensors: common polymeric materials are usually polyimide (2.5 GPa [73]), parylene (59 MPa [74]) and PDMS (0.8 MPa [75]). Polyimide exhibits a brittle-plastic stress-strain behavior [73], parylene undergoes plastic deformation [74], whereas PDMS is a highly elastic material.

Additionally to the elasticity of a given material, the geometrical design of a micro-device can highly influence its flexibility. This can be illustrated by a thin film subjected to mechanical bending. A narrow portion of a film, which is initially straight in the absence of any applied forces, is shown in the left image of Fig.3.5. Sections A_1B_1 and A_2B_2 define the top and bottom borders of the film portion. When the film is subjected to a bending moment M , these sections undergo transformation as indicated by the corresponding sections $A'_1B'_1$ and $A'_2B'_2$ so that the top section is elongated (stretched), while the bottom one is reduced in length (compressed). As stretching opposes compression, in the middle of the sample there should be a transition region, where no deformation occurs. This region is defined as neutral plane, indicated here by the section A_0B_0 . The neutral plane is the portion of the film, which does not experience any

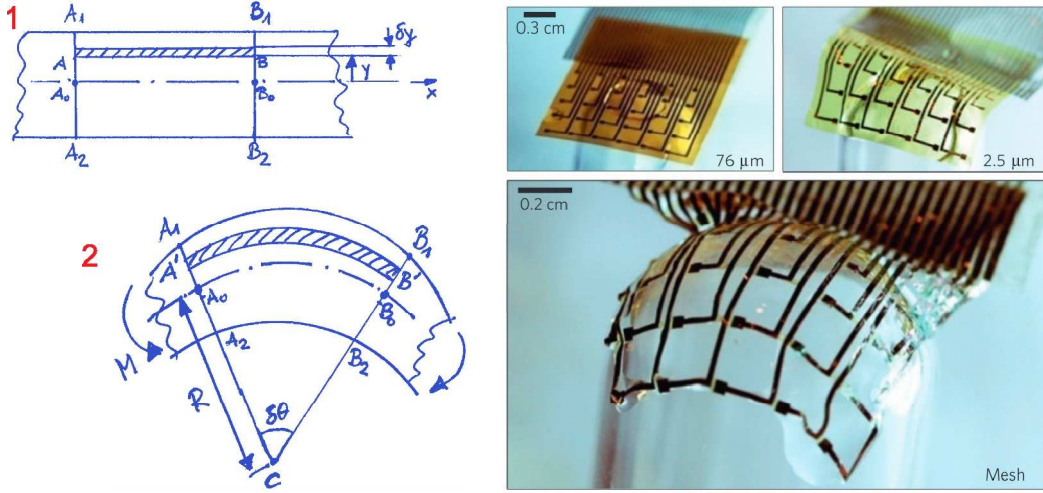


Figure 3.5: (Left) A beam subjected to mechanical bending: (1) before deformation all sections $A_n B_n$ are equal in length; (2) after applying a bending moment M along a circular arc only the $A_0 B_0$ neutral section does not experience any elongation; adopted from [77]. (Right) flexible electrode arrays of different thicknesses wrapped around a glass hemisphere – a 76 μm -thick sheet, 2.6 μm -thick sheet and 2.6 μm -thick mesh [78].

change in length upon bending [77].

Hence, the distribution of the strain ϵ_b will vary linearly within the beam thickness: from zero at the neutral section $A_0 B_0$ to \pm maximum at the top/bottom edge lines $A_1 B_1$ and $A_2 B_2$, respectively (Fig.3.5, 1 in the left image). As strain is defined as the relative change in length after deformation and all parallel sections $A_n B_n$ are equal in length prior deformation ($AB = A_0 B_0 = A_1 B_1 = A_2 B_2$), the strain within the beam ϵ_b is expressed as:

$$\epsilon_b = \frac{A'B' - AB}{AB} = \frac{A'B' - A_0 B_0}{A_0 B_0} \quad (3.2)$$

Provided upon application of a bending moment M the neutral section $A_0 B_0$ deforms in an arc of radius R , then $A_0 B_0 = \delta R$, and the corresponding strain ϵ_b from the above equation can be expressed as:

$$\epsilon_b = \frac{\delta\theta(R + y) - \delta\theta R}{\delta\theta R} = \frac{y}{R} \quad (3.3)$$

where R is the bending radius, $\delta\theta$ is the angle of the arc and y is the distance from the neutral plane to any point within the beam (see Fig.3.5, 2 in the left image). Provided the material of the beam is not elongated beyond the linear strain-stress relationship (see Fig.3.4), then the stress due to bending σ_b is defined as

$$\sigma_b = \frac{yE}{R} \quad (3.4)$$

with E being the Young's modulus of the beam material, which is assumed to be the same in tension as in compression [77], [79].

The bending moment M applied to the beam can be expressed by the normal force F acting at a distance y from the neutral plane; the normal force in turn can be related to the bending stress integrated over the area A . By applying Eq.5.6 the following relation for the bending moment M is obtained:

$$M = Fy = \int \sigma_b y dA = \frac{E}{R} \underbrace{\int y^2 dA}_I \quad (3.5)$$

whereas I is the second moment of inertia. Its value depends on the beam shape and the position of the neutral plane. For a rectangular cross section of width b and thickness d the second moment of inertia is $I = \frac{bd^3}{12}$ [79]. A detailed derivation of the bending moment and second moment of inertia is provided in the Appendix *Bending of a beam in an arc*.

Therefore, for the flexibility $\frac{1}{EI}$ of a beam⁸ the following relation derived from Eq.3.5. is obtained:

$$MR = EI \Rightarrow \frac{1}{EI} = \frac{12}{Ebd^3} \quad (3.6)$$

which indicates that in order to fabricate a flexible beam, not only a low Young's modulus E is preferred, but also a substantial reduction in thickness d should be aimed at [80].

Kim et al. [78] investigated the wrapping properties of neural flexible electrode arrays as a function of the film thickness (75 μm and 2.5 μm) and their design (sheet vs. mesh). The electrode arrays were wrapped around a glass hemisphere which has 6.3 mm radius of curvature, using only the capillary adhesion force of water between the glass and the flexible array. Some of the obtained results of [78] are presented in Fig.3.5: a relatively thick sample sheet (76 μm) remains completely flat, a reduction in sheet thickness to 2.5 μm makes the sample highly compliant but not fully adherent to the glass hemisphere. Only when the sheet is cut into a mesh-structure, removing the flexible material in between the metal electrodes, the sample becomes fully adherent to the glass hemisphere.

In summary, for a flexible electrode array to become compliant and adhere to the curvilinear surface of the cortex three major parameters should be tuned: reduction of the film Young's modulus, substantial decrease of thickness and last but not least introduction of specific cuts into the device.

⁸the inverse of bending stiffness EI

3.4 Electrode-Electrolyte Interface

Once the flexibility of an electrode array is tuned by an appropriate choice of parameters, the array's electrode material comes into consideration. By means of microfabrication a thin metal film can be embedded in the flexible polymer of the array. Upon implantation, placed directly on the dura surface, a metal surface comes in direct contact with the cerebrospinal fluid (CSF)⁹. In vitro, the cerebrospinal fluid is approximated by salty solutions based on sodium chloride (NaCl) such as saline¹⁰ or Ringer's solution¹¹. Therefore, the behaviour of the metal electrodes in-vivo resembles a metal-saline interface of unique impedance properties, much different from the electrode behaviour in a dry state. The electrode-saline impedance can be modeled by an equivalent electric circuit of passive electrical components such as capacitors and resistors. The impedance is characterized in vitro by electrochemical impedance spectroscopy by applying relatively small voltage sinus signals (10-20 mV) over the 1-10⁵ Hz frequency range. This section provides a concise summary of the metal/electrolyte interfaces based on [81].

Salty solutions, such as saline, belong to the class of electrolytes. They are solutions of ions, which can conduct an electrical current. In saline, the most common component is water. A single water molecule contains one oxygen atom and two hydrogen ones. The oxygen is more electronegative than the both hydrogen atoms, so that a strong electric dipole is formed (see Fig.3.6A). In the liquid state the dipoles of the water molecules are randomly oriented to each other (see Fig.3.6B) with a zero net charge. If NaCl is added to the water solution, water molecules will surround each single Na⁺ and Cl⁻ ion as shown in Fig.3.6C, because water molecules situated in the vicinity of the ions will be attracted by electrostatic forces originating from the ion charges. In case of a Na⁺ ion, the water dipoles will point toward it, while for a Cl⁻ ion the water dipoles will point outwards. Such water molecules are called primary waters of hydration and their number can vary from 1 to 5 water molecules per salt ion type. On top of this primary water layer, a second water-molecule layer (secondary waters of hydration) is situated to counterbalance the charge of the primary one, so that as a result a zero net charge is obtained. The percentage of the primary and secondary waters of hydration is very small when compared to the overall percentage of water molecules in a given electrolyte.

When a metal is immersed in an electrolyte, a metal/electrolyte interface is created, with adsorbed water molecules at its metal surface. If the metal is charged positively (e.g. by an external voltage supply), then the adsorbed water molecules will orient their dipoles inward the metal surface to counterbalance the positive charge of the electrode and vice versa (see

⁹CSF provides mechanical and immunological protection for the cortex.

¹⁰Saline is a 0.9 % w/v NaCl solution (9 g per liter) dissolved DI water.

¹¹Ringer's solution: 6.5 g NaCl, 0.42 g KCl, 0.25 g CaCl₂ and 1M sodium bicarbonate dissolved in 1 L H₂O.

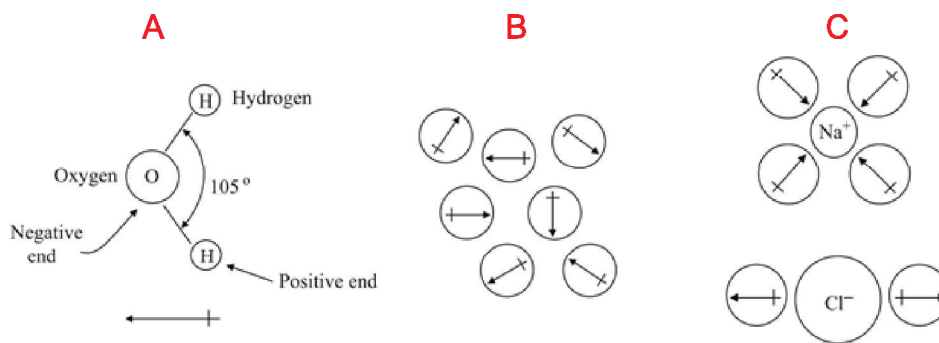


Figure 3.6: A: Water molecule with its corresponding dipole. B: Water dipoles in the bulk. C: NaCl solution with each ion type surrounded by a layer of water molecules [81].

Fig.3.7A). Except for water molecules, also ions can be adsorbed at the metal surface. The metal/electrolyte interface is not always stable (may corrode) and both anodic and cathode reactions can take place at it.

Several models have been developed for the metal/electrolyte interface with time. The first one is known as the Gouy-Chapman model: a positively charged metal electrode when immersed in an electrolyte will attract the negative ions of the electrolyte to its surface (counterbalance of charge). Despite the fact that the ions in an electrolyte are in constant thermal motion, there will be always a higher concentration of negatively charged ions at a positively charged metal surface.

Next, the Stern model was developed. It extends the Gouy-Chapman model by considering the adsorption of anions and cations at the metal surface. As illustrated in Fig.3.7B a positively charged metal electrode is counterbalanced by two types of ions: adsorbed anions and freely-moving anions. The size of an adsorbed ion can be approximated by its radius; the plane passing through the center of an adsorbed ion is defined as a Helmholtz plane. Outside the Helmholtz plane, there is a layer of freely-moving ions, called Gouy-Chapman diffuse double layer, which counterbalances the excess charge of the metal electrode.

The most recent model of an electrode/electrolyte interface is the Bockris-Devanathan-Mueller model: it includes all characteristics of the Stern model, but considers two additional issues: (1) adsorption of water molecules at the metal surface (and the corresponding orientation of their dipoles), whereas water molecules and ions constantly compete for free sites on the metal surface; the plane through the center of these adsorbed ions is called inner Helmholtz plane; (2) the charge of the adsorbed water molecules/ions is counterbalanced by counter-ions of opposite charge. These counter-ions are not adsorbed, but are surrounded by a layer of water molecules and the plane through their centers is called outer Helmholtz plane (see Fig.3.7C).

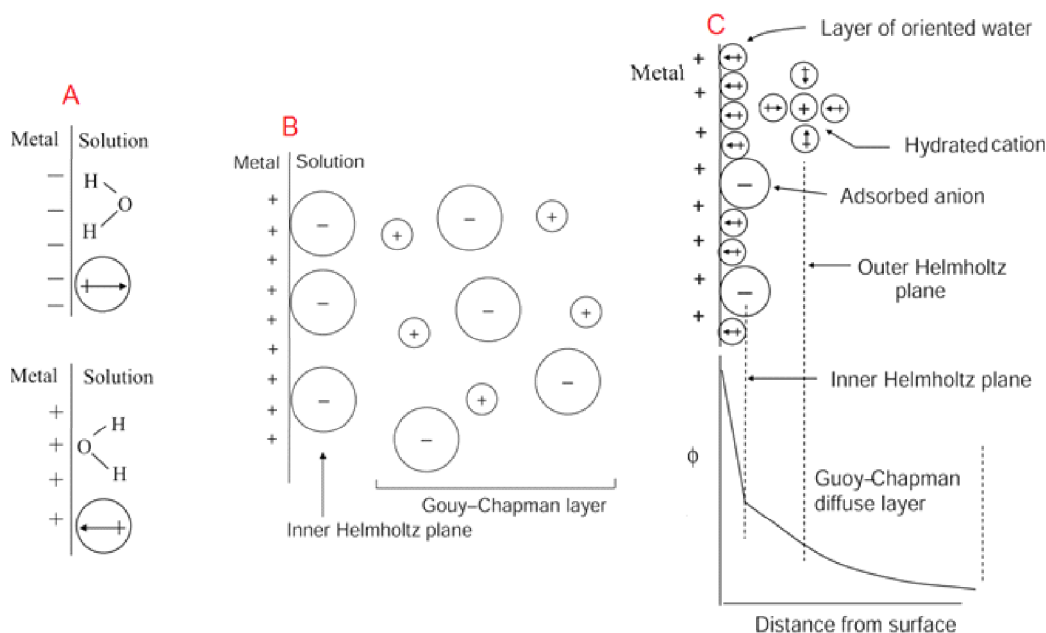


Figure 3.7: (A) Water molecules adsorbed on a metal surface. Their orientation depends on the electrode's charge; (B) Stern model of a metal/electrolyte interface; (C) Bockris-Devanathan-Mueller model of the electrical double layer of the metal/electrolyte interface [81].

The inner and outer Helmholtz planes constitute the electrical double layer (edl).

The electrode-electrolyte interface can be modeled by an equivalent electric circuit of passive electrical components such as capacitors and resistors. The corresponding electrical impedance is characterized in vitro by electrochemical impedance spectroscopy. In this electrochemical technique an alternating (AC) voltage is applied at the metal/electrolyte interface, the resulting AC current is measured and a complex impedance is obtained thereof. Originally, this technique was performed by using a Schering bridge: a $\delta C || \delta R$ impedance is varied until the bridge becomes balanced; by reading the values of C and R the equivalent impedance value of the metal/electrolyte interface is obtained. However, the bridge balancing was performed manually, which was a rather time-consuming task. It was therefore replaced by automated electrical instrumentation, which turned the electrochemical impedance spectroscopy into a powerful analytical tool for the study of metal/electrolyte interfaces, and corrosion behaviour of organic coatings deposited on metals.

Basically, electrochemical impedance spectroscopy (EIS) makes use of small voltage signals applied at the electrode (10-20 mV peak-to-peak sinus, $10^{-2} - 10^5$ Hz). By measuring the resulting current across the metal/electrolyte interface, the orientation and relaxation of the electrolyte dipoles can be characterized. The dipoles will orient themselves in the direction of the applied AC electric field. By sweeping the frequency the dipoles will constantly turn

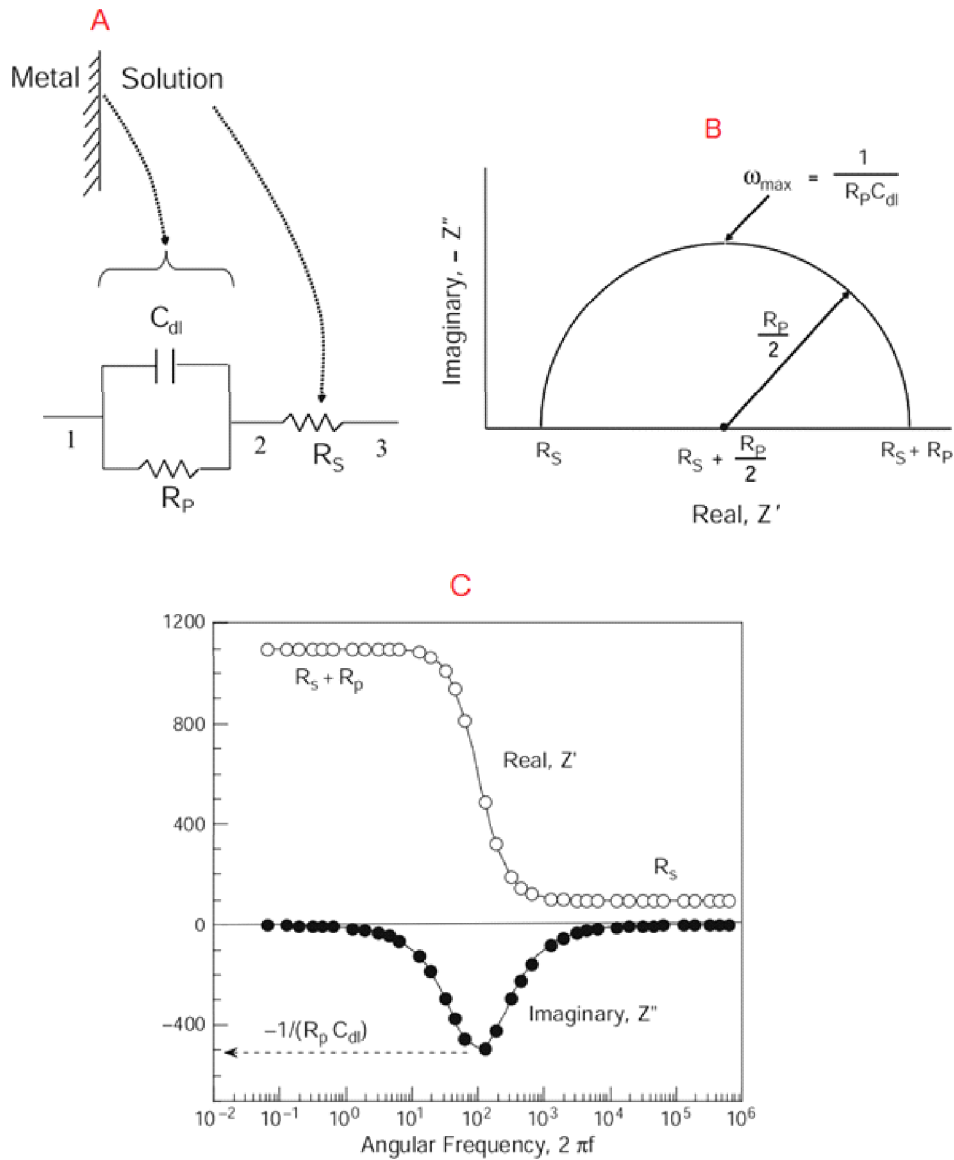


Figure 3.8: (A) Basic equivalent circuit for a metal/electrolyte interface; (B) Nyquist plot: real (Z') part plotted vs. imaginary (Z'') part of a metal/electrolyte impedance Z ; (C) Bode plot of a metal/electrolyte impedance Z [81].

back and forth following the changing electric field. However, the dipoles cannot follow exactly the applied frequency, which leads to a delay called relaxation¹². In EIS, the relaxation time t is defined as $t = R \cdot C$, with R being the resistance and C being the capacitance of the metal/electrolyte impedance, whereas R and C are in parallel. The impedance Z is obtained

¹²The electric field can induce electric dipoles if no permanent electrical dipoles are present.

from the applied voltage U and measured current I

$$Z(\omega) = \frac{U(\omega, t)}{I(\omega, t)} \quad (3.7)$$

with ω being the angular frequency. Once the impedance is obtained, then it can be expressed in terms of an equivalent circuit, as illustrated in Fig.3.8A. A basic electrical circuit, which describes the behaviour of a metal electrode immersed in electrolyte is comprised of a capacitor C_{dl} in parallel with a resistance R_p , connected in series with a resistance R_s . As the impedance Z describes the relaxation behaviour of the dipoles of the electrical double layer (see Fig.3.7C), C_{dl} represents the capacitance of the double layer, R_p accounts for the charge transfer across the double layer (i.e. across the metal/electrolyte interface) and R_s is the ohmic resistance of the electrolyte. Therefore, the interface impedance Z from Eq.2.8 can be expressed in terms of $C = C_{dl}$, R_p and R_s as follows

$$Z(\omega) = R_s + \frac{R_p}{1 + j\omega C R_p} \quad (3.8)$$

Furthermore, the impedance from the above equation can be expressed in terms of a real Z' and an imaginary Z'' part:

$$Z(\omega) = R_s + \frac{R_p}{1 + (\omega C R_p)^2} + j \frac{-\omega C R_p^2}{1 + (\omega C R_p)^2} \quad (3.9)$$

with

$$Z'(\omega) = R_s + \frac{R_p}{1 + (\omega C R_p)^2} \quad \wedge \quad Z''(\omega) = -\frac{\omega C R_p^2}{1 + (\omega C R_p)^2} \quad (3.10)$$

Combining Eq. 2.11 and 2.12 results in

$$\left(Z' - \left(R_s + \frac{R_p}{2} \right) \right)^2 + Z''^2 = \left(\frac{R_p}{2} \right)^2 \quad (3.11)$$

which corresponds to the equation of a semi-circle with a center situated at $(R_s + R_p/2)$ and radius $R_p/2$, as illustrated in Fig.3.8B.

By setting the derivative of Z'' from Eq. 2.12 to zero, the following expression is obtained

$$\omega_{max} = \frac{1}{C_{dl} R_p} \quad (3.12)$$

whereas ω_{max} is the apex of the semi-circle. Therefore, all three unknowns (C_{dl} , R_p and R_s) can be obtained from Fig.3.8B.

Alternatively, if the value of R_p is known, then C_{dl} can be determined from a linear plot of Z' vs. Z''/ω according to the following relationship

$$Z' = R_s - \frac{Z''}{\omega R_p C_{dl}} \quad (3.13)$$

whereas the slope of the above plot is $-1/(R_p C_{dl})$ and R_s the intercept.

A different way to present the impedance Z data is by means of a bode plot, whereas the the impedance magnitude $|Z|$ and phase angle ϕ are plotted in logarithmic scales against the angular frequency ω , with $\omega = 2\pi f$ as shown in Fig.3.8C. In the bode plot resistances appear as horizontal lines, while capacitors are slanted lines; the impedance magnitude $|Z(\omega)|$ and the phase angle ϕ as are defined as

$$|Z(\omega)| = \left\{ \left(R_s + \frac{R_p}{1 + (\omega C R_p)^2} \right)^2 + \left(j \frac{-\omega C R_p^2}{1 + (\omega C R_p)^2} \right)^2 \right\}^{1/2} \wedge \tan \phi = \frac{Z''}{Z'} \quad (3.14)$$

3.5 Scope of This Thesis

This PhD Thesis, conducted at INSTITUTE FOR MICROSENSORS, -ACTUATORS AND -SYSTEMS (IMSAS), University of Bremen, summarizes the development of a multi-channel ECoG MEA. The two-fold focus was set on: (A) establishment of a reliable electrical contact between the MEA and Omnetics connectors, and (B) investigation of how the diffusion of saline affects the MEA electrical performance (see Fig.3.9). The obtained results could prove beneficial for future implants, situated at the interface between the cortex and external electronics.

Fabrication of a multi-channel ECoG MEA A rigid interposer was monolithically integrated into the highly flexible device (see Fig.3.9.A). At the same time the electrode size was dictated by the application site: visual cortex of a Macaque. The electrode diameter was varied – 100, 300 and 500 μm – to provide first insights of how the ECoG signal scales with the electrode surface and a skull-facing reference electrode of much larger size was designed to ensure a high signal-to-noise ratio¹³.

The ECoG array was realized by spin-coating of polyimide, a golden metallization, and spin-coating of a second polyimide film. The wafer was etched away selectively from the backside to carve out a rigid interposer.

The electrical contact was optimized in several cycles. It was characterized by means of mechanical and electrical tests.

The ECoG electrodes were characterized in saline and the influence of electrode diameter on the electrode impedance was distinct.

The ECoG MEA was implanted on the visual cortex of a Macaque monkey (V1). The ECoG device was capable of recording distinct natural electrophysiological signals triggered by specific visual stimuli¹⁴. Preliminary tests of the electrode-size effect on the ECoG signal quality suggested an optimal electrode size for future ECoG array designs; measurements made

¹³The electrode design was suggested by Victor Gordillo-Gonzalez and the reference electrode by Prof. Kreiter.

¹⁴All in-vivo results were performed at AG Kreiter.

with the skull-facing reference electrode suggested a much higher signal-to-noise ratio than the one obtained with a common re-referencing technique. However, the long-term stability of the implanted array was limited to several months, as formation of parasitic shortcuts between different electrodes (also between non-neighbouring ones) was observed.

Accelerated soak tests in saline The formation of parasitic short-circuit contacts during the in-vivo tests motivated us to go for long-term stability tests. Either polyimide or parylene C were spin-coated as thin films on interdigitated planar capacitor structures ($10\text{ }\mu\text{m}$ interdistance). Cylinders were mounted on top and filled with saline. The samples were kept at 60°C for several months. A 10mV sinus (0.1 Hz - 100 kHz range) was applied across the coating and measurements of the resulting current offered insights into how the coating impedance changed over time upon water diffusion. An unexpected and highly promising coating material revealed an excellent water-barrier.

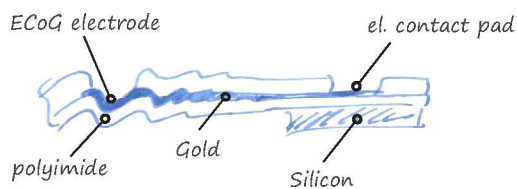
MEAs were fabricated with the promising material. The MEA samples were kept partially soaked in saline at 60°C for several months to simulate in-vivo environment at accelerated diffusion conditions. The obtained results offered insights into how both vertical and lateral diffusion influence the electrical characteristics of the MEA.

Foils of $5\text{ }\mu\text{m}$ thickness were fabricated out of the promising material and subjected to a set of physical investigations – FTIR, XRD and water-vapour permeation – in order to provide insight into chemical structure and crystallinity.

Thesis Structure

(A)

The making of ECoG MEAs



(1) establishment of microfabrication scheme

(2) optimization of el. contact between MEA & Omnetics

(3) Characterization of ECoG electrodes in water*

(4) Characterization of ECoG electrodes in-vivo

(B)

Soak tests in water*

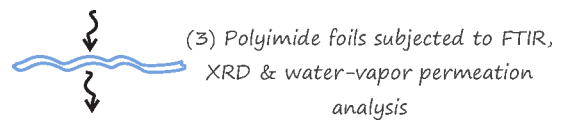
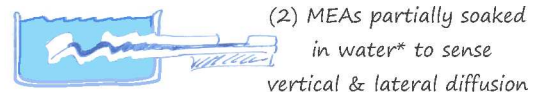
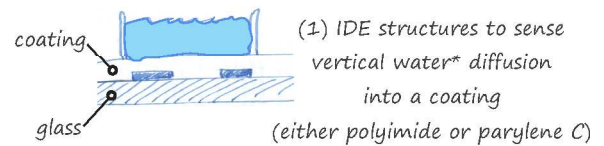
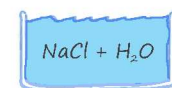


Figure 3.9: Thesis structure: (A) Microfabrication of a multi-channel ECoG MEA. (B) Accelerated soak tests on IDEs and MEAs, and physical investigations of polyimide foils. *water is here to be understood as saline.

Chapter 4

A Multi-Channel, Flex-Rigid ECoG MEA for Visual Cortical Interfacing

”Don’t undertake a project unless it is manifestly important and nearly impossible.”

Edwin Land

This Chapter proposes a multi-channel ECoG microelectrode array (MEA) of a flex-rigid nature. Its recording electrodes are embedded in a thin, flexible stack which enables them to warp around the semi-spherical cortical surface. The MEA connector-assembly region is fully rigid and flat to facilitate soldering of miniature SMD connectors. The content of this Chapter reflects predominantly the information published in [82].

High-density ECoG MEAs are promising signal-acquisition platforms for brain-computer interfaces envisioned e.g. as high-performance communication solutions for paralyzed persons. We propose a multi-channel microelectrode array capable of recording ECoG field potentials with high spatial resolution. The array has a 150 mm^2 total recording area. It has 124 circular electrodes (100, 300 and $500\text{ }\mu\text{m}$ in diameter) situated on the edges of concentric hexagons (min. 0.8 mm interdistance) and a skull-facing reference electrode (2.5 mm^2 surface area). The array is processed as a free-standing device to enable monolithic integration of a rigid interposer, designed for soldering of fine-pitch SMD-connectors. Electrochemical characterization revealed distinct impedance spectral bands for the 100, 300 and $500\text{ }\mu\text{m}$ -type electrodes, and for the array’s own reference electrode. Epidural recordings from the primary visual cortex (V1) of an awake Rhesus macaque showed natural electrophysiological signals and clear responses to standard visual stimulation. The ECoG electrodes of larger surface area recorded signals with greater spectral power in the gamma band, while the skull-facing reference electrode provided

higher average gamma power spectral density (γ PSD) than the common average referencing technique.

4.1 Design

ECoG electrode arrays are applied directly on the cortical surface, either above or below the dura¹. An ECoG MEA is coined as a “weakly-invasive” recoding device [4] because it still requires a surgery, but does not penetrate the cortical tissue in contrast to intracortical electrodes. Due to application site, ECoG electrodes record electrical signals of higher quality than EEG and are more robust toward artifacts than intracortical electrodes. These advantages make them highly promising signal-acquisition platforms of BCIs e.g. as communication tools for fully paralyzed persons. And yet, several basic questions need to be answered: optimal cortical location, most appropriate electrode size and interdistance [84]. All of these items are addressable with multi-channel ECoG systems. We present a multi-channel ECoG MEA designed for application on the visual cortex of freely-moving rhesus monkeys (*Macaca Mulatta*), the latter chosen because of the close resemblance to the human visual cortex [85]. The proposed device is of a flex-rigid nature – with flexible recording region and a rigid connector-assembly platform – to solve the challenge of soldering SMD connectors onto highly miniaturized and flexible electrode systems. Further, we incorporated three different electrode sizes/interdistances in the recording area to address the question of optimal electrode dimensions.

The Flex-Rigid Concept Current multi-channel ECoG systems are microfabricated as fully flexible devices by peeling them off from their wafer carriers [52], [47], [51]. The electrical connection to external pre-amplifiers is realized by means of either anisotropic conductive film (ACF) technology² [52], [47] or fine-pitch connectors of through-hole type [51]. The ACF is a straightforward, solder-less technology and yet inappropriate for multi-channel devices (> 100) on freely-moving animals because the MEA pads would be linked to a large-area, fan-out PCB. Fine-pitch connectors of Omnetics through-hole type, on the other hand, take up the smallest assembly area currently possible and yet require extreme precision during their mounting as

¹The dura matter is a dense, fibrous tissue attached to the inner surface of the skull. It is a membrane that envelops and protects the brain [83].

²An anisotropic conductive film (ACF) in form of tape/paste is sandwiched between the MEA and PCB pads. By applying heat and pressure the conductive particles of the ACF are only pressed between the MEA and PCB pads while the sites in-between remain non-conductive. This connection technology is applied between PCBs and flexible cables in liquid crystal displays, MP3 players and cameras [86].

their pins need to penetrate the flexible MEA pads through pre-designed holes³.

Alternatively, the challenge to assemble microsensors, for pressure and flow measurement around the tip of miniature invasive medical instruments⁴, was solved by the Flex-to-Rigid concept developed by Ronald Dekker et al. [69]. This concept enables the monolithic integration of microsensors on flexible carriers by applying polyimide-metal-polyimide stack in the very last steps of the planar microfabrication flow; at the same time the whole systems remains attached to the mother wafer by means of polyimide bridges⁵.

We implemented the Flex-to-Rigid concept to enable assembly of fine-pitch electrical connectors onto ECoG MEAs. Our flex-rigid electrode system is shown in Fig.4.1. Its recording electrodes together with their paths bundled in a flat cable are designed as fully flexible. As the flexible cable enters the connector-assembly region, a rigid block is introduced underneath to turn it into a flat and stable platform for the assembly of SMD connectors. The MEA is attached to the mother wafer by means of flexible straps, and can be released by cutting through the bridges e.g. manually by scalpel.

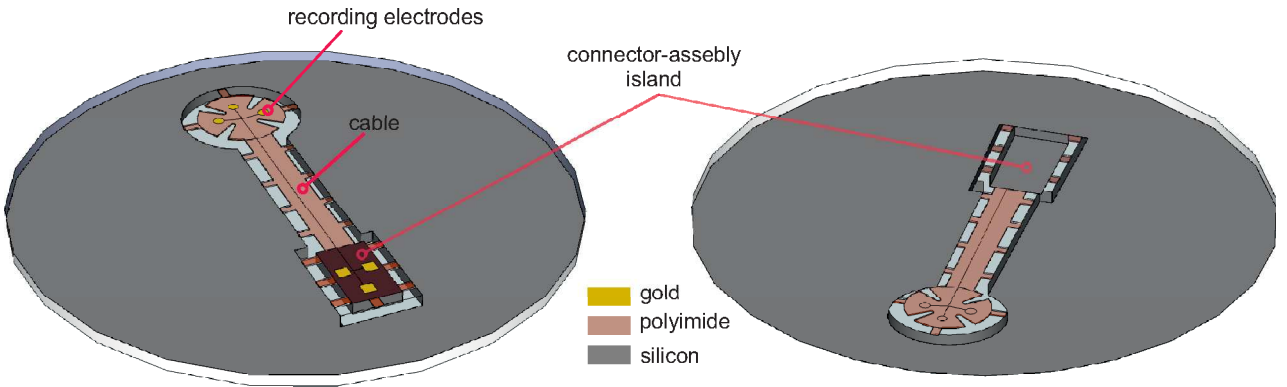


Figure 4.1: The ECoG MEA is realized as a flex-rigid system with flexible recording area, flexible cable, and rigid connector-assembly block. The MEA linked to its mother wafer by flexible straps.

The CAD-layout of the proposed ECoG MEA is depicted in Fig.4.2A. It consists of a circular signal-acquisition area (20 mm wide), a narrow cable (6 mm wide) and a rectangular connector-

³During mounting if the pad holes are too small, the pad metallization may get broken; if the pad holes are made larger, this may offer enough space for the solder paste to flow in between the pins and cause short-connections.

⁴diameter from ca. 0.3-2 mm

⁵A similar concept is applied during the fabrication of flexible PCBs; yet the latter are limited in their pattern resolution and therefore inappropriate for multi-channel ECoG MEAs.

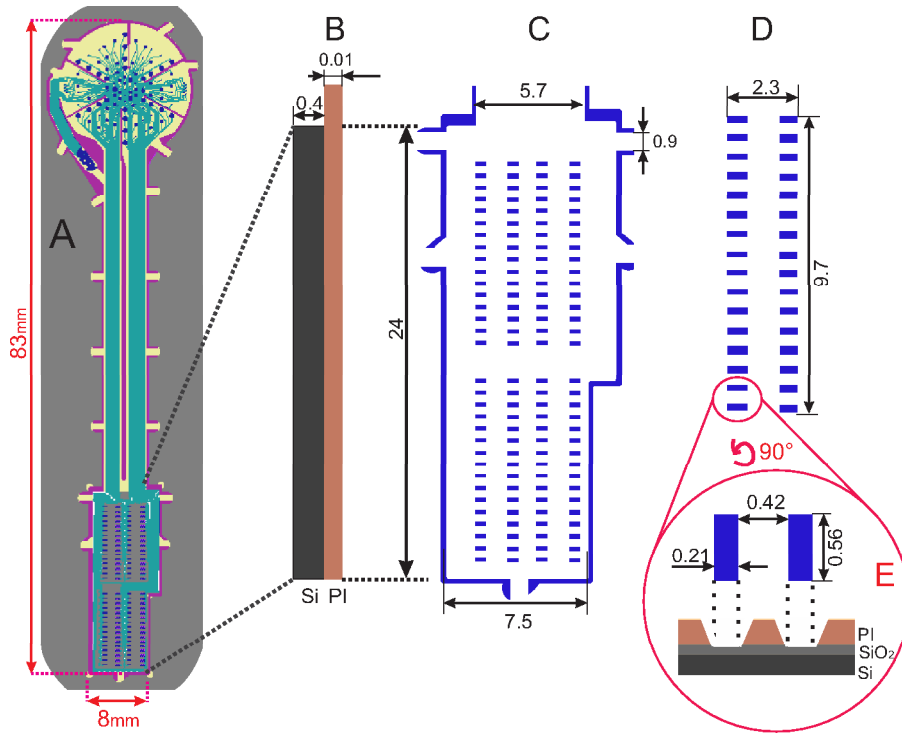


Figure 4.2: CAD design of the MEA connector-assembly platform: (A) MEA overview; (B) Platform side-view; (C) Platform top-view; (D) Pad layout of an SMD Omnetics connector; (E) Pad size and interdistance of the same. All dimensions are in mm.

assembly island (8 mm wide). The array is 83 mm long, mostly dictated by the cable length, which is needed during implantation in order to position the signal-acquisition area away from the site of craniotomy⁶.

The CAD-layout of the connector-assembly platform is presented in detail in Fig.4.2B,C,D. Polyimide serves as a flexible material which enables a monolithic transition from the MEA cable (5.7 mm-wide) to the rigid platform, the latter strengthened on its back-side by a silicon block. The connector platform is designed for 4 SMD Omnetics connectors, each of 32 pins, which results in a 200 mm² total surface area. A soldering pad has 210 μm x 560 μm area. The minimal distance between two pads is 420 μm . The polyimide on the areas destined for the pads is intentionally removed, so that Si/SiO₂-metal pads can be realized, which ensures reliable solder joints as demonstrated later in this Chapter. Flexible polyimide straps (0.9 mm wide) mechanically connect the platform to its mother wafer. This facilitates mechanical handling during mounting of connectors and in-vitro characterization⁷.

⁶A portion of the skull bone is removed. The MEA recoding area is flipped into skull-cortex gap, far enough from the removed portion to ensure high signal quality during ECoG recoding sessions.

⁷The MEA will tend to roll/stick unless spun to its mother wafer.

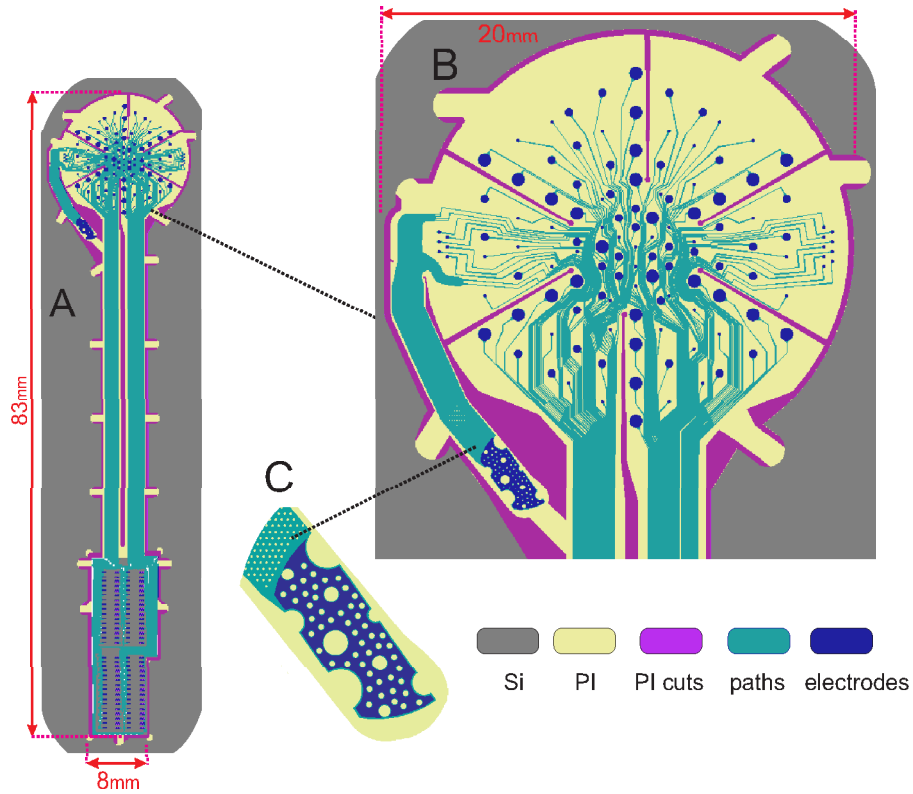


Figure 4.3: CAD-Layout of the MEA recoding area: (A) MEA overview; (B) 124 circular channels; (C) the reference electrode.

Electrode Design The CAD-layout of the MEA recoding region is presented in Fig.4.3. It contains 124 circular recoding channels and a reference electrode. Most of the circular electrodes are positioned on the edges of concentric hexagons, while the reference is connected with a 2 mm-wide cable to the recoding area. Eventually the reference electrode will be bent and fixed to the MEA backside. The electrodes and their paths are embedded in polyimide (PI). Several radial PI cuts perforate the MEA and enable it to attain a hemispherical shape without any undesired folds. Beside the radial cuts, there are curvilinear PI cuts, which define the circular edges of the array, the outlines of its reference electrode and the borders of several flexible straps, which connect the array in the final fabrication step to its carrier wafer (Si).

Fig.4.4 shows the distribution of MEA electrodes together with their sizes and interdistances. The recoding electrodes are 100, 300 and 500 μm in diameter. Most of them (109 in number) are situated on the edges of six concentric hexagons. The spacing between the hexagons is varied as follows: 800 μm for 1-2; 1200 μm for 2-3 & 3-4 and 1800 μm between the remaining ones. The ECoG electrodes are designed in three different sizes/interdistances to investigate the influence of their surface area on the coherence of ECoG signals.

Additionally, a few electrodes, 100 μm in diameter, of 400 μm interdistance, are arranged

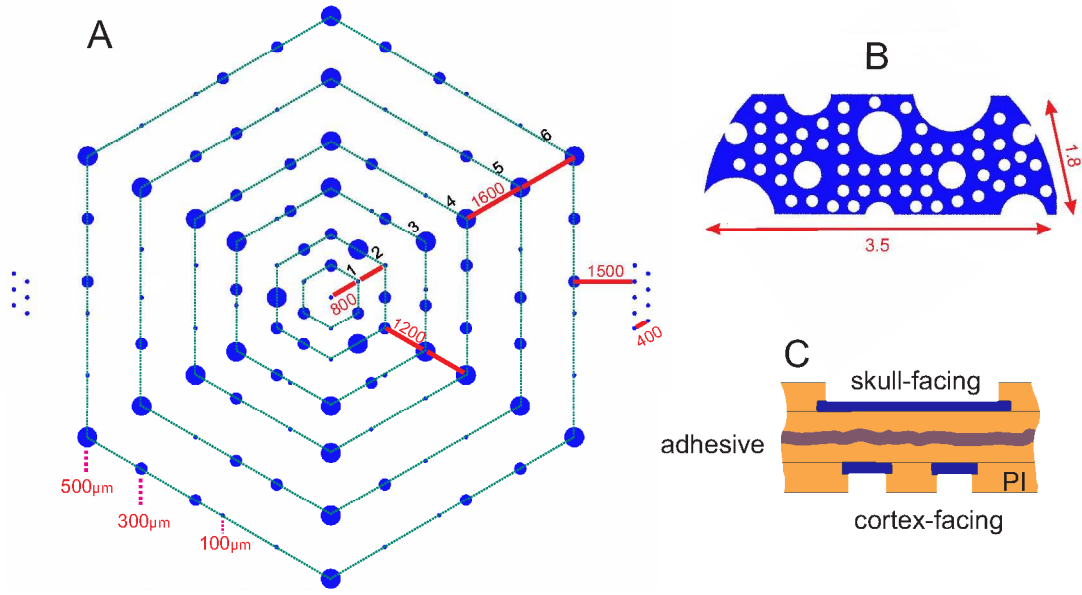


Figure 4.4: (A) Distribution of 124 recoding electrodes: 109 are situated on concentric hexagons (recoding channels), and the rest arranged in groups for spatial frequency tests; (B,C) The reference electrode will eventually become skull-facing (compare with Fig.4.3C).

in two groups and situated 1500 μm from the outermost hexagon (6 to the left and 9 to the right). These two electrode sets are planned for high-resolution spatial frequency tests.

The MEA's own reference electrode is of 2.5 mm² surface area, orders of magnitude larger than any recoding channel to ensure high signal-to-noise ratio. It has an irregular shape which contains several circular holes to prevent the formation of mechanical stress peaks and metal cracking during handling (Fig.4.4B). The reference electrode will be realized out of a 300 nm-thick gold (Au) film in the same metallization plane as the circular electrodes. After completion of all manufacturing steps the reference electrode will be bent and fixed with an adhesive to the backside of the MEA to face the skull during in-vivo recordings (see Fig.4.4C).

The integration of radial cuts in the electrode layout increases the design complexity of the electrode paths which connect the electrode sites with the connector pads (see Fig.4.3B). If the radial cuts originate at some distance from the array's center and run outwards, most of the electrode paths (15 μm wide and with 15 μm inter-path distance) must pass through a relatively narrow cut-free region, situated in the middle of the array layout. The origin of each cut is shaped as a circle of 200 μm diameter to distribute uniformly mechanical stress (during mechanical handling or implantation) over the circle circumference and thus prevent the formation of mechanical cracks.

4.2 Development of Fabrication Process

4.2.1 Microfabrication

A Silicon wafer served as a substrate, U-Varnish-S polyimide as a flexible encapsulation film and gold as a metallization layer. The choice of these materials was influenced by the work of Rubehn et al. [51] – the first large-area ECoG MEA tested in-vivo⁸.

Trials related to the establishment of the microfabrication flow are summarized in Fig.4.5.

(1) A 380 μm -thick silicon wafer, of 4" diameter, served as a substrate, whereas 380 μm thickness was preferred over 550 μm for shorter DRIE etching. A thermal oxide of ca. 750 nm thickness was grown on the wafer to serve as DRIE-etch-stop layer.

(2) An U-Varnish-S polyimide, from UBE Europe GmbH, was spin coated on the wafer: 30s@250rpm for dispensing; 30s@1500rpm for spreading; 40s@3000rpm to obtain a thin film. The polyimide film was kept for 10min in a desiccator to remove micro-bubbles and then soft-baked on a hotplate for 10min@80-120°C & 5min@120°C. Then the polyimide was fully cured – at first in a Centrotherm Belt Furnace in N₂ atmosphere, the oven situated outside of the clean-room⁹ and then we transferred the curing process to a wafer-bonder machine, in vacuum, the machine situated inside the clean room¹⁰. As during the first curing shot large bubbles formed, enclosed between the wafer and the polyimide film, we introduced the adhesion promoter VM-651 from HD Microsystems¹¹ prior to the polyimide spin-coating. The result was a bubble-free U-Varnish-S film of 5 μm final thickness.

(3) Platinum was the first metal choice because of its high resistance to oxidation/corrosion. And yet, we experienced troubles using Aqua Regia to structure a 300 nm-thick Pt film into exceptionally long, narrowly spaced multi-channel tracks (ca. 8 cm long, 15 μm pitch, 128 tracks, see Fig.4.4). There were always some Pt-islands left (> 3 mm in diameter) which led to short-circuits. Treating the Pt-surface with an Ar-plasma prior to the wet etch did not help.

Gold was sputtered instead – a noble metal, 1:1 mask transfer during wet etch, high conductivity. Three wet-etch solutions were tested: (1) Cyanide-based¹², (2) Au etch 200@50°C from NBT Technologies and (3) KI+I₂+Glycerin. The cyanide solution had the minimum underetch (almost zero), however it is highly toxic. Au etch 200 resulted in a negligible underetch of <0.5 μm , however sometimes particles precipitated from the solution and led to severe contaminations. The third solution had an 0.5-1 μm underetch, was easy to apply and discard.

⁸Rubehn had also fabricated a 128-channel ECoG MEA for Andreas Kreiter's research group.

⁹Centrotherm Belt Furnace, Centrotherm, DE, 450°C peak temperature, 80 mm/min belt speed

¹⁰Substratbonder SUESS SB6, SUESS MicroTec, DE

¹¹The VM-651 was diluted in water (0.1 ml in 100 ml), spin-coated at 4000 rpm and baked for 120s@120°C.

¹²200ml Au etch plus from Candor Chemie : 2g potassium cyanide : 1L water

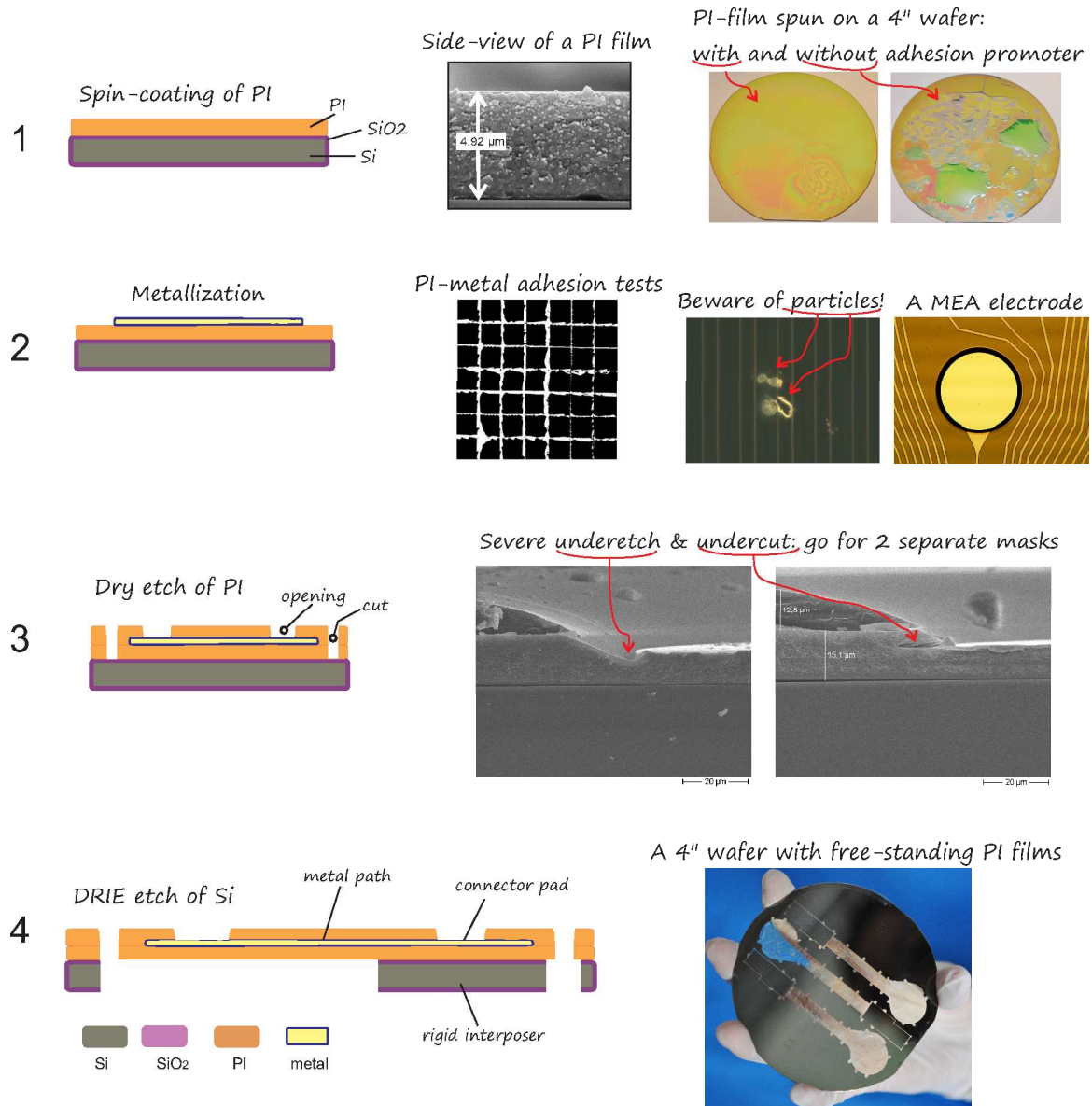


Figure 4.5: Preliminary fabrication steps of a flex-rigid ECoG MEA.

The polyimide-gold adhesion was investigated by means of cross-cut tests (see Fig.4.6.left): all samples were heated on a hotplate (120s@120°C) to demoiaturize the polyimide and then divided into three groups (Fig.4.6.Left). The PI/Au stack was scratched in a right-angle lattice and an adhesion tape was applied to remove any residues. The white pixels corresponding to the scratched areas (Fig.4.5.2) were counted with a Matlab Image Processing toolbox. Alternatively, wedge wire-bonding was used: after attachment of the first bond and raising the wedge to form a loop, the aluminum bond detached from the metal-polyimide sample thereby removing partially the gold film from the polyimide (see Fig.4.6.Right). Both cross-cut and wire-bonding tests revealed samples without any pre-treatment (sample type 3) to have lowest

	#1	#2	#3
HP 120s@120°C	x	x	x
VM-651	x		
O2 plasma		x	
20nm Ti	x	x	
300nm Au	x	x	x
pixel # [%]	16.2	18.7	19.8

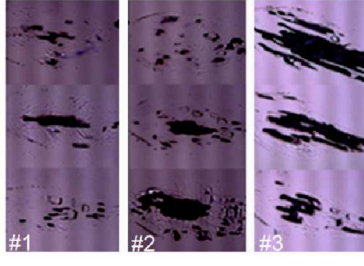


Figure 4.6: (Left) Cross-cut adhesion tests at the PI-Au interface; (Right) Wire-boding tests.

PI-Au adhesion. On the other hand, PI-Ti-Au sample had higher adhesion (type 1 & 2), as expected. In the end, we preferred type 2, because 1 could introduce some particle contamination. In future, instead of scratching, the cross structure should be transferred in the Au-film by wet etching.

(3) A second polyimide film was spin-coated and cured (see Fig.4.5.3). To open the ECoG electrodes/pads and define the PI cuts, the polyimide was etched in a O_2+CF_4 plasma in a STS ICP tool¹³ at an etch rate of $0.5 \frac{\mu m}{min}$ and the masking photoresist was removed in an NMP solution. However, in order to open the electrodes & pads a $5 \mu m$ -thick PI should be removed, while for structuring the PI cuts a $10 \mu m$ -thick PI should be etched away. Etching all structure types at once and applying afterwards an NMP resist stripper led to severe underetch/undercut at the electrode sites. Therefore, we split the PI etching in two – at first only the PI cuts were pre-etched up to a $5 \mu m$ depth, and then PI cuts+electrode sites+pads were opened – and also exchanged NMP with AZ100 resist stripper¹⁴.

(4) The DRIE-etch was performed in two steps: (1) the wafer backside was pre-etched for 80 min up to ca. $300 \mu m$ average depth, it was unloaded and a blank wafer (mechanical stabilization) was fixed with a silicone paste (heat sink, WLP 035, Fischer Elektronik) dispensed on the edges the MEA wafer (front side) to prevent the pins of the STS etcher to punch through the MEA. The wafer was loaded again and fully etched (ca. 40 min). The support-wafer was detached and the paste was removed manually with an acetone-soaked cloth.

Later, the blank wafer+silicone paste were replaced with a $130 \mu m$ -thick “Adhaesionsfolie” i.e. a soft PVC-based foil which adheres on a surface by means of electrostatic forces¹⁵. This foil was applied to the front surface of the pre-etched wafer. The DRIE process was transferred to an Alkatel tool (no pins). Afterwards the foil was removed manually with IPA¹⁶.

¹³800 W coil power, 25 W plate power, 40 sccm O_2 flow, 8 sccm CF_4 flow

¹⁴As NMP is a solvent contained in the polyimide precursor, it attacked the cured polyimide film.

¹⁵www.modulor.de/Kunststoff-Gummi/Klebfolien-und-Adhaesionsfolien/Adhaesionsfolien

¹⁶Volker Biefeld came up with the electrostatic foil. His foil application/removal art is highly appreciated ☺.

4.2.2 SMD Assembly

The MEA surface was activated in O₂ plasma. A Sn-58Bi solder paste¹⁷ was manually dispensed on the 128 MEA pads through a tip of 250 μm inner-diameter using a fluid dispenser under pressure¹⁸.

A multi-purpose die bonder (Fineplacer¹⁹) was used for the assembly of connectors. A 5 mm-thick pre-designed Al block with a hole in its center²⁰ was placed on the hotplate of the Fineplacer. The MEA rigid island was positioned on the Al block and it was vacuum sucked. A 32-pin SMD-connector²¹ was picked up by the Fineplacer's lever arm. The connector legs were aligned to the MEA pads with the help of the Fineplacer vision alignment system (two images superimposed on each other).

Fig.4.7 shows the solder heat-profile²² which contains several heat regions²³ with temperature measured on the Fineplacer hotplate. To note is that the temperature measured on the MEA pad surface is slightly lower – 40s@100°C, 40s@129°C, 30s@140°C and 20s@165°C.

After soldering, the flux residues are rinsed as soon as possible (Flux Remover, followed by IPA) and an UHU adhesive²⁴ is applied around the connectors through a syringe under pressure. The UHU adhesive is applied in 2-3 layers, whereas after every layer the MEA is heated on a hotplate for ca. 10min@90°C to let the adhesive flow under the connector and also to ensure high mechanical stability. Images of the connector-assembly process are shown in Fig.4.8.

Eventually, the ECoG array is released from its carrier wafer by manually cutting the polyimide straps using a scalpel. Its reference electrode is bent and fixed to the middle of the MEA signal-acquisition area (backside) by a biocompatible, high-temperature and moisture-resistant adhesive²⁵ to realize a skull-facing reference (see Fig.4.9).

¹⁷20-38 μm solder powder size, LFM 65W, Almit GmbH, Michelstadt, Germany; eutecticum at 139°C.

¹⁸Nordson EFD, 1000 DVE, 2 bar, 0.5-1 s

¹⁹FINEPLACER@pico ma, Finetech GmbH & Co., KG, Berlin, Germany

²⁰The Al block was placed between hotplate and MEA to focus the heat to the assembly platform.

²¹Omnetics, Nano Strip Series, NPD type, A71350-001, Omnetics Connector Corporation, USA

²²Motto: reduce the heat flux to a minimum to spare the thin-flexible MEA portions, cool down slowly.

²³Originally, we started with a rather long heat-profile (to be on the safe side) and then reduced its duration step by step. Thereby, during every trial we used a dummy MEA with dispensed solder paste (no connector) and monitored the how the paste behaves with temperature increase.

²⁴UHU plus endfest 300, UHU GmbH, Germany

²⁵Polytec EP653, Polytec PT GmbH, Waldbronn, Germany

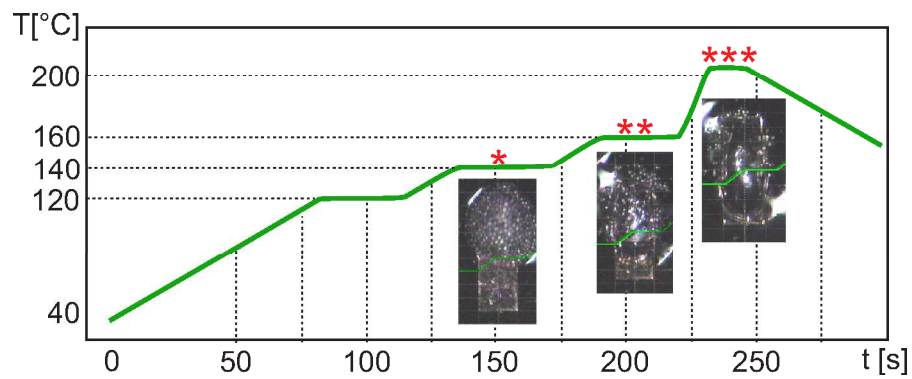


Figure 4.7: Heat profile of a Sn-58Bi solder paste (hotplate temperature): (*) the solder flux flows outwards; (**) the solder paste begins to melt, flows under the connector legs and the connector moves to align itself to the MEA pads, (***) the solder paste is fully molten.

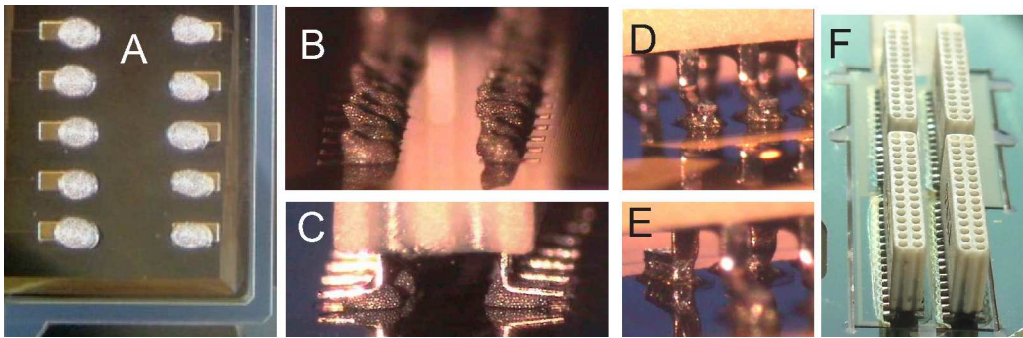


Figure 4.8: (A,B) The solder-paste dispensed slightly off-pad to ease connector alignment; Omnetics connector before (C) and after heating (D,E,F).

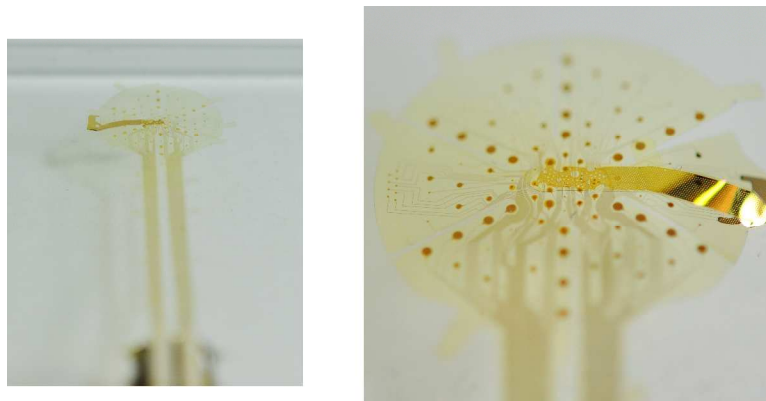


Figure 4.9: The reference electrode after being fixed to the backside of the MEA.

4.3 Troubleshooting: a Reliable Electrical Contact

After establishing the soldering heat-profile we stuck into a reliability problem. The soldered Omnetics connectors had many broken electrical connections. It took us three microfabrication runs to pinpoint the source of the problem²⁶, as illustrated in Fig.4.10.

A: The very first run borne a 300nm-thick golden pad situated on a polyimide (PI) layer, the PI enforced by a Si/SiO₂ interposer. The assembly of 32-pin connectors by means of soldering led to many broken connections (> 50%) which was explained by the insufficient thickness of the gold film – the 300nm-thick Au film diffused completely into the solder paste upon heating. We employed a silver paste instead²⁷ for the assembly of 4x 32-pin male connectors. Then we plugged the female counterparts to measure the connections – only 6 out 128 were broken. However, upon unplugging of females out of the males more than 50 % of the silver-joints failed²⁹ (see Fig.4.11, left image, sample A). To note is a relatively high force is needed to unplug an Omnetics female from a male – ca. 12 N for a 32-pin configuration³⁰.

B: We increased the thickness of the gold pads by means of electroplating – up to ca. 2,5 μm . And yet, this improvement did not work either. This time up to 25 out 32 connections were broken (see Fig.4.11, left image, sample B). Upon scratching the gold surface with a needle, almost the whole pad metallization was ripped off the polyimide surface which spoke for weak adhesion at the PI-pad interface³¹. This was highly surprising, as we measured the pad-metal adhesion directly after metal deposition and even improved it with a Ti inter-layer (see Fig.4.6). It was neither an effect of aging, which we confirmed by applying a scotch tape on an over-1-year-old wafer/PI/Au sample (with no top polyimide). Therefore, the only explanation was the 450°C curing step of the second polyimide, situated on top of the Au layer and later opened at the pad. During this curing process both the top and bottom polyimide expanded much more than the Au film (mechanical stress), breaking thereby the chemical bonds at the PI-Au interface.

C: In order to reduce the occurrence of mechanical stress at the PI-Au interface, we simply removed the bottom PI. In this way the Ti/Au stack was situated directly on the rigid Si/SiO₂

²⁶The process of finding out the reasons for the broken connections are described here in detail for the sake of clarity, as this topic is highly underestimated (in my experience).

²⁷The silver paste Elecolit 3653²⁸ was dispensed on 128 PI/Au pads. The paste dispensing was performed manually, using a syringe (100 μm diameter, Nordson EFD) under pressure (3 bar, 3 s) through fluid dispenser. The silver paste was cured for 6min@120°C on the FINEPLACER hotplate.

²⁹Another disadvantage of silver pastes in general is that they can lead to short-circuits as they cannot flow (in contrast to solder paste)

³⁰see Appendix for the details of this measurement.

³¹Additionally, we performed peel tests – one could easily peel the Au pads off the MEA.

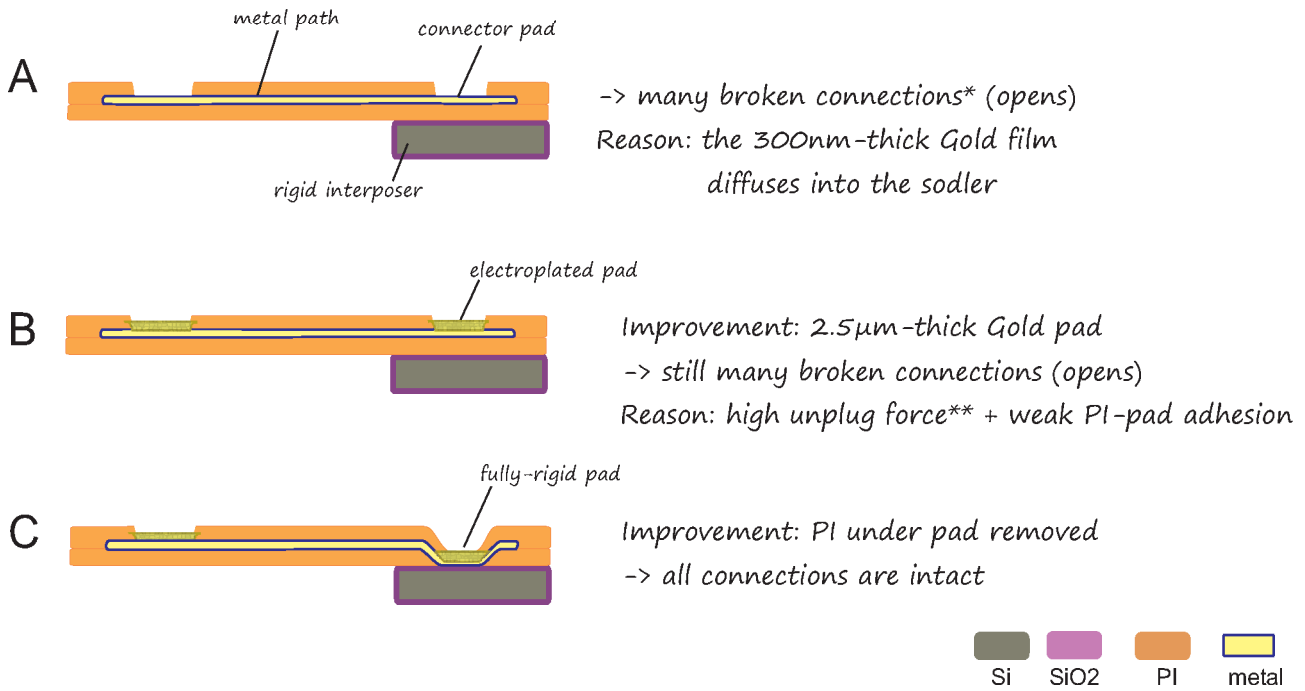


Figure 4.10: Establishing a MEA with reliable platform for SMD assembly of connectors. (A) Neither a 300nm-thick Au soldering pads realized on PI, (B) nor a 2.5μm-thick Au pads deposited onto PI provided reliable contact solution. (C) Au pads on the Si/SiO₂ interposer. *connection is here to be understood as electrical contact and **unplug force is related to the force needed to remove a female connector out of its male counterpart.

interposer (their design and fabrication is presented in the following Section). Electrical tests revealed zero broken connections³². Additionally, we performed pull tests to confirm our assumptions about the loss of adhesion at the PI-pad interface. This sample reached the maximum force-at-break during pull tests (as shown in the left image of Fig.4.11, sample C). Details of this pull tests are presented in the Appendix. To note is that the force-at-break for the sample C was increased by 10x by making the Ti layer even thicker³³ – from 20 nm to 50 nm – explained by the partial diffusion of Ti film into the gold layer during soldering.

³²To note here is that the MEAs polyimide-cured in the Centrotherm oven outside of the clean room exhibited up to 3 broken connections out of 32 which was due to the rather short curing cycle of the polyimide (during the curing of the top polyimide, solvents diffused out of the bottom polyimide and made the PI pads crack and oxidize at the cracks). Instead, MEAs with fully cured polyimide (in vacuum) had 0 broken connections.

³³Tobias Tessmann demonstrated it by means of pull tests.

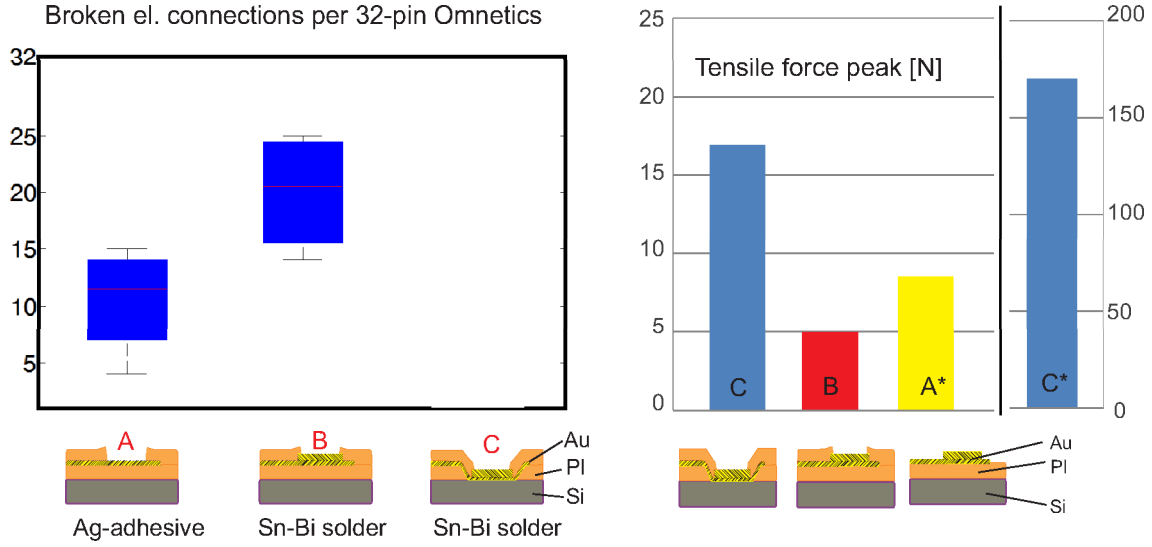


Figure 4.11: (Left) Electrical tests, performed on 32-pin Omnetics connectors soldered to MEAs with different pad types, reveals pad type C as most reliable; (Right) Pull tests performed on Omnetics connectors reveal pad type C of maximum force at break. Sample C* denotes pull tests performed on C-type pads, additionally strengthened by an UHU adhesive

4.4 Final Fabrication Flow

Fig.4.12 shows the final fabrication flow of the ECoG MEA, developed for fully rigid Ti/Au pads. A 750nm-thick thermal oxide is grown on a 4", 380 μ m-thick silicon wafer. A 1.8 μ m-thick AZ1518 photoresist mask³⁴, defining the array's flexible and rigid regions, is realized on the wafer backside. The mask is transferred into the oxide beneath by dry etching (CF₄-RIE plasma, ALCATEL 601E). The resist is stripped (5min@50°C, AZ100, MicroChemicals, Germany) and the wafer is cleaned in Caro's acid. Next, the wafer front side is spin-coated with an organosilane adhesion promoter VM651 for 60s@4000rpm and baked on a hotplate for 120s@120°C, followed by a spin-coating of an U-Varnish polyimide film at 3000 rpm for 40 s. The polyimide is soft-baked on a hotplate for 5min@80-120°C & 5min@120°C and then cured in a N₂ atmosphere³⁵. In this way the first polyimide layer is realized on the wafer front-side (see Fig.4.12.1).

Next, the wafer is cleaned by IPA, water-rinsed and dried for 1h@120°C in an oven³⁶. The polyimide surface is activated in O₂ plasma (500 sccm, 500 W, 30 s, 400 PlasmaSystem) to pro-

³⁴MA6 mask aligner, Suess, Germany; AZ726MIF developer, MicroChemicals, Germany

³⁵10min@450°C peak, Centrotherm Belt Furnace, Centrotherm, Germany; The curing was transferred later to a Substratbonder SUESS SB6, SUESS MicroTec, DE (in vacuum).

³⁶We performed this step for polyimide films curing outside of the clean-room. As we later shifted the curing to the clean room, we just skipped this step

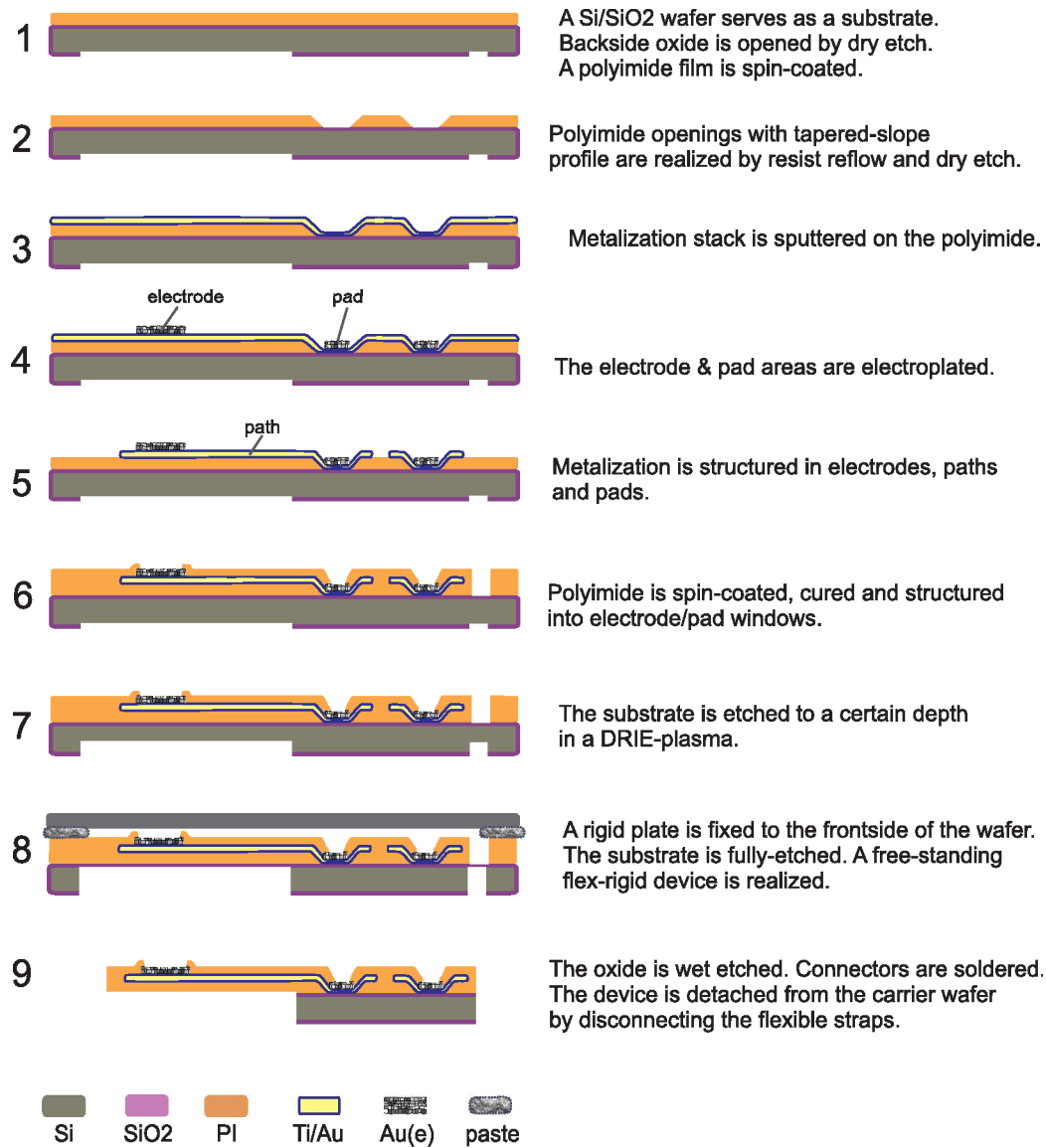


Figure 4.12: Final fabrication flow of the flex-rigid ECoG array, which has fully rigid Ti/Au pads situated on the Si/SiO₂ interposer.

mote high photoresist adhesion. A photoresist is spin-coated and structured into rectangular windows (10 μm -thick AZ9260 resist, AZ400K developer). The photoresist is then thermally re-flowed for 1h@120°C in an oven to obtain a smooth step profile³⁷. This resist profile is transferred in the polyimide layer situated underneath by O₂+CF₄ RIE plasma (11 min, 40 sccm O₂, 8 sccm CF₄, 800 W coil, 25 W plate, STS ICP tool). The resist is eventually stripped (15min@50°C in AZ100). Hence, rectangular windows with a tapered slope are realized in polyimide; these windows define the regions where soldering pads will be situated (see Fig.4.12.2).

³⁷Refer to the Appendix for more information on how we established the parameters for the resist reflow.

Next, the polyimide is dried for 2min@120°C and its surface is treated in O₂ plasma and a 20nm/300nm-thick Ti/Au metalization stack is sputtered³⁸, as shown in Fig.4.12.3. A photoresist film is applied and structured into electrode and pad windows³⁹ and a 2.5μm-thick gold layer is deposited via electroplating onto the windows⁴⁰; the photoresist is stripped in AZ100 for 5min@50°C (see Fig.4.12.4). Another 1.8μm-thick AZ1518 photoresist is spin-coated and structured into electrodes, paths and pads. The resist mask is transferred into the Au film (3-4 min in NaCN) and subsequently in Ti (30 s in BOE). The photoresist is stripped in AZ100. In such way ECoG electrodes and Ti/Au pads are realized (Fig.4.12.5). The heat and O₂ plasma treatment, applied directly before sputtering, should promote high polyimide-metal adhesion.

In the following stage, the organosilane adhesion promoter VM651 is applied and second polyimide film is realized on top of the metallization. A 10μm-thick AZ9260 photoresist is spin-coated and structured into arrays' outlines and cuts. This mask is transferred into polyimide in an O₂+CF₄ RIE plasma, and the photoresist is eventually stripped in AZ100. Another 10μm-thick AZ9260 photoresist is applied, this time structured in electrode and pad windows. These windows are then transferred in polyimide, and the resist is stripped. Hence, the array electrodes and pads are opened and the array outlines/cuts/straps are defined (Fig.4.12.6). We structured the outlines/cuts/straps separately from the opening of electrodes/pads, because of their different thicknesses: 10 μm and 5 μm, respectively.

In the final clean-room fabrication step, a 10μm-thick AZ9260 photoresist is applied on the wafer backside. It is structured into a relatively large window defining the flexible area of the array, and narrow lines surrounding the assembly area. The Si wafer is pre-etched on the backside to a 300 μm depth for 80 min in SF₆+C₄F₈ DRIE plasma, STS ICP tool (Fig.4.12.7). The wafer is unloaded and a blank 4" silicon wafer is fixed on its front side with a silicone paste (WLP 035 from Fischer Elektronik). The blank wafer serves as a mechanical stabilization platform, while the thermal conductive paste provides a heat sink. The MEA wafer is completely etched in ca. 40 min (Fig.4.12.8), the blank wafer is detached and the paste is removed⁴¹. The remaining oxide is wet etched in BOE and the MEA wafer is rinsed and dried for 1h@90°C. Thus, a free-standing flexible electrode array with a monolithically integrated rigid interposer is fabricated. The array can be easily removed from its carrier wafer upon cutting the flexible straps (Fig.4.12.9). Images of the microfabricated ECoG MEAs are presented in Fig.4.13.

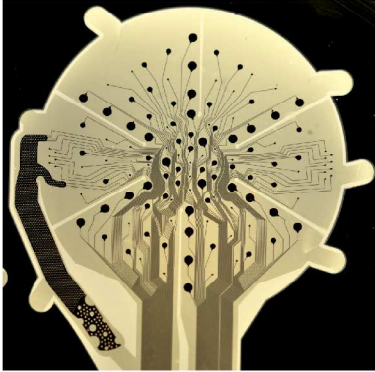
³⁸Ti: 72 s, 200 W; Au: 174 s, 100 W, -45 V bias; Ardenne LA 440S, Ardenne Anlagentechnik, Germany

³⁹O₂ plasma surface activation, 1.8μm-thick AZ1518, AZ726MIF

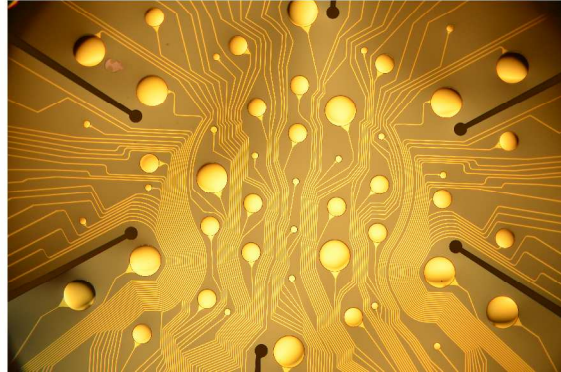
⁴⁰30 min electroplating time; 10 $\frac{mA}{cm^2}$ current density; Cyanide-free gold electrolyte, NB SEMIPLATE AU 100, MicroChemicals

⁴¹Later we exchanged the blank wafer+silicone paste with an electrostatic foil and transferred the second DRIE etch to an Alkatel tool (no pins).

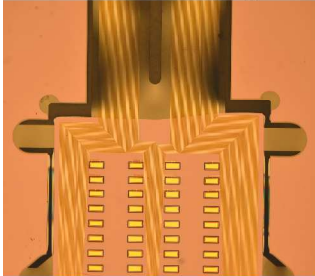
ECoG recording area



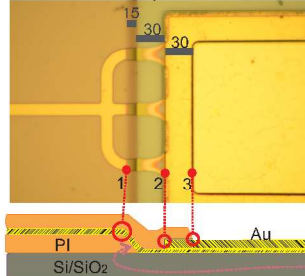
ECoG recording electrodes: 100, 300 & 500 μm



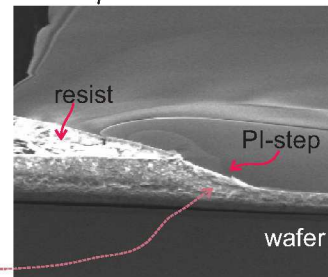
Connector-assembly area



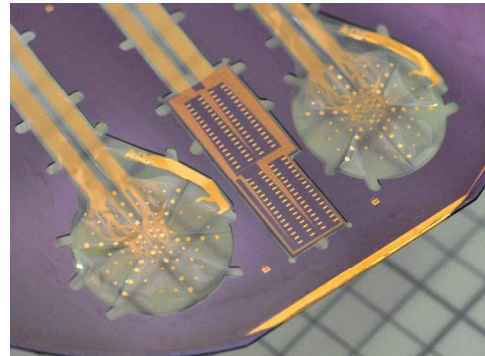
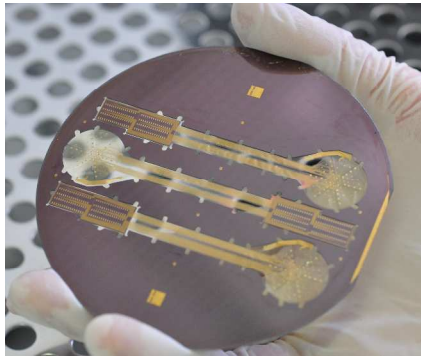
Soldering pad



PI-step



Mother wafer with 3 ECoG MEAs



a completed ECoG MEA



Figure 4.13: Images of flex-rigid ECoG MEAs.

4.5 In-Vitro Characterization of ECoG MEA Electrodes

The recoding electrodes of the MEA were characterized in 0.9% saline via electrochemical impedance spectroscopy (EIS), as shown in Fig.4.14. A 2cm² Pt electrode served as counter electrode (CE) and an Ag/AgCl electrode (Ref) was the external reference⁴² (SensorTechnik Meinsberg GmbH, Germany). A 10 mV sinus was applied at the Pt-electrode, while its frequency was swept from 10⁵ to 1 Hz. The electrode impedances were measured by a portable CompactStat.e impedance analyzer (IVIUM Technologies B.V., NL). The switching between the electrode channels was performed by a LabVIEW-driven NI-PXI 2530 multiplexer.

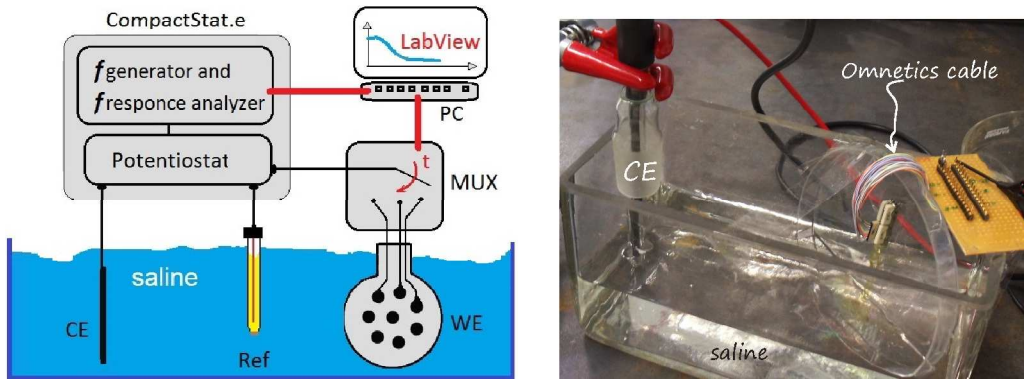


Figure 4.14: In-vitro test set-up: LabVIEW-controlled multiplexer (MUX), counter electrode (CE), external reference (Ref) and ECoG MEA (WE).

Measuring the impedances of the MEA electrodes immersed in salt water (saline) against a Pt-electrode revealed different impedance spectral bands for each electrode size (recoding electrodes of 100, 300 and 500 μm diameter and a 2.5 mm² MEA's own reference), as shown in Fig.4.15. The impedance magnitudes scaled inversely with the electrode size, in accord with theory. At frequencies above 10 kHz all impedance spectra have dominant resistive behavior i.e. the impedance magnitudes $|Z|$ are frequency independent. Below 10 kHz all $|Z|$ rise with decreasing frequency. At 100 Hz, a frequency related to the gamma ECoG activity, the average $|Z|$ values (mean \pm SD) are $405.5 \pm 31.3 \text{ k}\Omega$ for 100 μm , $41.1 \pm 2.8 \text{ k}\Omega$ for 300 μm and $14.5 \pm 0.3 \text{ k}\Omega$ for the 500 μm -diameter electrodes, and 1.7 k Ω for the MEA's own reference electrode.

The above impedance magnitudes obtained at 100 Hz are plotted in Fig.4.16 as a function of the electrode surface area. The 100 μm , 300 μm and 500 μm -diameter electrodes have 0.031, 0.283 and 0.785 mm² surface areas and the 100 Hz impedance magnitude increases linearly with the inverse of the electrode area.

⁴²At first we used an Ag/AgCl reference electrode, but dropped it later, as two-point measurements provided comparable results due the relatively large area of the ECoG electrodes.

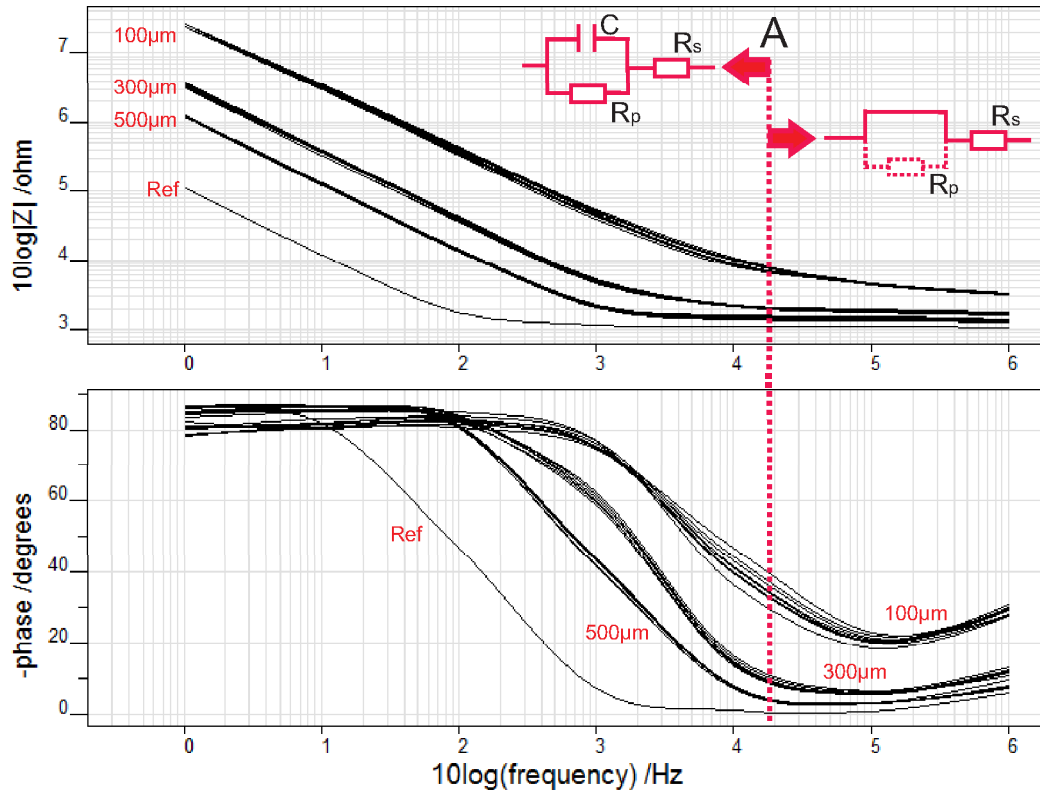


Figure 4.15: Impedances of 100, 300 and 500 μm -type electrodes and the MEA reference.

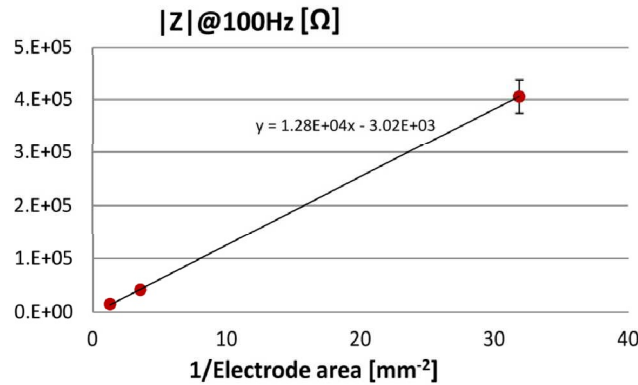


Figure 4.16: $|Z|@100\text{Hz}$ derived from the data of Fig.4.15, plotted against the inverse values of the electrode area (mean \pm SD); the 100 μm -diameter electrodes have highest $|Z|$.

Additionally, the 100Hz-impedance magnitude of the MEA's own reference electrode is eight times smaller than the impedance magnitude of the largest circular electrodes (500 μm -type).

When a metal electrode is immersed in an electrolyte (e.g. salt water) its electrical behaviour can be approximated by an electric circuit $X_c || R_p + R_s$, with X_c being a capacitive reactance

Table 1. Parameters of the electric circuit model (mean + s.e.m): C is the double-layer capacitance, R_p the charge transfer resistance and R_s the path + saline resistance.

Electrode Diameter	Electrode Area [mm ²]	R_s [k Ω]	R_p [M Ω]	C [nF]
100 μm	0.031	2.6 ± 0.1	83.5 ± 31.7	1.3 ± 0.1
300 μm	0.283	1.8 ± 0.02	4.8 ± 0.4	10.6 ± 0.4
500 μm	0.785	1.5 ± 0.02	1.3 ± 0.1	36.0 ± 3.1

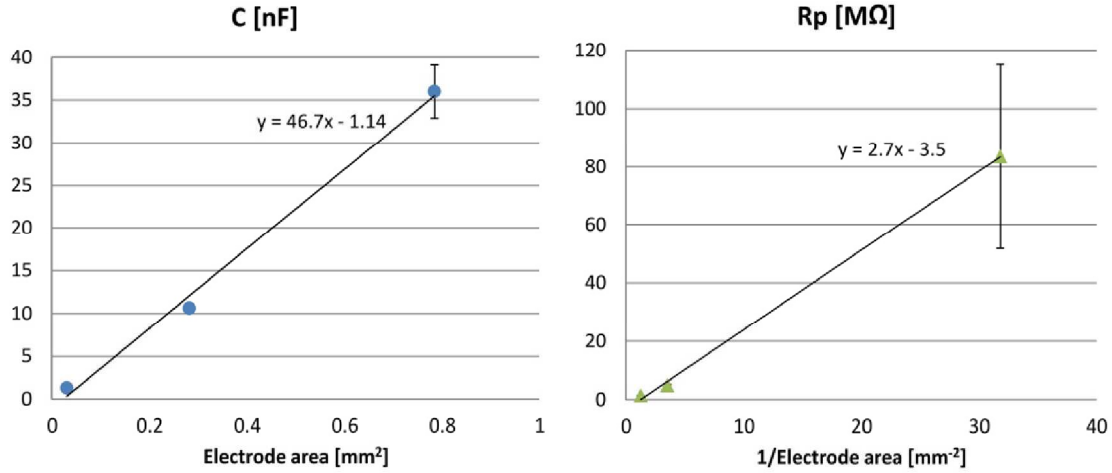


Figure 4.17: C and R_p values from Table 1 plotted against the electrode area.

and R_p and R_s ohmic resistances (see left circuit in Fig.4.15 and also Section 3.5). As the metal electrode is negatively charged with respect to electrolyte solution, a double layer is formed at the electrode-electrolyte interface, which resembles a charged capacitor. Its capacitance C is related to X_c by the angular frequency ω , with $C = (\omega X_c)^{-1}$. Additionally, as current passes via the electrode-electrolyte interface, the resistance R_p accounts for the associated charge transfer, whereas R_s sums up the electrolyte and array path resistances [87].

Applying the above electric circuit model to the impedance data (whole frequency spectrum) reveals that at frequencies above 10 kHz the electrical circuit reduces to R_s because C shunts R_p (see right circuit in Fig.4.15); below 10 kHz both C and R_p determine the steady impedance increase (see left circuit in Fig.4.15). The impedance data of the ECoG array were fitted using IviumSoft Electrochemistry Software (Ivium Technologies B.V., The Netherlands) to derive the values for C , R_p and R_s (mean + s.e.m.) – R_s belongs to the low k Ω -range; R_p spans the 1-80 M Ω -range and rises exponentially with decreasing electrode diameter, orders of magnitude higher than R_s ; C is in the 1-36 nF-range and linearly increases with electrode area (see Table 1 and Fig.4.17).

4.6 In-Vivo Characterization of ECoG MEA

The results summarized in this Section were obtained by Victor Gordillo-Gonzalez as part of his PhD Thesis under Prof. Dr. Kreiter at Institute for Brain Research, University of Bremen.

The ECoG MEA⁴³ was implanted epidurally over V1 of a rhesus monkey. The MEA was characterized in vivo while the monkey performed a specific visual fixation task. Fig.4.18 shows the stimulus sequence, which the animal perceived: 1). onset of the fixation point at the center of the screen (blank period, ca. 300ms), 2). a light bar moved laterally across the lower right part of the visual field (3000ms), 3). fixation point for 250-1250ms, 4). the brightness of the fixation point was changed. 5). The moving bar was presented for mapping the receptive fields. If the animal responded successfully to this brightness change, it received a reward.

The recorded ECoG signals from successful trials were amplified 10 times by 4x 32-channel headstage pre-amplifiers (MPA32I, Multichannel Systems MCS GmbH, Reutlingen, Germany) and then 100 times by programmable gain amplifiers (PGA64, Multichannel Systems MCS GmbH, Germany). The recorded signals were digitized at 25 kHz sample rate. A recording session was evaluated only if every single stimulus was recognized at least ten times.

The recorded data was filtered between 1-150 Hz and down-sampled to 1 kHz by applying Matlab-designed filters. To enable analysis in the time-frequency domain of the recorded ECoG signals, a wavelet transformation was applied. Thereby Victor Gordillo-Gonzalez used complex Morlet wavelets with Gaussian shape in both time and frequency domains [23]. Power spectral density values (PSD) were calculated as the square of the absolute value of the wavelet-transformation divided by the Nyquist frequency (500 Hz). Time-frequency plots of mean power spectral density were built, corresponding time-frequency bins of trials sharing the same stimulus were averaged and then normalized against the baseline taken from the initial fixation period of 300 ms before mapping stimulus onset.

Neuronal ECoG signals were recorded by the here proposed MEA, six weeks after MEA implantation, while a light bar swept across the visual field (see Fig.4.19). The presented signals come from 14 ECoG electrodes spanning the array diameter (1-14, Fig.4.19, right image).

The ECoG signals from three size-different electrodes situated close to each other were further evaluated. Fig.4.20 shows time-frequency plots of normalized power spectral density (PSD), normalized to baseline activity. Increase in electrode size resulted in higher spectral power density. The PSD was up to 10 times stronger than the baseline, while the 40-150Hz frequency range was most prominent

In order to further compare the performance of the size-different electrodes, their PDS-powers of the 40-150 Hz frequency range γ PSD were plotted against each other. Thereby, the ECoG

⁴³which was fabricated at IMSAS, University of Bremen

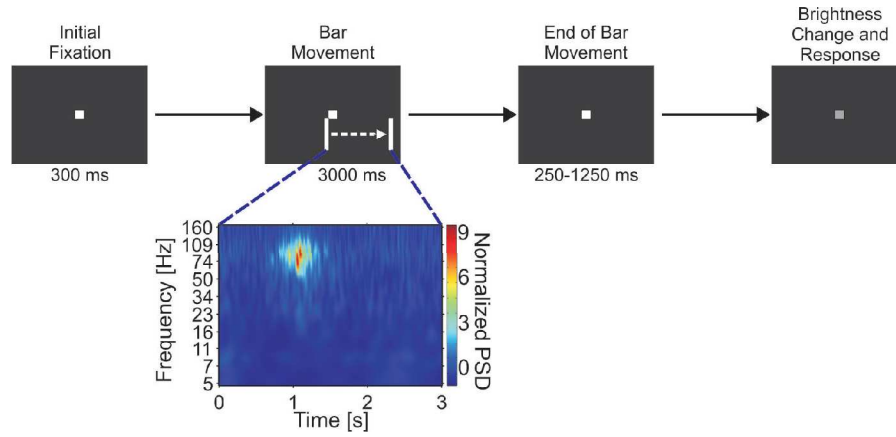


Figure 4.18: Receptive field mapping task. Movement of the bar stimulus over the receptive field of an electrode is reflected as a temporary increase in ECoG signal power.

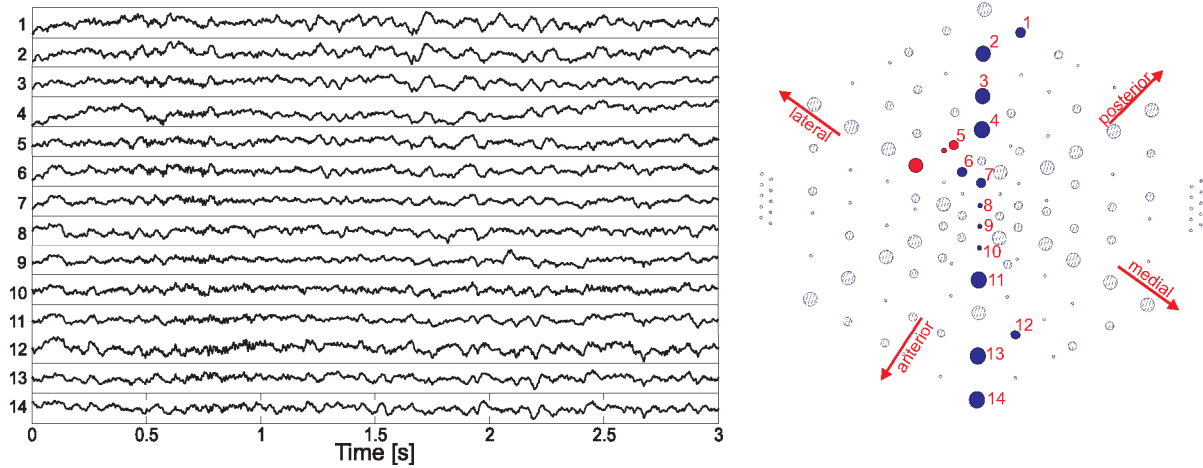


Figure 4.19: Electrophysiological signals (left image) recorded from electrode sites distributed over the array diameter (right image, 1-14).

signals of 11 triplets (100, 300 and 500 μ m in diameter) were averaged over eight recording sessions. These recordings were referenced in two ways: once using skull-facing electrode and secondly using common average reference. Fig.4.21 presents the better performance of the MEA's reference electrode (skull-facing).

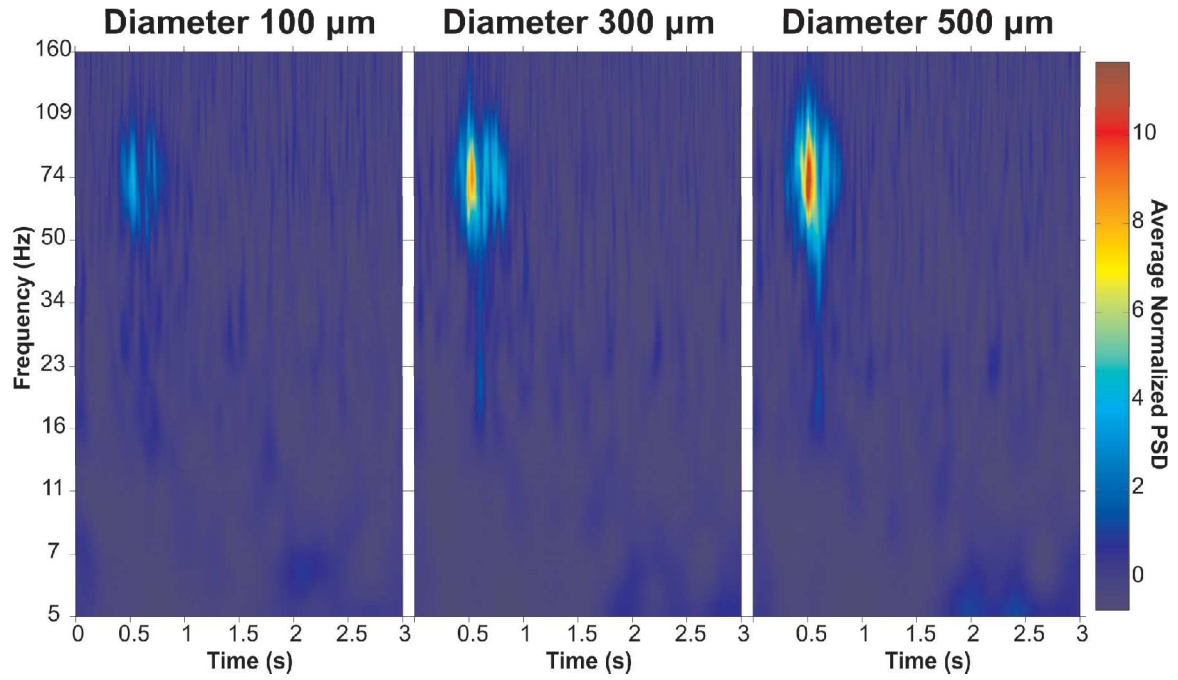


Figure 4.20: Time-frequency plots of normalized PSD for three neighbouring electrodes of different sizes situated in the middle of the array layout (red circles in the right image of Fig.4.19).

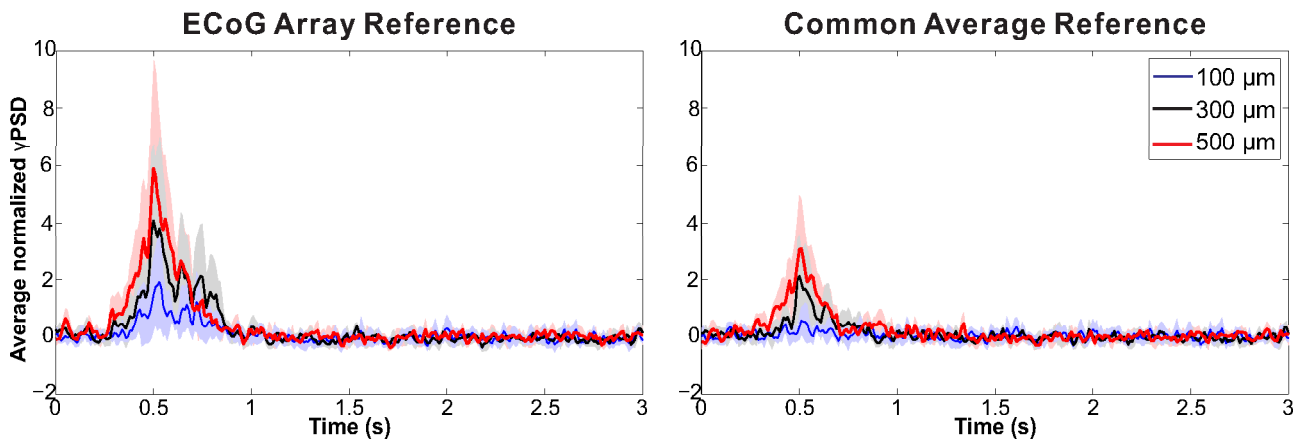


Figure 4.21: Time course of normalized gamma-PSD \pm s.d. derived from time-frequency plots (shown in Fig.4.20), using a skull-facing reference electrode (Left) and common average referencing (Right).

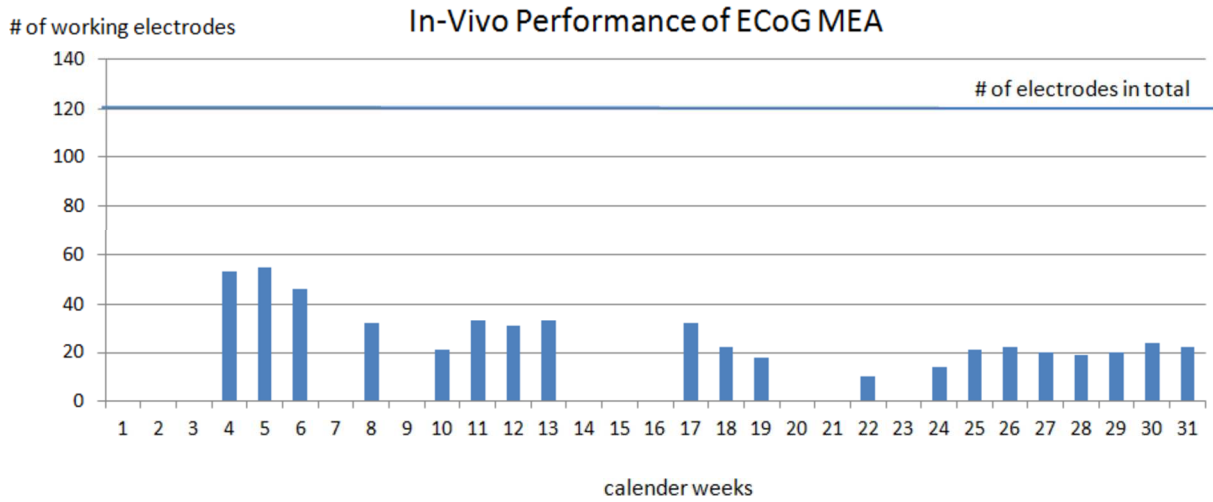


Figure 4.22: Number of working MEA electrodes over time.

Further, the in-vivo performance of the ECoG MEA was monitored for several months. Fig.4.22 shows the number of working electrodes of the MEA in the course of calendar weeks. First natural electrophysiological signals were recorded 4 weeks⁴⁴ after implantation of the MEA. Only 42 % of all electrodes (53 from 124 recording channels⁴⁵) were able to provide natural electrophysiological signals. After ca. 4.5 months, this number decreased to ca. 24%, and to 16% after 7.5 months. During this gradual decrease, the number of working electrodes fluctuated over time. Additionally, after ca. 3.5 months⁴⁶ first signs of parasitic behaviour within a group of electrodes⁴⁷ was noticed; in the course of time the number of disfunctional electrodes increased steadily; nonetheless within the span of ca. 1.5 years a small number of electrodes succeeded to record signals without any signs of parasitic influence.

The initial loss of 59% of electrodes was most probably due to mechanical handling (unplugging of the Omnetics connectors⁴⁸) and sterilization, as these were the only two processes which took place before MEA implantation. The fluctuation of working channels over time can be explained by unstable electrical contact between MEA and Omnetics connectors, once present and another time lost.

The gradual decrease of working channels within the 7.5 months was attributed to three basic failure modes: (A) the receptive fields of the electrodes decreased in power density, (B)

⁴⁴This recoding onset was chosen in order to wait for complete healing of the implantation wounds.

⁴⁵The MEA has 124 recording channels and a reference electrode. All these electrodes are electrically linked to 4×32 connectors, whereas each connector receives its own electrical path to the reference electrode.

⁴⁶time counting starts directly after device implantation

⁴⁷electrodes 1-3, 5-6, 8, 10, 12 and 14 in connector A

⁴⁸The force to unplug an Omnetics connector is much higher as compared to conventional connectors.

the appearance of the receptive fields became too similar within the affected electrodes, almost as if they were all the same channel, resembling the formation of a parasitic short-circuit⁴⁹, and (C) the RF was completely lost, corresponding to an open channel.

From the above observations, two basic issues crystallize: loss of electrical contact and formation of short-circuits. To note is that these *in-vivo* results were obtained with the ECoG MEA, fabricated according to the scheme of Fig.4.10.A, i.e. with inherited unstable electrical contacts. We improved the design of the MEA with respect to electrical contact stability (see Fig.4.10.C, which was implemented for MEA fabrication in Chapter 6). Further, we assumed that the parasitic behaviour can be explained by formation of short-circuit connections⁵⁰ between the electrodes (also between non-neighbours) upon water penetration into the thin-film insulation (polyimide). Salt water was considered as a most probable trigger, because it is present in abundance between cortex and skull.

4.7 Summary

A flex-rigid ECoG electrode array was fabricated with rigid connector platform (Si/SiO₂) for the assembly of Omnetics connectors. The MEA device was characterized *in vitro* and *in vivo*.

Electrical open- and short-connection tests showed that rigid solder joints situated on Si/SiO₂ were much more reliable than those situated on PI. Adhesion tests revealed higher adhesion strength of the Si/SiO₂-metal interface compared to the Si/SiO₂/PI-metal interface. Comparing PI/metal adhesion before and after the second polyimide curing indicated a decrease in adhesion at the PI/metal interface, most likely caused by thermal stress exerted during the curing of the second PI layer.

The array electrodes and its reference have impedance magnitudes that increase with decreasing electrode surface area. The impedance magnitude of the reference electrode at 100 Hz is eight times smaller than the impedance of the largest circular electrodes, and the impedance at 100 Hz of the smallest electrodes is ca. 10⁵ times lower than the input impedance of a commercial headstage amplifier [51]. These impedance differences are of considerable importance for recording ECoG signals with sufficiently high amplitude. Furthermore, the derived parameters of the equivalent electric circuit as suggested by [87] indicated a clear linear relationship between the capacitance and the electrode surface area, while the associated double-layer re-

⁴⁹Coincidentally enough, similar parasitic behaviour was observed in another ECoG-MEA, which had been fabricated by Prof. Stieglitz's research group and had been also *in-vivo* tested in Prof. Kreiter's lab. The Stieglitz's array was made from the same sort of thin-film isolation (BPDA-PPD polyimide), but contained Pt-metallization instead of Au.

⁵⁰in this case high-ohmic parasitic current paths

sistance rose linearly with the inverse of the electrode surface area. Compared to impedance values reported in literature, our measurements are equivalent to impedance values reported by Baek et al. (480 μm diameter) [53] and by Kim et al. (250 μm diameter) [55].

Epidural electrocorticographic recordings of strong and distinct stimulus-induced electrophysiological field potential signals from a Rhesus macaque's primary visual cortex (V1) demonstrated functioning of the proposed flex-rigid MEA design. Larger electrodes recorded signals with greater spectral power in the gamma band (40-150 Hz), which can be attributed to the larger recorded population of neurons contributing to the stimulus-induced activity patterns. The use of a skull-facing reference electrode confirmed an expected higher spectral power as compared to the common average reference technique, distinctively stronger than the baseline.

Furthermore, referencing the recordings to the skull-facing electrode provided signals with greater power than those obtained using a common average referencing technique. This difference can be explained by the synchronous activity in the gamma band induced over extended regions of area V1 by the long bar stimulus [88]. This activity is therefore acquired by a substantial subset of the array electrodes and therefore prominently contained in the common average reference which is obtained by averaging over all electrode signals. Subtracting this common average reduces the gamma band response in corresponding electrodes.

These results support the advantage of engineering a flex-rigid electrode array with a monolithically integrated connector platform for the microfabrication of high-electrode count and density ECoG electrode arrays for neuroprosthetics and brain-computer interfacing applications.

Chapter 5

Long-Term Stability of BPDA-PPD Polyimide in Saline

”Nothing is softer or more flexible than water, yet nothing can resist it.”

Lao Tzu

In the past decade highly flexible biomedical devices were engineered, which enabled novel methods of signal acquisition from within the human body. In this regard, cortical ECoG MEAs have recently emerged. Being thinner than a human hair, they can easily slip between cortex and skull, and acquire electrical activity of neuronal populations directly from the cortical surface¹ [89]. These ECoG recordings offer detailed information about cognitive behaviour with high speed and accuracy, which makes ECoG MEAs attractive as weakly-invasive high-performance signal-acquisition platforms for future BCIs and neuroprosthetic applications [4].

Nevertheless, as the thickness of ECoG-MEAs is restricted up to 1 mm due to the site of their application, established packaging methods for marketed long-life medical devices, such as heart-pace makers or cochlear implants, are not applicable. Polymeric materials, such as polyimide and parylene C, serve as thin-film insulation in most ECoG microdevices, but polymers lack hermetic properties. Concurrently, ECoG devices will mature toward real-world neuroprosthetic applications only if their long-term stability is guaranteed *in-vivo* for at least 10 years.

In the previous chapter the *in-vivo* performance of ECoG-MEA revealed the formation of parasitic short-circuits between electrodes. Saline was considered as most probable trigger for these parasitics, as it is the natural medium in vivo and can readily diffuse into the polyimide coating and thus provide a leakage path. To investigate how salt water diffuses into

¹contrary to intracortical electrodes e.g. Utah- or Michigan-type

the thin-film isolation of our electrode array, we considered two basic mechanisms: **volume diffusion** of saline through the thin-film isolation and **interfacial diffusion** of saline along the metal-isolation paths. To test the effect of volume diffusion on the electrode performance, interdigitated (IDE) finger structures were considered as most appropriate test method. With fine inter-finger spacing, such test structures can sense tiny amounts of moisture absorbed by the thin-film isolation on top, therefore used extensively for humidity sensor applications.

This Chapter summarizes the materials/methods applied to investigate how both diffusion mechanisms influence the formation of parasitic inter-electrode connections under accelerated soak-test conditions (saline@60°C). The obtained results reveal to what extent each mechanism contributes to this parasitic behaviour and based on the latter possible solutions to prolong the life-time of future ECoG-MEAs are suggested.

5.1 State of the Art

This Section reports on recent research accomplishments on: (1) *in-vivo* long-term stability of implantable passive microdevices with focus on ECoG and intracortical devices, and (2) long-term performance of thin-film encapsulation materials (polyimides and parylene C) examined in saline under accelerated soak conditions. This literature survey was conducted to provide a series of promising state-of-the-art material candidates² to be tested at first in saline at accelerated conditions (volume diffusion) and thus pave the road toward longer-stable ECoG MEAs.

Long-term stability of cortical microdevices *in-vivo* Initially, our decision to use U-Varnish-S polyimide as a thin-film encapsulation/electrical isolation for our ECoG was based on the fact that polyimides in general possess exceptional mechanical/thermal/electrical properties and can be casted in form of highly flexible thin-films. Our choice to use exactly U-Varnish-S polyimide was influenced by the work of Rubehn et al. 2009 [51], who applied the same polyimide type to fabricate for the first time large-area ECoG electrode arrays, one of which was *in-vivo* tested by Prof. Kreiter's group. Within the above contribution [51] Rubehn reported on a 4.5 month-long *in-vivo* functionality of a 252-channel polyimide-based ECoG array without any noticeable device malfunctions.

Two other research groups also made use of polyimide in the fabrication of their ECoG MEAs. Yeager et al. 2008 [90] used Kapton© as flexible material in a 64-channel ECoG electrode array (Kapton/TiW/Au/SU-8), and reported on 108-day-long successful signal acquisition *in-vivo*; thereby TiW accounted for a good adhesion between the Kapton film and

²BPDA-PPD polyimide to be used as a reference

the Au-metallization, even better than Kapton/Au or Kapton/Ti/Au, and thus accounted for the prolonged device performance. Kapton® also served as a flexible substrate and inter-layer isolation film within the 360-channel ECoG active device of Prof. Roger’s group [47]³, which contained monolithically-integrated nano-membrane transistors and its performance was tested *in-vivo*. While this novel microfabrication technology offers ECoG measurements of exceptionally high spatial resolution, this work did not report on the long-term performance *in-vivo*.

Instead of polyimide, several ECoG electrode arrays were fabricated out of Parylene C. Among these, only Ledochowitch et. al 2013 [52] reported on the *in-vivo* performance; he could successfully record electrophysiological signals with a 64-channel parylene/Pt/Au/Pt/parylene MEA from a rat cortex within a time span of 370 days; thereby only a slight increase of the impedance magnitude was observed without any indication for the formation of parasitic inter-electrode shorts; from the latter he deduced that this was an indication for the absence of delamination along the parylene-metal interface of the electrode paths⁴.

Beyond ECoG MEAs, the long-term performance of intracortical microelectrode arrays⁵ has been extensively investigated, as this technology was introduced much earlier⁶ than ECoG-MEAs because it enabled for the first time multi-channel recordings of electrophysiological signals from single neurons. The Utah needle array, most prominent among the intracortical MEAs, and the only one FDA-approved, has undergone a tremendous development in the course of time: the *in-vivo* performance of the first successful Utah-array, casted out of Si and implanted in a cat cortex, was reported to be 13 months [91]; a more recent Utah-array generation of 100-channels, which relies on a parylene C encapsulation, successfully performed for 1000 days (= 2.7 years) in patients [92]. However, intracortical MEAs are tissue-penetrating electrodes and can induce neuronal damage upon implantation, which triggers the formation of glial sheet around the electrodes, thus shunting it from the brain in the course of time, and therefore reducing the signal quality over time. This is not the case with ECoG devices – as they rest on the cortex surface – which raises the hope that ECoG MEAs have the potential, in this regard, to perform for much longer time *in-vivo*.

In Summary, ECoG signal-acquisition is a relatively recent recording technique, as compared to intracortical measurements, which explains the little amount of contributions reporting on the *in-vivo* long-term performance of ECoG-MEAs: a Kapton/TiW/Au/SU-8 ECoG array performed successfully for 108 days [90], and an U-Varnish/Pt/U-Varnish array lasted for 4,5 months (=ca. 135 days) [51]. In comparison, our U-Varnish/Au/U-Varnish array survived

³as described in the supplementary material of [47]

⁴10 μ m inter-path distance (and pitch)

⁵best known as micro-needles or intracortical MEAs

⁶driven extensively by neurophysiologists

90-120 days *in-vivo*. Alternatively, Parylene-C-encapsulated ECoG arrays lasted for 370 days, while Utah-needles survived 1000 days. All these studies suggest Parylene C to be better packaging material than polyimide and that delamination at the polymer-metal interface can trigger most probably the formation of parasitic shorts in both Parylene-C [52] and polyimide-encapsulated MEAs [90].

Long-term stability of Parylene and Polyimide in saline Accelerated aging tests are highly useful methods to test the long-term performance of encapsulation materials *in vitro*. Usually, a thin-film coated metal plate is partially inserted in a salt water container and kept at elevated temperatures to increase the rate of moisture diffusion into the film; as water diffuses into the film, e.g. via defects or pin holes, the film resistance decreases, which is monitored by means of external electrodes. Alternatively, instead of a metal plate, interdigitated (IDS) capacitive structures come into use; with a pitch within the $10\mu\text{m}$ range these IDS structures can sense even smaller amounts of water molecules absorbed within the thin-film coating, which not only makes this method much more sensitive (volume diffusion), but also resembles the case when water diffuses into the cable of our ECoG MEA. Based on the results gained in an accelerated soak test, predictions about the lifetime of these materials when used *in-vivo* can be made. Nevertheless, *in-vitro* tests alone are not sufficient, as within a biological environment interfacial diffusion can play an important role for the degradation of the overall device, e.g. as water enters the device via electrode openings and diffuses along metal-polymer interfaces.

Parylene C (poly-chloro-p-xylylene) is used as protective coating in numerous biomedical applications [93], due to its hydrophobicity, conformality⁷ and biocompatibility⁸. However, it adheres poorly to other materials [96], which can lead to device malfunction. For example, as saline diffuses along parylene-metal-parylene interfaces, this can cause parasitic short-circuits between adjacent electrodes.

Several methods to promote adhesion of Parylene C to other materials have been proposed. Substrate pre-treatments [96]: 1) oxygen plasma to remove substrate surface contaminations or argon plasma to roughen substrate surface, 2) PECVD deposition of thin-film adhesion promoters, based on methane or trimethylsilane, 3) silanization of the substrate surface in gas or liquid form. Additionally, heat-treatment of already-deposited Parylene C film was reported to improve adhesion [97], [98]: 1) annealing at 200°C and 300°C in N_2 atmosphere, 2) the higher the temperature and duration, the better the adhesion, 3) temperatures higher than 350°C destroy adhesion. As interdigitated microstructures (IDE) are highly sensitive to the diffusion of water molecules through the coating on top, they are mainly used for *in vitro* tests

⁷e.g. parylene C can penetrate into a channel up to a depth = 5x channel's diameter [94]

⁸Parylene C has USPClassVI biocompatibility certificate (highest) [95]

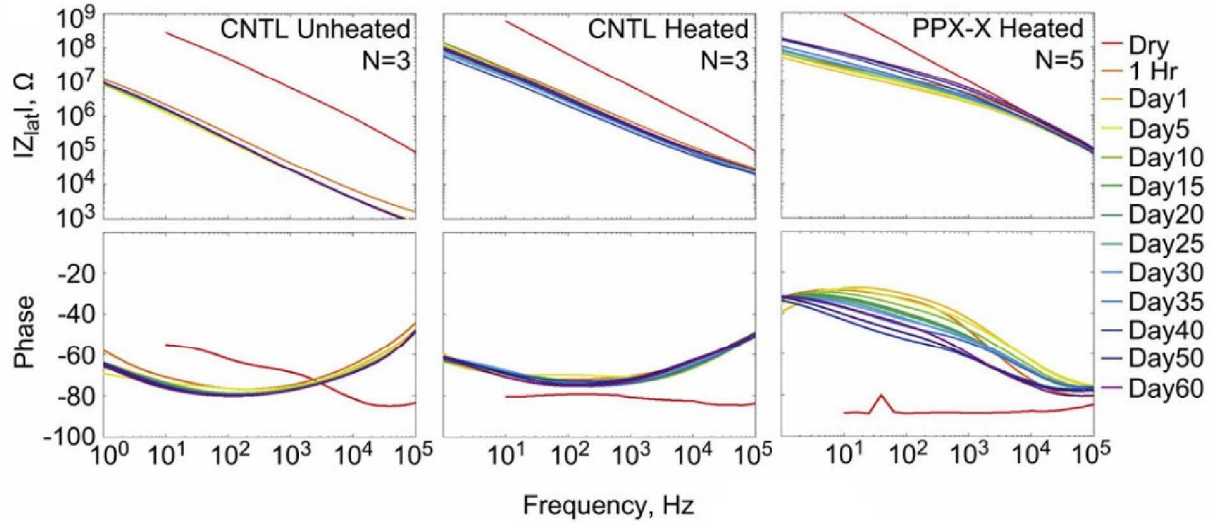


Figure 5.2: Accelerated soak tests on IDE sensors coated with parylene C (CNTL), heated parylene C and modified parylene (PPX-X), adapted from [95].

of parylene coatings.

Seaymour et al. 2009 [95] investigated the in vitro performance of parylene-metal-parylene IDE samples. Both parylene surfaces were functionalized with two complimentary reactive groups and upon heating for 3h@140°C both reactive groups formed strong covalent bonds. This adhesion method guaranteed a relatively high IDE impedance for 60 days in saline@37°C. The reactive parylene Seymour used was poly-p-xylylene (PPX) functionalized with two reactive groups: aldehyde (CHO) and aminomethyl (CH₂NH₂). Upon heating for 3h@140°C both reactive groups form strong covalent bonds, as illustrated in Fig.5.1, which improves the wet adhesion of the parylene layers.

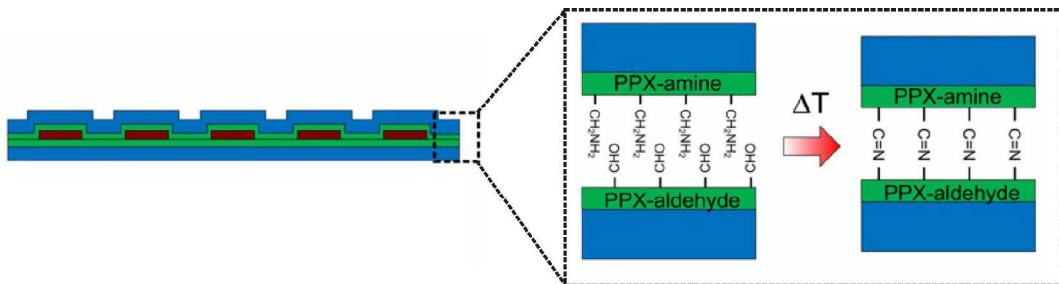


Figure 5.1: Improving the adhesion of a parylene-metal-parylene microdevice by functionalizing the adjacent parylene surfaces with complimentary reactive groups, adapted from [95].

To investigate how the improved adhesion affects the soak performance of the overall device, Seaymour et al. performed accelerated soak tests for 60 days on metal IDE structures encapsu-

lated in: (1) parylene C⁹, (2) heat-treated parylene C for 3h@140°C and (3) modified parylene (PPX-X¹⁰). The soak tests revealed, as shown in Fig.5.2, that modified parylene maintained a relatively high impedance, much higher than that of parylene C: @10kHz 800% > parylene C and @1kHz 70% > parylene C. These results confirm the crucial role interfacial adhesion plays in the long-term performance of implantable microsensors.

Further, the encapsulation performance of parylene C was also investigated by Hassler et al. 2010 [99], whereas a series of adhesion promoters were applied between a parylene film and several substrates. Adhesion peel tests and IDE-soak tests revealed Silane A-174 to be appropriate adhesion promoter for parylene-parylene, parylene-Si₃N₄ and parylene-Pt interfaces. The soak tests were performed in saline at 37°C with 3V applied across the IDE structures. The magnitude of the IDE impedance remained high for max. 11 days.

The influence of substrate material on the measurement of parylene impedance was investigated by Xie et al. 2011 [100]. IDE structures of 130μm-pitch were fabricated on three different substrates – Si/Si₃N₄, Si/SiO₂/Si₃N₄ and quartz – and coated by a thin film of Parylene C. The overall impedance of the IDE-samples was monitored at 37°C in PBS¹¹ for 180 days, which disclosed Si/Si₃N₄ and Si/SiO₂/Si₃N₄ as "leakage" substrates, and quartz as most suitable one¹².

Polyimide was introduced into the market under the trademark "Kapton© film" in 1960s [101]. This material had high temperature stability, outstanding mechanical properties and low dielectric constant¹³, which matched the goal of the electronic industry at that time toward ever faster computers [101]. The relatively low dielectric constant of Kapton© accounted for a decrease in signal delays as electrical signals traveled from one chip to another via their packages and interacted on the way with the dielectric mediums [101]. Recently, as flexible thin-film biosensors emerged, Kapton© could not meet the requirements for long-term stability in biological environment because of its relatively high moisture absorption (0.4-1.3 % at 23°C, 50 % RH¹⁴), and became overshadowed by Parylene C with moisture absorption < 0.1 % acc.[103].

Beside Kapton©, a wide spectrum of polyimides emerged based on the phenomenon that a slight modification of the polyimide backbone highly altered its physical properties. For example, a BPDA-PPD polyimide was recently developed by both DuPont and UBE under the trademarks PI2611 [104] and U-Varnish-S [105], respectively, with lowest intrinsic stress and lowest moisture uptake among all polyimides. For PI2611 the moisture absorption is reported

⁹denoted by Seymour et al. as "CNTL"

¹⁰X denotes product of the complimentary reactive groups as shown in Fig.5.1

¹¹phosphate buffered saline i.e. a water-based solution

¹²Total magnitude impedance at 1 kHz: 80 kΩ for Si/Si₃N₄, 0.2 MΩ for Si/SiO₂/Si₃N₄ and 2 MΩ for quartz.

¹³3.4 measured at 1 kHz, 23°C [102]

¹⁴RH stands for relative humidity

to be 0.5 % [104], while for U-Varnish-S it is 1.2 % acc. [105] or 0.8-1.4 % acc. [99].

Stieglitz's research group investigated the long-term stability of BPDA-PPD polyimide [106] in a simulated biological environment (PBS¹⁵). For this investigation three different BPDA-PPD foils were used: PI2611 [104], U-Varnish-S [105] and Upilex25S [107]; the first two types were obtained as fluid precursors, then spin-coated on Si wafers at 2000rpm and cured at 60min ramp-up & 60min@350°C and 170min ramp-up & 10min@450°C, respectively (5µm-final thickness). The third polyimide was obtained as a ready-made 25µm-thick foil. All foil types were stored in PBS for 20 months at three different temperatures – 37°C, 60°C and 85°C – to investigate how these ambients affect the mechanical properties of BPDA-PPD polyimide in the course of time. Tensile tests, performed on a monthly basis, showed no degradation in the mechanical properties – stress at break, strain at break, stress at 10% strain and fracture energy – when stored at 37°C and 60°C except for an increase in Young's modulus values for PI2611 and U-Varnish-S. In contrast, Kapton degrades after 30 days in DI water@25°C, which suggests that the mechanical performance of Kapton "might not be representative for the whole group of polyimides" [106]. Additionally, 85°C storage condition was not recommended to be used for accelerated soak tests on biomedical implantable devices, because mechanical degradation of BPDA-PPD polyimide at this temperature does not obey the Arrhenius equation. Further, Schubert et al. 2015 investigated the water-barrier of PI 2611 by IDE structures. When soaked in saline, this polyimide maintained high impedance values for 30 days [108]. Further, Kirsten et al. 2014, investigated the water-vapour transmission rate (WVTR) via 9 µm-thick PI 2611 membranes (ca. 6 g/(m²d)) [109].

An intriguing work on the applicability of polyimide as non-hermetic packaging material for 3D-interconnects was presented by Sugitani et al. [110], [111]. He investigated the moisture resistance of gold interconnects, using either polyimide¹⁶ or BCB¹⁷ as thin-film insulation. As gold is the main material used in interconnects, and it adheres very poorly to organic insulators, different thin-films were applied between the gold and the insulation: W, WN, WSi and WSiN. The test samples, with cross section shown in Fig.5.3, were exposed to 85°C, 85% RH under two electrical test conditions: (1) contact-resistance evaluation with current density of $1.3 \cdot 10^3$ A/cm², and (2) inter-line leakage test with 10 V applied bias. Right image of Fig.5.3 illustrates the results obtained from contact-resistance tests: (1) WSi/Au interconnects without any passivation failed first¹⁸, (2) WSi/Au and WSiN/Au interconnects with additional polyimide passivation degraded next, (3) WN/Au and W/Au interconnects with polyimide

¹⁵Phosphate-buffered saline, P3813 from Sigma-Aldrich, 0.138M NaCl & 0.0027M KCl, pH = 7.4 [106]

¹⁶polyimide was spin-coated and cured for 60min@300°C, 2.5µm final thickness

¹⁷benzocyclobutene, spin-coated and cured for 40min@250°C, 2.5µm final thickness

¹⁸failure if resistance increase >20%

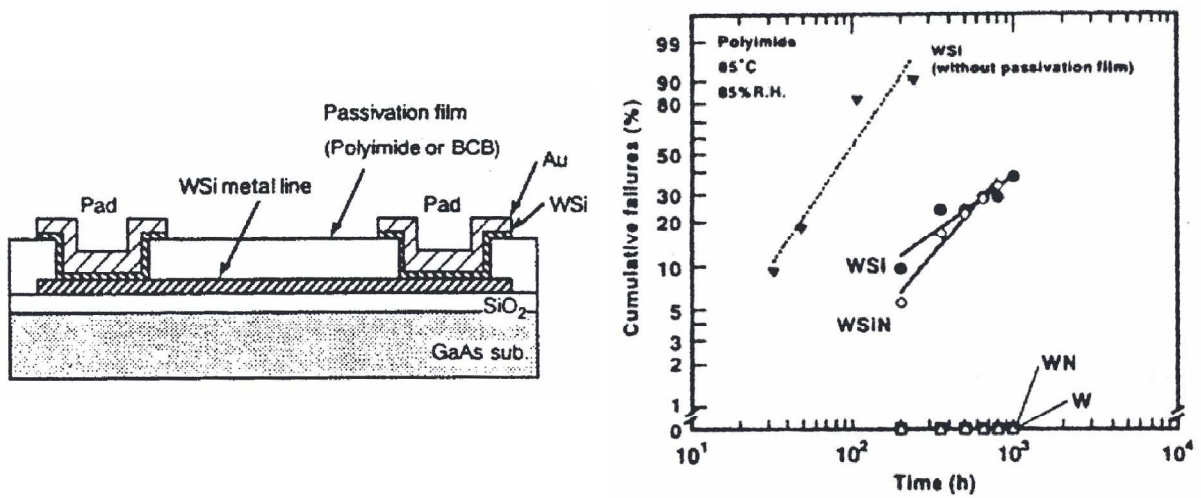


Figure 5.3: (Left) Cross-section of gold interconnects used as test samples, adapted from [110]; (Right) Influence of the adhesion metal (WSi, WSiN, W and WN) on the performance of gold interconnects when exposed to moisture, adapted from [110].

passivation were not affected at all, even after 1000h operation (= ca. 42 days). The reason for the early failure observed in non-passivated samples is explained as follows: "the end face" of the WSi metal film is attacked by moisture, which triggers oxidation reactions; as WSi is oxidized, it expands in volume, cracks occur and "the insulator film separates" from the polyimide [110]. This reveals the importance of interfacial adhesion i.e. between polyimide-passivation and gold-interconnects for the long-term performance of the overall device under accelerated moisture aging.

Fig.5.4 presents the results from the 10V inter-line leakage test, wherein the performance of BCB and polyimide-passivated W/Au interconnects was investigated: (left image) in BCB-coated samples an increase in leakage current¹⁹ occurred at first at 96h and then in all samples after 716h; (right image) in polyimide-coated samples no increase in leakage current was observed even after 1000h. This finding is very intriguing, because in general polyimide is known to absorb much more moisture than BCB. Nevertheless, in the work of Sugitani et al. polyimide proved as a much better moisture-resistant passivation, which suggests that "permeability is more important than moisture absorption" [111].

In Summary, the long-term performance of thin-film packaging materials was investigated in salt water at elevated temperatures. The insulation property of parylene C films was monitored by means of IDE structures at 37°C by several research groups, whereas the longevity of the overall device was prolonged by: adhesion optimization (by heat or chemically) at the parylene-parylene interface [95]; Silane A-174 adhesion promoter for parylene-parylene, -Si₃N₄ and -Pt

¹⁹failure if leakage current > 1 · 10⁻⁹ A

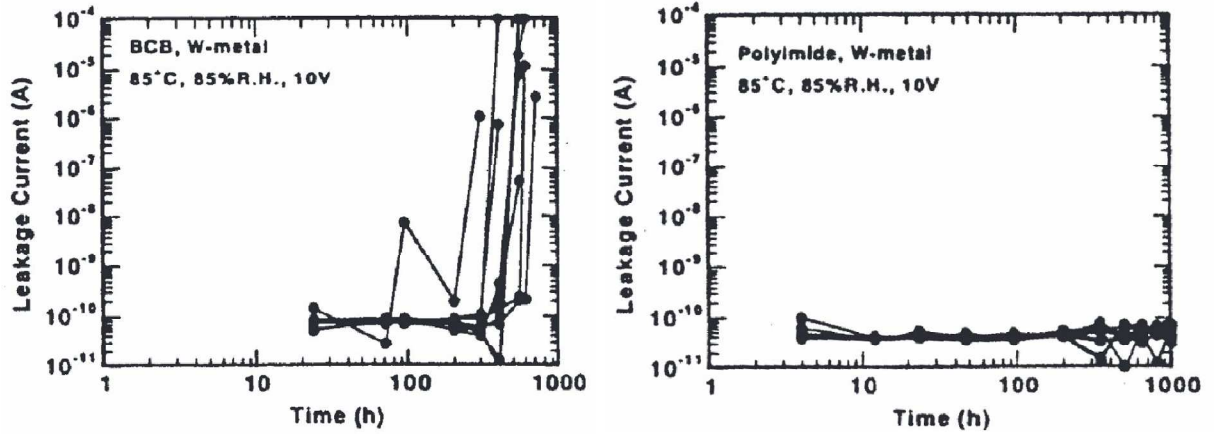


Figure 5.4: Leakage current measurements between parallel W/Au interconnects, passivated by either BCB (**left image**) or polyimide (**right image**), adapted from [110].

interfaces [99]. Quartz was recommended as substrate was for the impedance monitoring in IDE electrical test, because of its minimal parasitic influence [100].

In regard to polyimides, a low-moisture-absorption BPDA-PPD polyimide was recently developed. Rubehn et al. [106] demonstrated that it preserves most of its mechanical properties when soaked in PBS at 37°C or 60°C for 20 months, and advised not to test this polyimide at 85°C, as it does not follow the Arrhenius relationship. In parallel, Sugitani et al. [110] revealed that the ability of a device passivation to absorb water does not account for the device degradation under accelerated moisture aging, but rather the moisture impermeability of the passivation and the adhesion at the passivation-interconnect interface. W or WN thin films were recommend as adhesion promoters for Au interconnects passivated by polyimide [110].

5.2 IDE Sensors: Materials & Methods

State-of-the-art ECoG MEAs rely on parylene C as non-hermetic packaging material and electrical insulation. The long-term performance of Parylene C has been demonstrated in-vitro by means of parylene-coated IDE samples kept in saline at 37°C for 60 days [95], and in-vivo: 370 days for an ECoG MEA [52] and 1000 days for a Utah-needle array [92].

BPDA-PPD polyimide has recently emerged with a relatively low moisture-absorption coefficient and low CTE²⁰. Rubehn et al. demonstrated that BPDA-PPD polyimide preserves its mechanical properties when kept in PBS at 37°C and at 60°C in the course of 20 months [106].

To understand the degradation mechanisms behind the formation of parasitic shorts in our ECoG device (see previous Chapter), we set to investigate the long-term performance of the

²⁰coefficient of thermal expansion

BPDA-PPD polyimide, because we used exactly this material as flexible insulation in the array microfabrication. For this purpose, we realized golden IDE capacitive test structures on a quartz substrate²¹, and covered them by a $5\mu\text{m}$ -thick insulation film – either BBDA-PPD polyimide or parylene C. After mounting glass cylinders on top, and filling them with saline, we thus constructed a test set-up to monitor the diffusion of saline into the thin-film coating (volume diffusion). By applying an AC potential of several mV at the IDE capacitive structure, changes in the dielectricity of the corresponding coating material were tracked upon saline diffusion²². We designed the set-up in such a way as to restrict the saline diffusion only to the volume of the coating material (*in-vivo* also interfacial diffusion takes place²³) to allow deeper understanding of how volume diffusion process solely affects the formation of parasitic shorts.

This Section summarizes the theory and design on IDE capacitive structures, follows the fabrication process of these and describes the test set-up for volume diffusion. The obtained results on the saline absorption of both polyimide and parylene C turned out to be more intriguing than originally expected. To gain more information several physical tests were additionally performed on BPDA-PPD polyimide: FTIR²⁴, X-ray diffraction and water-vapour permeability. The volume diffusion results together with the physical investigations not only disclosed partially the trigger for the formation of parasitic shorts but also revealed BPDA-PPD polyimide as a very promising thin-film packaging material for ECoG electrode arrays.

5.2.1 Theory: Choice of Optimal Parameters

In this project interdigitated (IDE) capacitive structures were used to sense how salt water diffuses into thin-film polymeric coatings. To highlight their operation principle, two-plate capacitors are reviewed, both in a parallel and planar configuration. This theory provides basis for the subsequent design of our specific IDE structures.

Electricity-to-Go arose by accident in the 1740s as three scientists²⁵ independently discovered that a jar filled with water can store electrical charge [112], [113]. Since scientists at that time believed electricity to be a fluid, they looked for ways to "condense" and store it in jars [114]. During one such experiment Musschenbroek used an electrostatic generator to put charge in a water-filled glass jar via a metal rod inserted in it. The jar's exterior was covered with a metal foil and when he held the jar with one hand and touched the inserted metal rod with the other, he experienced a severe electrical shock, "shaken as if by a lightning stroke" [115]. Soon, the

²¹quartz was suggested in [100] as best substrate material for IDE tests

²²due its highly polar nature water has a dielectric constant by far larger than that of polyimide or parylene

²³it begins at an electrode opening, continues along a metal-polyimide interface and reaches the connector

²⁴Fourier transform infrared spectroscopy

²⁵Bose, von Kleist and van Musschenbroek [112]

power of this Leyden jar²⁶ to hold and release high amounts of charge made it the first portable source of electricity, as it was more compact and could store much more charge than electrostatic generators. Today, this power of the Leyden jar, known as the first capacitor, is used to provide the powerful discharge of heart defibrillators and its ability to store precise amount of charge has enabled computer RAM memory, among many other electronic applications [115].

Once the Leyden jar was invented, many scientists tried in vain to reproduce its storage power: during the experiment they stood on a wax-isolated ground²⁷ [115] and by charging the inner walls of their jars by an electrostat, the charge escaped the jars once the electrostat was removed (Fig.5.5A). Success came when a proper connection to ground was provided, so that electrons could flow from earth, via the experimenter body, to the outer metal foil of the jar and thus "keep" the excess positive charge from escaping (Fig.5.5B). In such a way relatively high amount of charge could be stored in the jar, so that when the experimenter held with one hand the outer metal foil of the jar and touched the metal rod connected to the inner foil, the electrons from the outer foil flew – via the experimenter body – to the inner one (the capacitor was discharging), and a severe electric shock was experienced.

Benjamin Franklin used the Leyden jar to capture lightnings. He also "dissected" it to investigate where exactly the charge was stored – on the inner/outer metal foils or in the dielectric of the jar's glass container. For this purpose, once he charged the jar, he removed its inner and outer metal foils and brought them in contact, but no discharge (in from of spark) was observed. This was strange as he expected the metal foils to be charged. Then he inspected the glass and felt by his hand some electrostatic electricity. Assembling back the metal foils of the jar, and this time connecting them produced a spark. Nowadays, this effect is explained as follows: during the removal of the metal foils from the jar, their charges are forced to spread on an ever decreasing area, leading to an increasing electrical field strength between the foils; at some point during the removal the electrical field becomes strong enough to ionize the air between the metal foils and the glass container which enables negative charge from the outer metal surface to be pulled into the glass and other negative charge from the glass into the inner foil [116].

Parallel-plate capacitor is the modern name of the Leyden jar and it stores charge in its dielectric, as Benjamin Franklin discovered [114]. Early scientists realized that by making the glass thinner, the metal foils larger and connecting several jars together, the amount of stored charge increased. Hence, the storage unit was named jar. As electrical measurements became

²⁶named after the city of the inventor Musschenbroek

²⁷common at the time to prevent charge from escaping [115]

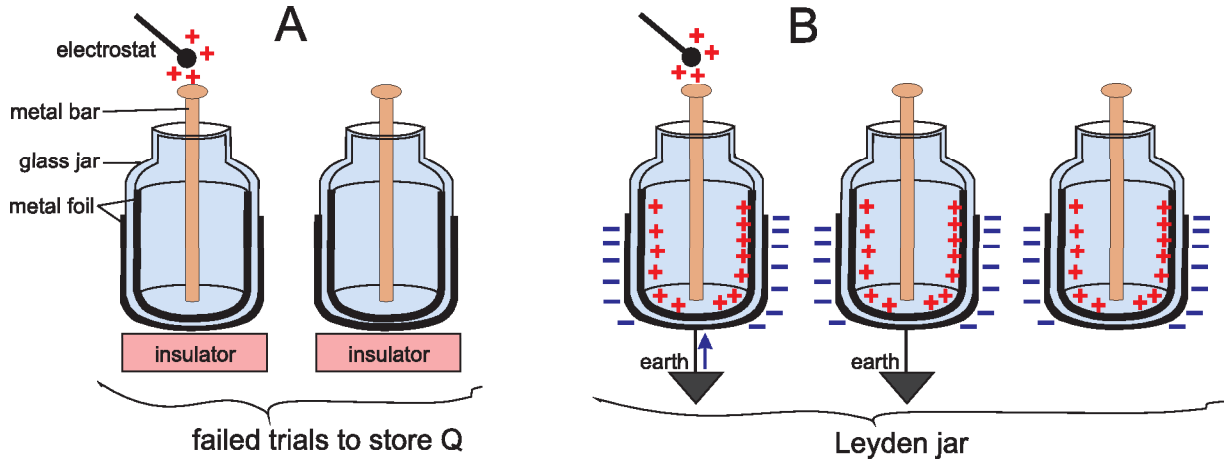


Figure 5.5: Attempts to store charge Q in a glass jar, lined with an inner and outer metal foil: (A) unsuccessful and (B) the first capacitor; Leyden jar image adopted from [113] and mechanism description adopted from [117], [118].

more accurate, the measurement unit was renamed in Farad²⁸ and the ability to store charge in capacitance C . Volta measured that the amount of charge Q put on a metal sphere (one-plate capacitor) is linearly proportional to the resulting voltage V on the plate

$$Q \propto V \Rightarrow Q = C \cdot V \Leftrightarrow C = \frac{Q}{V} \quad [F] \quad (5.1)$$

In general, capacitance C is a useful quantity, as it does not depend on its charge or voltage values, but is a function of geometry and material of a given capacitor [115].

For one-plate capacitor, such as a metal sphere, the potential on its surface can be expressed as if coming from a point charge $V = (kQ)/r$. Based on this, its capacitance scales linearly with the radius of the sphere

$$C = \frac{Q}{V} = \frac{Qr}{kQ} = \frac{r}{k} \quad [F] \quad (5.2)$$

whereas r is the radius of the metal sphere and $k = 1/(4\pi\epsilon_0)$ with ϵ_0 being the relative permittivity of free space²⁹ [115].

Considering now a two-plate capacitor, a charge Q of equal but opposite sign is put on each plate of area A , separated at a distance d from each other (see Fig.5.6A). The charge density on each plate is then $\sigma = Q/A$. The electrical field of each charged plate is $E_p = 2\pi k\sigma$, which makes $E_t = 2E_p = 4\pi k\sigma$ in total (neglecting edge effects). Therefore the parallel-plate capacitance is defined as

²⁸after Michael Faraday, originally coined as too large unit and used nowadays in pF - μ F [114]

²⁹ $k \approx 9.0 \cdot 10^9 [(Nm^2)/C^2]$ and $\epsilon_0 = 8.85418781762 \cdot 10^{-12} [C^2/(Nm^2)]$

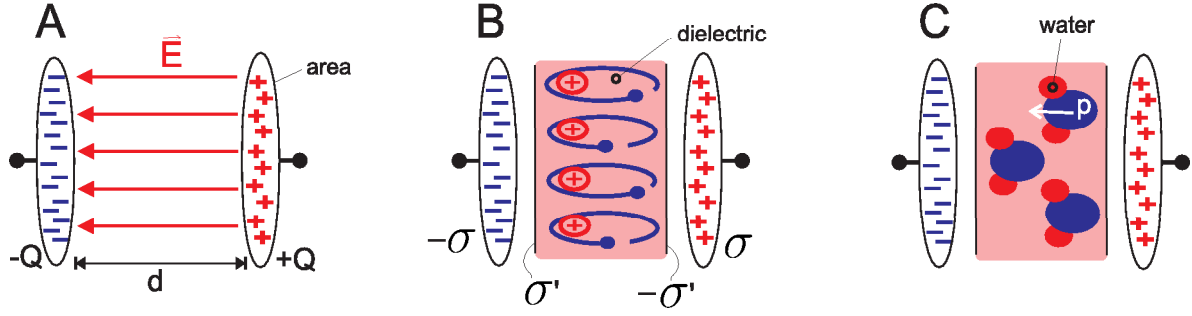


Figure 5.6: Parallel-plate capacitor: (A) distribution of electric field \vec{E} ; (B) a non-polar dielectric raises the capacitance due to induced surface polarization; (C) major increase in capacitance when this dielectric is filled with water; adopted from [114], [115].

$$C = \frac{Q}{V} = \frac{Q}{E_t d} = \frac{\sigma A}{4\pi k \sigma d} = \frac{A}{4\pi k d} \quad [F] \quad (5.3)$$

whereas the voltage is calculated from the work U done to move a test charge q in the field over a certain distance acc. $V = U/q = (F \cdot d)/q = E \cdot d$. To remark is that the electrical field E between the capacitor plates is independent of the position of a test charge in between the plates and it is normal to the plates. Moreover, it should be kept in mind that a capacitor plate contains $6 \cdot 10^{21}$ atoms in a 0.01 of a mole, and if made from copper ($2e/\text{atom}$) this makes a charge of $Q = 6 \cdot 10^{21} \times 3.4 \cdot 10^{-9} \text{ C} = -1920 \text{ C}$ due to its freely moving electrons and $+1920 \text{ C}$ due to its immobile positive ions. As a capacitor is charged usually with a fraction of a Coloumb (e.g. 0.001 C), the total charge difference in a metal plate, as a result, is fairly negligible [115].

Moreover, the capacitance of a parallel-plate capacitor with $A = 10\mu\text{m} \cdot 50\text{mm} = 0.5\text{mm}^2$ and $d = 10\mu\text{m}$ is 0.884 pF^{30} acc. Eq.5.3. In comparison, a metal sphere (one-plate capacitor) needs to have a surface area of 397.887 mm^2 (Radius= 5.62mm) acc. Eq.5.2 in order to reach the same capacitance value. This comparison reveals one reason why the Leyden jar made a breakthrough in 1740s (Fig.5.5B) and not the one-plate jar (Fig.5.5A).

The second reason for the relatively high storage capacity of the Leyden jar was the glass container. This dielectric material increased the overall capacitance by allowing more charge to be stored per unit area and hence decreasing the voltage difference ΔV between the plates (see eq.5.3) [115].

The amount by which a given dielectric material raises the capacitance is described by the *dielectric constant* or *relative permittivity* ϵ_r . The product of the relative permittivity together with the permittivity of free space ϵ_0 gives the *permittivity* ϵ i.e. $\epsilon = \epsilon_r \cdot \epsilon_0$.

³⁰this value is $< \text{C}$ of commercially available capacitors, nevertheless its area is \approx area of our IDE structures.

How the dielectric constant ϵ_r affects the capacitance is illustrated in Fig.5.6B. The plates of a parallel-plate capacitor have charge densities $\pm\sigma$ and hence an electric field $E_t = 4\pi k\sigma$. When a dielectric material (e.g., glass or polymer) is placed between the capacitor plates, the molecules of the dielectric are polarized. The dielectric charge $\pm\sigma'$ due to polarization is opposite in sign to the plates charge (see Fig.5.6B). Moreover, most of the dielectric charge is spread on the surfaces closest to the metal plates, and the electric field strength decreases the further one moves into the dielectric volume. This surface charge cannot escape to the plates, provided the applied voltage is below a breakdown voltage value³¹. The electric field within the dielectric is defined as

$$E = 4\pi k\sigma - 4\pi k\sigma' = E_0 \left(1 - \frac{\sigma'}{\sigma}\right) = \frac{E_0}{\epsilon_r}, \text{ with } E_0 = 4\pi k\sigma \quad (5.4)$$

where $\epsilon_r = (1 - \sigma'/\sigma)^{-1}$. The larger ϵ_r , the more polarizable a given dielectric is and the larger its capacitance is.

The atomic polarizability α relates an applied E-field to the induced dipole moment \vec{p} within the dielectric. For a dilute gas, such as air, the induced charge density in the dielectric is relatively small and acc. Eq.5.4 the following relation for \vec{p} is obtained

$$\vec{p} = \alpha \cdot \vec{E} \approx \alpha \cdot E_0 = \alpha \cdot 4\pi k\sigma \quad (5.5)$$

considering only the effect of E due to $\pm\sigma$ on the capacitor plates.

Therefore, the induced charge density can be expressed as the superposition of all dipole moments of the air molecules

$$\sigma' = n \cdot \vec{p} = n \cdot \alpha \cdot \vec{E} \approx \alpha \cdot 4\pi k\sigma \quad (5.6)$$

where n is the atomic gas density.

With $\epsilon_r = (1 - \sigma'/\sigma)^{-1}$ the following relation for ϵ_r acc. Eq.5.6 is obtained

$$\epsilon_r \approx 1 + 4\pi kn\alpha \quad (5.7)$$

This equation relates the dielectric constant to the polarization effects within a dielectric, implying that "the higher the density and the higher the polarizability, the larger the dielectric constant ϵ_r " [115]. Nevertheless, this relationship becomes much more complicated for denser dielectrics such as liquids or solids, but still can be qualitatively applied to denser materials provided they do not have a permanent electric dipole moment. For polar molecules, such as water, a small electric field can be enough to align them, resulting in a very large dielectric constant, for water in the range of 34-80.

³¹the higher ϵ_r , the higher the breakdown voltage

Coplanar-plate capacitor was implemented in micro-technology for various sensing applications: from pressure and humidity sensors, to microfluidics [119]. In this Work, this capacitive structure could be used to simulate two neighbouring electrodes in the ECoG MEA. When covered by a thin film, such as a polyimide coating and exposed to fluid ambient such as salty water, the capacitor plates would sense the diffusion of salty water into the coating. This would shine more light on the formation of parasitic short-circuits, observed during the long-term in-vivo usage of the ECoG MEA (see previous Chapter). However, optimal diffusion monitoring requires all electrical field lines, which flow from one to the other capacitor plate, to stay confined within the thin-film coating. This in turn depends on capacitor parameters such as plate width w , plate interdistance d , and coating thickness T (see Fig.5.7.A). The following calculations lead to a relation between these three basic parameters.

The coplanar-plate capacitor is characterized by two plates situated horizontally next to each other, which allows their implementation in the layer-by-layer fabrication common for micro-technology. Nonetheless, when charged, the coplanar plates give rise to an elliptically-shaped electrical field (see Fig.5.7A), which turns the calculation of the associated capacitance into a challenging task.

In general, the capacitance between any two plates can be calculated with the Laplace equation³², provided the voltage distribution is known and no charge storage occurs in the space between them. Practically, obtaining analytical solutions to this elliptical partial differential equation can be complicated. Instead, conformal mappings came into use. They can transform an elliptically-shaped E-field in z into a parallel-lined E-field in w , whereas both z and w are two different complex planes (Fig.5.7B). The power of this technique lies in its ability to preserve the angles between the equipotential lines and E-field lines i.e. the equipotential lines intersect the E-field lines always at right angles, in both z and w planes [121]. The distribution of the uniform E-field in the w -plane can be easily calculated and then transformed back to the z -plane so that it fits the boundary conditions of a given system in z e.g. plates configuration and values of plates potential [122], [123].

However, knowledge of the boundary conditions alone is not sufficient to determine the proper conformal mapping which will satisfy them. For this purpose there are tables with conformal transformations, which can be applied individually or even combined in series [123]. In most cases, the search for the right conformal mapping goes over trial and error.

And yet, in 1956 Escher constructed a fascinating conformal mapping – the lithograph "Print Gallery" – without any knowledge of complex functions. Fig.5.7C shows his creation – a disturbed scenery with "a young man looking with interest at a print on the wall of an

³² $\nabla\varphi = 0$, an elliptic partial DGL, whose solutions have no local maxima or minima, and the property that "the average value over a spherical surface is equal to the value at the center of the sphere" [120].

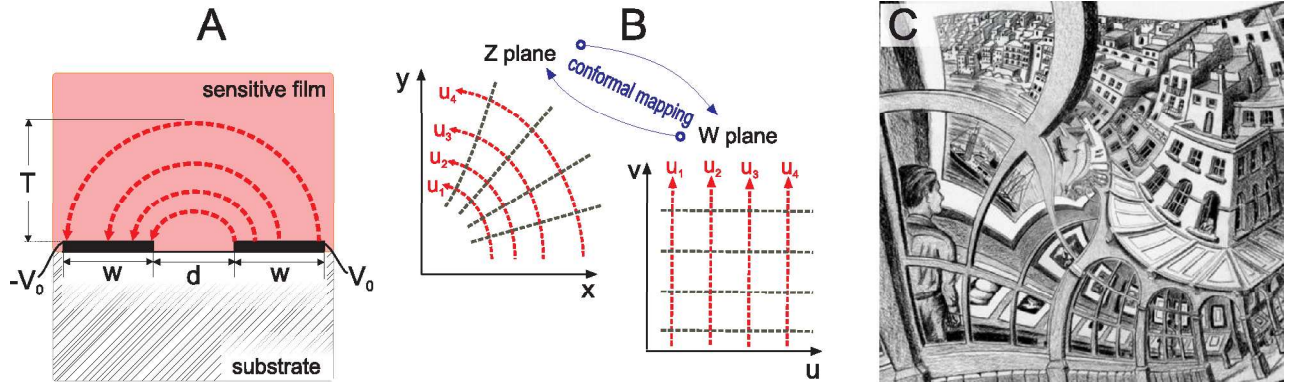


Figure 5.7: (A) Elliptically-shaped E-field in a coplanar-plate capacitor with plate width w , plate gap d and E-field penetration depth T ; (B) Conformal mapping of elliptically-shaped E-field in z -plane to a uniform E-field in w -plane: right angles between E-field lines and equipotentials are preserved during the mapping; (C) Escher's lithograph "Print Gallery" – a conformal mapping based on a spiral without beginning or end; adopted from [119], [123], [124].

exhibition that features himself³³ [125]. In his original work, Escher left a blank area in the middle of the picture, not able to complete the cycle origin. Recently, the mathematician Lenstra found the conformal mapping which satisfied the "boundary conditions" – a complex exponential function – and based on it completed the picture [125], [124]. A video of the never-ending "Print-Gallery" exponential cycle can be viewed in [126].

In regard to calculating a coplanar-plate capacitance, the *Schwarz-Christoffel* conformal transformation is most pursued [121]. This transformation maps an upper half-plane in z to a polygon in w [127], but at the same time it requires "tedious integral calculations" [121] to deliver an analytic solution in form of elliptical integrals³⁴. Alternatively, a *inverse-cosine* conformal mapping was applied by Chen et al. 2004 [119], and based on this, he found the coplanar-plate capacitance by a very intuitive approach. This procedure is presented as follows.

Consider the coplanar capacitance in Fig.5.7A. By charging its plates with $\pm Q$, a curvilinear electrical field \vec{E} is established at a potential difference of $2V_0$. In general, Volta found that the amount of a charge Q put on a metal plate is linearly proportional to the resulting voltage V and coined this relation as capacitance (see Eq.5.1). Based on this, we can determine the coplanar-plate capacitance as

$$C = \frac{|Q|}{2V_0} = \frac{\int_A \sigma dA}{2V_0} \quad (5.8)$$

where σ is the surface charge density on the coplanar plate, which is also induced as $-\sigma'$ in the surface of the dielectric medium situated closest to the plate (see Fig.5.6B) and A is the

³³"How can this be? Perhaps I am not far removed from Einstein's curved universe" a letter to his son [125].

³⁴ $C = \frac{\epsilon_0 \epsilon_r}{2} \frac{K(\sqrt{1-k^2})}{K(k)}$, with K being elliptical integrals and $K(k) \approx \int_0^1 \frac{dt}{\sqrt{(1-t^2)(1-k^2t^2)}}$ [121].

surface area of the plate.

Next, the charge density σ can be obtained by calculating the *divergence* of the E-field according to *Gauss's Law*

$$\vec{\nabla} \circ \vec{E} = \frac{\sigma}{\epsilon_0} \quad (5.9)$$

where $\vec{\nabla}$ is the *nabla* operator which in our case stands for a 2D-gradient i.e. $\vec{\nabla} = \left(\frac{\partial}{\partial x}, \frac{\partial}{\partial y} \right)$ and \circ is the scalar product. The term " $\vec{\nabla} \circ$ " stands the *divergence* of a given vector field. The term *divergence* was coined by Maxwell and Heaviside as the rate at which E-field lines flow away from a positive charge [128]. In other words divergence is "outflow minus inflow" at a specific point in space (here flow = flux); points of positive charge are *sources* of flow and negative charges are *sinks*.

To get a notion of what divergence is, consider the image of a positive charge in Fig.5.8: (A) shows the potential field; (B) E-field expressed as the gradient of the potential³⁵ and (C) the divergence of the E-field. At the charge origin the outflow of E-field lines \gg inflow, therefore its divergence at that specific point has a positive value i.e. $\vec{\nabla} \circ \vec{E} \gg 0$. As one moves away from the charge origin, the amplitude of the E-field decreases rapidly ($E \propto 1/r^2$), therefore the divergence becomes zero $\vec{\nabla} \circ \vec{E} = 0$ at all points away from the charge origin³⁶.

Consequently, the divergence of the E-field in the dielectric medium of our coplanar-plate capacitor is zero

$$\vec{\nabla} \circ \vec{E} = 0 \quad (5.10)$$

i.e. there are no sources or sinks present and therefore no change of flow rate is observed within the dielectric volume [128]. At the same time, the E-field strength can be expressed in terms of the electrical potential acc. $E = -\vec{\nabla}V$.

Substituting the latter relation into Eq.5.10 gives the *Laplace equation*

$$\vec{\nabla} \circ \vec{E} = \vec{\nabla} \circ (-\vec{\nabla}V) = -\vec{\nabla}^2 V = 0 \quad (5.11)$$

where " $\vec{\nabla} \circ \vec{\nabla}$ " = $\vec{\nabla}^2$ is the *Laplacian operator* and stands in our case for the *divergence of a 2D-gradient of a vector field* i.e. it measures the *curvature* of a vector field. To get a notion for $\vec{\nabla}^2$, consider the following example: the Laplacian operator in 1D is the second derivative $\vec{\nabla}^2 = \frac{d^2}{dx^2}$; to fulfill Eq.5.11 this derivative must vanish $\vec{\nabla}^2 = \frac{d^2}{dx^2} = 0$; the latter can only be true if the function to which the Laplacian operator is applied does not have any local maxima or

³⁵In moving a +charge to a -capacitor plate over a distance Δx work W is done by the E-field; the electrical potential ΔV is def. as work done per unit charge $\Rightarrow \vec{E} = \frac{F}{q} = \frac{W}{\Delta x} \cdot \frac{1}{q} = -\frac{\Delta V q}{\Delta x} \cdot \frac{1}{q} = -\frac{\Delta V}{\Delta x}$ [129].

³⁶one can visualize divergence by means of water flow. Once particles are introduced in the flow, if they get dispersed, then there is a flow source ($\vec{\nabla} \circ \vec{E} \gg 0$); if they become compressed, then there is a sink of flow ($\vec{\nabla} \circ \vec{E} \ll 0$); if the flow rate does not change, then there are no sources/sinks ($\vec{\nabla} \circ \vec{E} = 0$) [128].

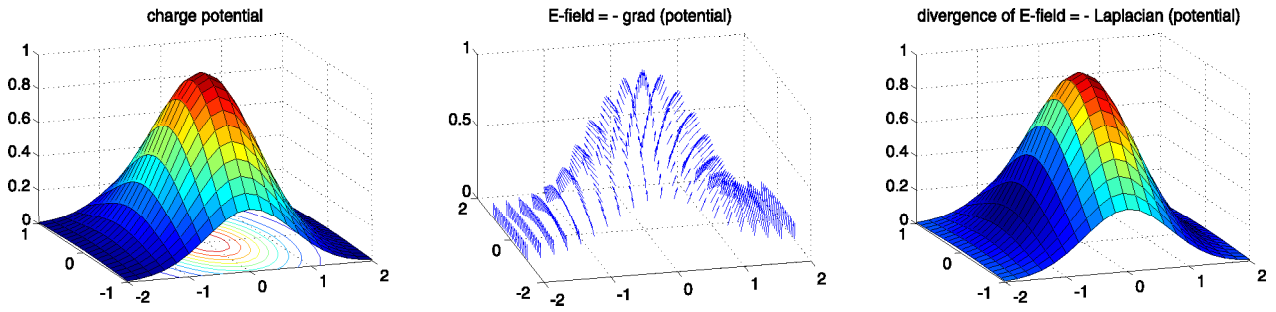


Figure 5.8: A positive electric monopole: (A) scalar potential field V ; (B) 3D E-field i.e. 3D gradient of the potential field ($\vec{E} = -\vec{\nabla}V$); (C) Divergence of E-field $\vec{\nabla} \circ \vec{E} = -\vec{\nabla}^2 V$; adopted from [130].

minima at the point of application i.e. function slope is constant. Back to the E-field example this would imply that the flow of the E vector field is constant (no sources or sinks)³⁷.

Having obtained a relation between a charge density and the divergence of its E-field (Eq.5.9), and linking this E-field to the potential gradient (Eq.5.11), the coplanar capacitance calculation can be expanded from Eq.5.8 to the following expression

$$C = \frac{|Q|}{2V_0} = \frac{\int_A \sigma dA}{2V_0} = \frac{\int_A (\epsilon_0 \vec{\nabla} \circ \vec{E}) dA}{2V_0} = \frac{\int_A (-\epsilon_0 \vec{\nabla}^2 V) dA}{2V_0} \quad (5.12)$$

In order to obtain an analytical expression for the above capacitance, the Laplace equation $\vec{\nabla}^2 V = 0$ should be solved. To find a direct analytical solution to this 2nd-order differential equation is a highly challenging task. Instead, a conformal mapping which fulfills the boundary conditions of our coplanar-plate system is pursued. For this purpose Chen et al. [119] applied the *inverse-cosine* conformal mapping, which is described next.

Charging two infinite conformal plates, separated by a gap, gives rise to an elliptically-shaped E-field. In the x/y-plane the E-field lines are orthogonal to each plate and intersect the y axis at right angles. The associated equipotentials are orthogonal to the E-field lines and take the shape of hyperbolas (see Fig.5.9A). For the sake of simplicity, a uniform E-field distribution would be highly advantageous, such as the one in a parallel-plate capacitor, as it enables straightforward calculus. Indeed, this can be achieved by altering the axes from straight lines (x and y) so that they take the shape of curvilinear coordinates (u and v) and begin to spread "in-parallel" to the hyperbolas and ellipses. This is exactly what the *inverse-cosine* conformal mapping does – it takes the Cartesian coordinates in z and transforms them in orthogonal elliptical ones in w (see Fig.5.9A) according to

$$w = \cos^{-1} z \quad (5.13)$$

³⁷1D-example adopted from physics.stackexchange.com/questions/20714/laplace-operators-interpretation

where $w = u + jv$ is the complex 2D-space of the elliptic coordinates and $z = x + jy$ is the complex plane of the Cartesian coordinates [123].

Each axis can be separately transformed as follows

$$x + jy = \cos^{-1} z = \cos(u + jv) = \cos u \cdot \cosh v - j \sin u \cdot \sinh v \quad (5.14)$$

$$x = \cos u \cdot \cosh v \quad (5.15)$$

$$y = -\sin u \cdot \sinh v \quad (5.16)$$

By squaring Eq.5.15 and Eq.5.16 and expressing them as a function of u gives

$$\cos^2 u = \frac{x^2}{\cosh^2 v} \quad (5.17)$$

$$\sin^2 u = \frac{y^2}{\sinh^2 v} \quad (5.18)$$

By summing up Eq.5.17 and Eq.5.18 and applying $\cos^2 u + \sin^2 u = 1$, the ellipse equation is obtained

$$\frac{x^2}{\cosh^2 v} + \frac{y^2}{\sinh^2 v} = 1 \quad (5.19)$$

The solutions to the above equation are plotted as concentric ellipses with foci at ± 1 in Fig.5.9A and correspond the E-field lines.

The second coordinate is the hyperbola, which is obtained in a similar way by expressing the Eq.5.17 and Eq.5.18 as a function of v , and applying $\cosh^2 v - \sinh^2 v = 1$

$$\frac{x^2}{\cos^2 u} + \frac{y^2}{\sin^2 u} = 1 \quad (5.20)$$

Equations 5.19 and 5.20 represent infinite number of concentric ellipses and hyperbolas. A specific solution to $\vec{\nabla}^2 V = 0$ can be obtained by matching the inverse-cosine transfer function (Eq.5.13) to the boundary conditions of a given electrode (plate) system according to

$$w' = C_1 \cos^{-1}(nz') + C_2 \quad (5.21)$$

whereas C_1 , n and C_2 are constants: C_1 scales the magnitude of potential on right metal plate (for $u = 0$); n is inversely scales the gap between the plates and C_2 scales the potential on the left metal plate (for $u = 2\pi$) [123].

To obtain a solution to our coplanar-plate problem, we need to find the values of the above three constants. Fig.5.9B shows a configuration of two coplanar plates, which lie on the x-axis and spread from $\pm a$ to $\pm\infty$, respectively.

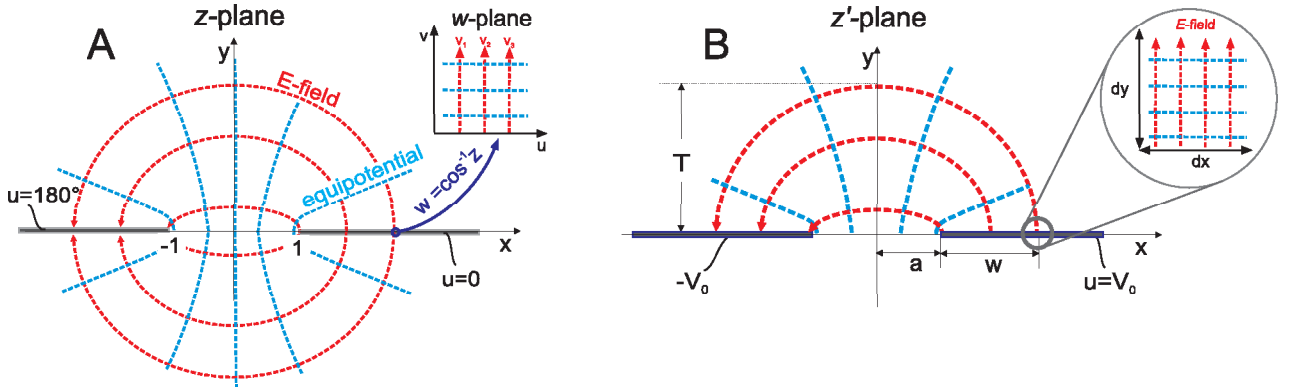


Figure 5.9: Charged coplanar plates: (A) Elliptical E-field and hyperbolic equipotentials in z-plane transformed to straight lines in w-plane; (B) E-field distribution depends on gap $2a$ and potentials $\pm V_0$. E-field is orthogonal to the plate surface (zoom); adopted from [123].

With $z = nz'$ and applying Eq.5.13 we can make the following substitution

$$w'(u' + jv') = C_1 \cos^{-1}(nz') + C_2 = C_1 \cos^{-1}(z) + C_2 = C_1 w(u + jv) + C_2 \quad (5.22)$$

In our case, we link u' to the electrical potential in V and $\epsilon v'$ to the electrical flux in C/m [123]. In our case the plate potentials are both real values $\pm V_0$. Accordingly, the constants C_1 and C_2 are taken as real values [123]. Hence Eq.5.22 reduces to the following expression

$$u' = C_1 u + C_2 \quad (5.23)$$

Now we can determine the C_1 , n and C_2 constants by comparing Fig.5.9A with Fig.5.9B.

1. We want $z' = a$ when $z = 1$; with $z = nz' \Rightarrow 1 = az' \Rightarrow \underline{n = 1/a}$
2. We want $u' = V_0$ when $u = 0$; with $u' = C_1 u + C_2 \Rightarrow V_0 = C_1 0 + C_2 \Rightarrow \underline{C_2 = V_0}$
3. We want $u' = -V_0$ when $u = \pi$; with $u' = C_1 u + C_2 \Rightarrow -V_0 = C_1 \pi + V_0 \Rightarrow \underline{C_1 = -2V_0/\pi}$

Inserting the above constants in the inverse-cosine transformation of Eq.5.21 gives

$$w' = -\frac{2V_0}{\pi} \cos^{-1} \left(\frac{1}{a} z \right) + V_0 \quad (5.24)$$

By rearranging Eq.5.24 the following expression for z is obtained

$$z(x + jy) = a \cos \left(\frac{\pi}{2V_0} (V_0 - w'(u' + jv')) \right) \quad (5.25)$$

Similar to Eq.5.15 and Eq.5.16 each coordinate is expressed separately

$$x = a \cdot \underbrace{\cos\left(\frac{\pi}{2V_0}(V_0 - u')\right)}_{u''} \cdot \underbrace{\cosh\left(\frac{\pi}{2V_0}(v')\right)}_{v''} \quad (5.26)$$

$$y = a \cdot \underbrace{\sin\left(\frac{\pi}{2V_0}(V_0 - u')\right)}_{u''} \cdot \underbrace{\sinh\left(\frac{\pi}{2V_0}(v')\right)}_{v''} \quad (5.27)$$

where V_0 is a real quantity, $\cosh(-x) = \cosh(x)$ and $\sinh(-x) = -\sinh(x)$.

The above relations can be used to find an analytical expression for the coplanar-plate capacitance shown in Fig.5.9B. In general, a given capacitance can be determined if an expression for its E-field distribution is known (acc. Eq.5.12). In general, the E-field can be then expressed as $\vec{E} = -\vec{\nabla}V$. To simplify calculus, we consider the vicinity of the right plate ($y \rightarrow 0$), where the E-field lines are orthogonal to the plate $\frac{\partial E}{\partial x} = 0$. As we linked the potential to u' this implies

$$\vec{E} = -\vec{\nabla}V = -\frac{\partial u'}{\partial y} \quad (5.28)$$

Applying the following differentiation rule

$$\frac{\partial(u \cdot v)}{\partial y} = \frac{\partial u}{\partial y} \cdot v + u \cdot \frac{\partial v}{\partial y} \quad (5.29)$$

to Eq.5.27 gives

$$\partial y = - \left[a \cdot \frac{\partial(\sin u'')}{\partial y} \cdot \sinh v'' + \sin u'' \cdot \frac{\partial(\sinh v'')}{\partial y} \right] \quad (5.30)$$

In the vicinity of the metal plate $y \rightarrow 0$ and the E-field lines, represented by v' -ellipses, run parallel to y , hence $\frac{\partial v'}{\partial y} = 0$. Therefore we obtain

$$\partial y = -a \cdot \frac{\partial(\sin u'')}{\partial y} \cdot \sinh v'' \Leftrightarrow 1 = -a \cdot \frac{\partial u''}{\partial y} \cdot \cos u'' \cdot \sinh v'' \quad (5.31)$$

Substituting back $u'' = \frac{\pi(V_0 - u')}{2V_0}$ and $v'' = \frac{\pi}{2V_0}$ from Eq.5.27, and considering that on the plate $u' = V_0$, gives

$$1 = a \cdot \frac{\pi}{2V_0} \frac{\partial u'}{\partial y} \cdot \underbrace{\cos\left(\frac{\pi}{2V_0} \underbrace{(V_0 - u')}_0\right)}_1 \cdot \sinh\left(\frac{\pi}{2V_0} v'\right) \quad (5.32)$$

Rearranging the above equation and substituting it in Eq.5.28 provides an analytical expression for the electric field in the vicinity of the right metal plate i.e. $y \rightarrow 0 \wedge \vec{E}||y$

$$\vec{E}_y = \frac{\partial u'}{\partial y} = \frac{1}{a} \cdot \frac{2V_0}{\pi} \cdot \frac{1}{\sinh\left(\frac{\pi}{2V_0} v'\right)} \quad (5.33)$$

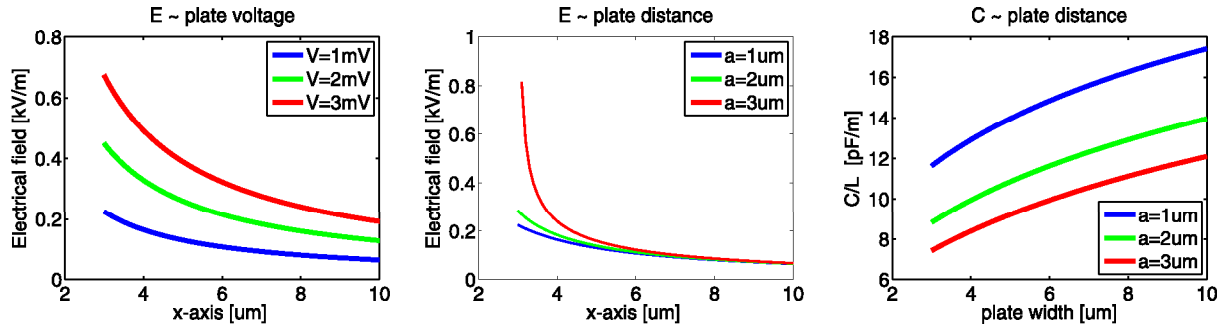


Figure 5.10: In the vicinity of the plate surface the E-field strength increases with larger plate voltage (left plot) and larger inter-plate distance a , for a in the range of x (middle plot); The coplanar capacitance per unit length as a function of w and a (right plot).

Fig.5.9B shows the dimensions of our metal plate: it is placed at a distance a from the y axis, has a width w and has a length l (the latter not shown). According to *Gauss's Law* [128] we can integrate the E-field in the vicinity of the plate to obtain its charge Q

$$\int_A \vec{E}_y \circ \hat{n} dA = \frac{Q}{\epsilon_0} \Rightarrow Q = \epsilon_0 \frac{2V_0}{a\pi} l \int_a^{a+w} \frac{1}{\sinh\left(\frac{\pi}{2V_0} v'\right)} dx \quad (5.34)$$

where \hat{n} is the normal vector of the surface area A of the plate.

In order to solve the above integral, we need to express v'' in terms of x by using Eq.5.26 and the fact that on the plate surface $u' = V_0$

$$x = a \cdot 1 \cdot \cosh\left(\frac{\pi}{2V_0} v'\right) \Rightarrow \frac{x}{a} = \cosh\left(\frac{\pi}{2V_0} (v')\right) \quad (5.35)$$

Then

$$\sinh\left(\frac{\pi}{2V_0} v'\right) = \sqrt{\cosh\left(\frac{\pi}{2V_0} v'\right) - 1} = \sqrt{\left(\frac{x}{a}\right)^2 - 1} \quad (5.36)$$

Substituting the above result in Eq.5.34 gives

$$Q = 2\epsilon_0 \frac{2V_0}{a\pi} l \int_a^{a+w} \frac{1}{\sqrt{\left(\frac{x}{a}\right)^2 - 1}} dx \quad (5.37)$$

Finally, we obtain the following analytical expression for our coplanar-plate capacitance

$$C = \frac{Q}{2V_0} = 2\epsilon_0 \frac{l}{a\pi} \int_a^{a+w} \frac{1}{\sqrt{\left(\frac{x}{a}\right)^2 - 1}} \Rightarrow C = 2\epsilon_0 \frac{l}{\pi} \left[\ln \left| x + \sqrt{x^2 - a^2} \right| \right]_a^{a+w} \quad (5.38)$$

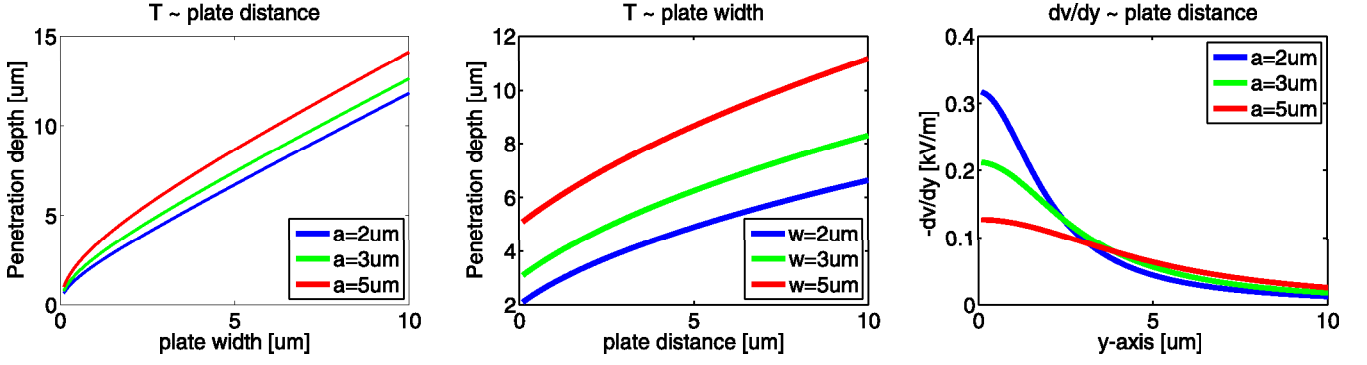


Figure 5.11: Penetration depth T : as a function of plate width w (left plot) and inter-plate distance a (middle plot); E-field distribution along the y -axis³⁹ (right plot).

$$C = 2\epsilon_0 \frac{l}{\pi} \left[\ln \left| a + w + \sqrt{(a + w)^2 - a^2} \right| - \ln |a| \right] \quad (5.39)$$

$$C = 2\epsilon_0 \frac{l}{\pi} \ln \left(1 + \frac{w}{a} + \sqrt{\left(1 + \frac{w}{a}\right)^2 - 1} \right) \Rightarrow C = 2\epsilon_0 \frac{l}{\pi} \operatorname{arcosh} \left(1 + \frac{w}{a} \right) \quad (5.40)$$

where $\ln x - \ln y = \ln \frac{x}{y}$, w is the width of the plate and $2a$ is the inter-plate distance.

In summary, the E-field strength³⁸ in the vicinity of the coplanar plate of Fig.5.9B scales with the applied plate voltage and inter-plate distance a . The latter holds only for the edge of the plate nearest to the gap, i.e. for a values in the range of x (Fig.5.10, left and middle plot). The coplanar capacitance per unit length C/L , derived from Eq.5.40, increases with plate width and decreases with plate distance, as shown in Fig.5.10, right plot.

The penetration depth T of the E-field into the dielectric material is shown in Fig.5.9B. In regard to the design of an IDE sensor, this quantity is important to reach maximum sensitivity. In our case, the coplanar electrodes are to be covered with an insulating layer – either polyimide or parylene. On top a cylinder of salt water is to be positioned. A most effective way to track the water diffusion into the insulation is to design the coplanar plates with most of the electrical field lines propagating within the dielectric material (and not outside of it). We can calculate the penetration depth T by using Eq.5.19, which describes a set of concentric ellipses, and inserting our boundary conditions (v'' instead of v and a instead of 1). As T is max for $x = 0$ (see Fig.5.9B) then the right term of Eq.5.19 vanishes, which gives

$$T = y_{x \rightarrow 0} = a \cdot \sinh v'' \quad (5.41)$$

We have already related \sinh to x in Eq.5.35, and T is max for $x = a + w$ which gives

³⁸combining Eq.5.33 and Eq.5.35, the E-field strength in the vicinity of the plate surface is $\vec{E}_y = \frac{2}{\pi} \frac{V_0}{\sqrt{x^2 - a^2}}$

$$T = a \cdot \sqrt{\left(\frac{x}{a}\right)^2 - 1} \Rightarrow T = a \cdot \sqrt{\left(\frac{w}{a} + 1\right)^2 - 1} \Rightarrow T = \sqrt{w^2 + 2aw} \quad (5.42)$$

where w is the plate width and a is the inter-plate distance.

For the case when $w = a$ the penetration depth becomes $T = w\sqrt{3}$, which is plotted in Fig.5.11 as a function of w and a in the left and middle image, respectively. Comparison of the left and middle plots reveals that plate distance has higher impact on the penetration depth T .

In practice, however, the choice of width, distance and penetration depth, is constrained by the limitations of the micro-system technology at IMSAS, namely a minimum structure resolution of $5 \mu\text{m}$. Hence, minimum width of $5 \mu\text{m}$ and distance of $5 \mu\text{m}$ would imply a penetration depth of $T = w\sqrt{3} = 5\sqrt{3} = 8.67\mu\text{m}$ i.e. this would be the right choice for coating thickness to ensure that all electrical field lines stay confined within the coating. And yet, coating thickness of $5 \mu\text{m}$ for polyimide and parylene had been already established at IMSAS as microfabrication flows, and altering it would mean changing deposition parameters and photoresist parameters.

Taking a closer look at the distribution of electrical field lines within the coating, shown in the right plot of Fig.5.11, reveals that lines are most concentrated in the vicinity of the electrodes. For a coating thickness of $5\mu\text{m}$ ⁴⁰, ca. 75 % of the field lines are confined within the coating, whereas the plate width = distance = $5\mu\text{m}$.

Hence, $5\mu\text{m}$ is considered here as optimal choice of coplanar capacitor parameters with respect to IMSAS photolithography constraints and established processes. Translation of these parameters into IDE-dimensions means fingers and interdistance equal to $10 \mu\text{m}$.

5.2.2 Design & Microfabrication

The design of our IDE sensor⁴¹ is shown in Fig.5.12A: it consists of coplanar capacitor plates and coating under test. By polarizing the capacitor plates, an elliptically shaped E-field is formed. As water diffuses into the polymer on top, the water alters the electrical properties of the polymer due its exceptionally large dielectric constant (ca. 80 at RT [131]), the capacitance between the microelectrodes increases and the overall impedance decreases. In practice, the capacitor plates are designed in form of interdigitated fingers (see Fig.5.12B), which increases the total length of the capacitor plates and enables reliable measurement of the capacitance/impedance (Eq.5.40). The real dimensions of our interdigitated sensor are shown in Fig.1C: 1). interdigitated microelectrodes, 2). contact pads for wire-bonding, 3). a microhole introduced into the

⁴⁰y-axis= 5

⁴¹The analytical expression for coplanar capacitance plate-width and -distance, and penetration depth serve here as a basis for the design of the IDE-sensor sensor.

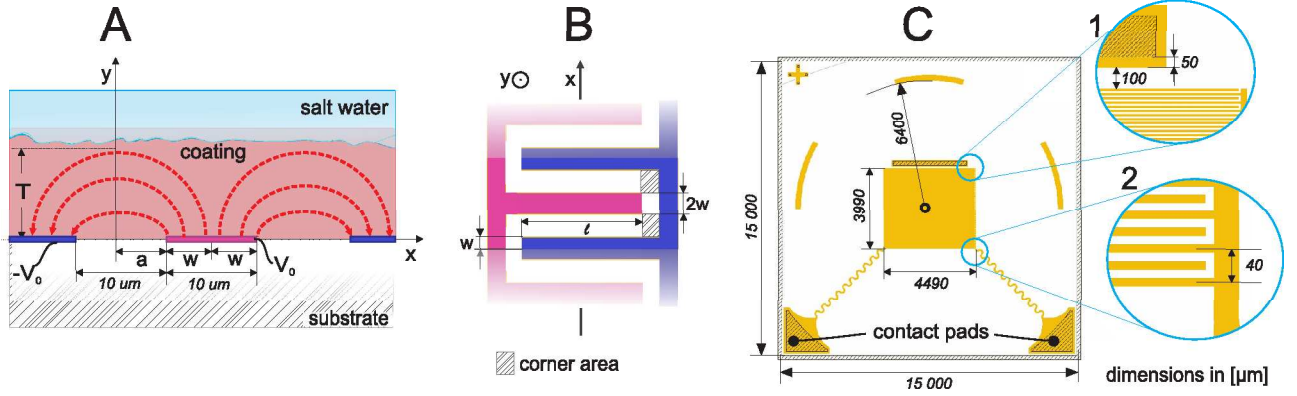


Figure 5.12: Interdigitated microelectrode sensors: A). View of sensor cross-section with middle capacitor plate set to a higher electrical potential than its neighboring plates, covered by a coating material of thickness T , subjected to diffusion of salt water (saline); B) Top-view of interdigitated finger microstructures; C). Real dimensions of interdigitated fingers, and contact pads, a coating microhole, situated $100 \mu\text{m}$ away from the top finger as an opening for lateral creeping of saline, and curves marking the position of a saline-filled cylinder.

coating as an opening for lateral diffusion of saline.

For the sake of symmetry the electrode width and electrode spacing were chosen to be equal ($2w = 2a$). In the sensor design the thickness of the coating was set to be $5 \mu\text{m}$, the same as in the *in-vivo* array, and IDE-fingers and interdistance equal to $10 \mu\text{m}$, as derived analytically in the previous Subsection.

Fig.5.12C shows the design of our interdigitated-electrode (IDE) sensor. According to Eq.5.40 and for $w = a$ the total capacitance C_0 in the absence of water diffusion is

$$C = \epsilon_0 \frac{L}{\pi} \operatorname{arcosh}(2) \cdot (\epsilon_c + \epsilon_s) \quad (5.43)$$

where L is the total length, and ϵ_c and ϵ_s are the dielectric constants of coating and substrate, respectively.

If a coplanar unit is defined acc. Fig.5.12A, then the length of such a unit in mm is

$$L_{unit} = 2(l + 2w) = 2(4490 + 5) \cdot 10^{-3} = 9 \quad (5.44)$$

whereas l and w are defined in Fig.5.12B. A coplanar unit is $40 \mu\text{m}$ wide, hence their number N is

$$N_{unit} = \frac{(3390 - 30)}{40} = 84 \quad (5.45)$$

Then the total length L of all coplanar units in mm is

$$L_{all} = L_{unit} \cdot 84 + l + 2w = 760,5 \quad (5.46)$$

Then the IDE capacitance C_0 of a polyimide coating with $\epsilon_{polyimide} = 3.4$ and $\epsilon_{SiO_2} = 3.9$ is

$$C_0 = 20.6pF \quad (5.47)$$

and the IDE-capacitance C_{H_2O} of a 5 μm -thick water film is

$$C_{H_2O} = 225.7pF \quad (5.48)$$

The water film capacitance is ca. 10 times larger than that of the polyimide film due to the large dielectric constant of water. This explains why IDE sensors are so sensitive to water diffusion.

The microfabrication of the IDE sensor is shown in Fig.5.13. A borosilicate glass wafer⁴² serves as substrate. The wafer is cleaned in Caro's acid⁴³ and sputter-coated with a 20/300 nm thick Cr/Au metallization (Fig.5.13A). The Au surface is treated with an O₂ plasma (500 W, 30 s) to promote good adhesion and a 1.8 μm -thick AZ 1518 photoresist is spin-coated. The resist is exposed for 2.5 s at 12 mW/cm² through an IDE-photomask (see Fig.5.12C) and developed in AZ 726 MIF. The photoresist capacitor structure is transferred into the Au film by wet etching in a Cyanide etch solution⁴⁴ (Fig.5.13B). The resist is stripped in acetone and isopropanol⁴⁵, and the Au structure is transferred into Cr by wet etching⁴⁶ (Fig.5.13D). The wafer is cleaned in Caro's acid and coated by either a 5 μm -thick parylene C or a U-Varnish-S polyimide film (BPDA-PPD type), as shown in Fig.5.13E. A 10 μm -thick AZ 9260 photoresist is spin coated and structured into contact openings and the parylene/polyimide is etched in an O₂ + CF₄ RIE-plasma. The resist is stripped in AZ100 (15 min at 50°C). The wafer is diced into chips.

Deposition of Polyimide U-Varnish-S polyimide film from UBE Europe GmbH (BPDA-PPD type) was deposited as follows: organosilane adhesion promoter VM651 was spin-coated for 60s@4000rpm and baked on a hotplate for 120s@120°C; a 5 μm -thick U-Varnish-S film (BPDA-PPD) was spin-coated for 40s@3000rpm and soft-baked for 5min@80-120°C and 5min @120°C on a hotplate. The polyimide curing took place in two different machines: (1) in a Centrotherm Belt Furnace in N₂ atmosphere, the oven situated outside of the clean-room⁴⁷, and (2) in a wafer-bonder machine⁴⁸, applying three different ambient conditions: (i) vacuum,

⁴²4", 500 μm thick BOROFLOAT® 33, chosen for minimal parasitic effects [100]

⁴³essential step for the adhesion; suggested to be performed directly before applying other materials

⁴⁴200mL *Au Etch plus* from Fa. Candor Chemie : 2g KCN : 800mL H₂O

⁴⁵otherwise the resist will be destroyed during the following Cr-etch step and contaminate the wafer with particles

⁴⁶250g C₆FeK₃N₆ : 120g NaOH : 1L H₂O; if by mistake resist not removed, Cr-etch solution "burns" it

⁴⁷Centrotherm Belt Furnace, Centrotherm, DE, 450°C peak temperature, 80 mm/min belt speed

⁴⁸Substratbonder SUESS SB6, SUESS MicroTec, DE

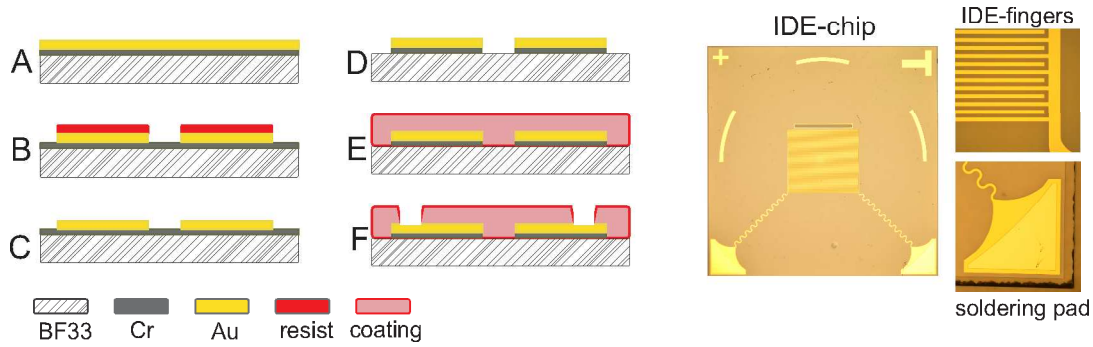


Figure 5.13: Microfabrication flow of IDE sensor for accelerated soak tests: (A) glass wafer sputtered with Cr/Au films, (B) Au film is structured into interdigitated fingers (see Fig.5.12.C), (B) the photoresist is stripped, (C) the structures of Au-film are transferred into Cr by a wet etching, (E) a coating-under-test is deposited into the microfingers, (F) the coating is opened at the microhole and at the contact pads. The produced sensor is $15\text{mm} \times 15\text{mm}$ and has $10\mu\text{m}$ -wide microfingers.

(ii) first evacuation, then flooding with N_2 , and (iii) only N_2 flooding. Both curing temperature profiles are plotted in Fig.5.14. The curing profile of the Centrotherm oven was mistakenly programmed to be of much shorter duration than the profile suggested by the manufacturer UBE Europe GmbH. This mistake became obvious when we transferred the polyimide curing to the bonder machine. The latter is 1:1 copy of the manufacturer profile. The short curing profile did not include a large pre-heating step, and herewith applied to show what role such a pre-heating step plays in the water-barrier properties of the BPDA-PPD polyimide.

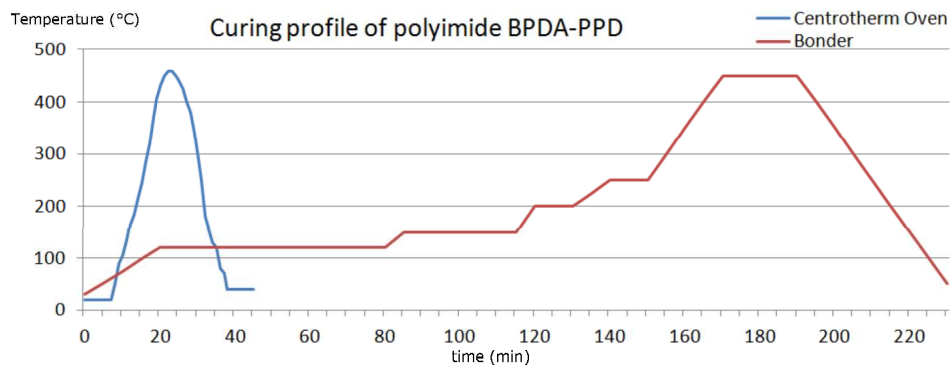


Figure 5.14: BPDA-PPD polyimide curing profile in a Centrotherm oven (short cure) and a wafer-bonding tool (long cure).

Deposition of Parylene Parylene C was deposited as follows: (A) the wafer was cleaned in Caro's acid followed by the application of the adhesion promoter Silane A-174 according to the procedure reported by Hassler et al. [99]; (B) the wafer was straightforward coated

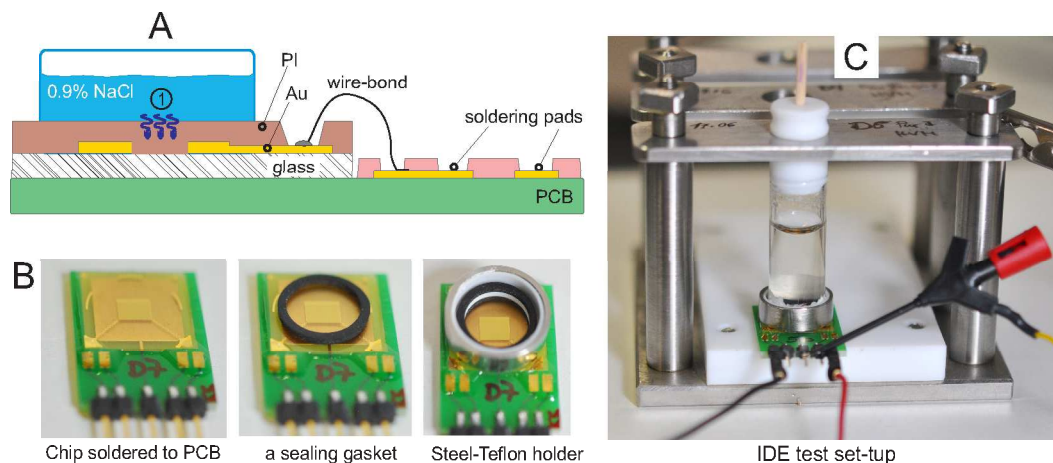


Figure 5.15: Accelerated soak test set-up: (A) cross-section of the IDE sensor assembled to a pre-designed printed circuit board, with wire-bonds serving as electrical connections, and a salt-water-filled cylinder mounted on top of the sensor; (B) Sealing mechanism: gasket, steel-teflon holder, sealing gasket; (C) Overall acceleration soak test set-up: IDE sensors with mounted water-filled glass cylinders, steel frame fixing the cylinders in place

with a 5 μm -thick parylene C layer in a polymerization process from the gas phase using the Labcoater 300 RW (Plasma Parylene Systems GmbH, Germany); during this coating process the wafer was kept at room temperature, while the pyrolysis of the used dimer Dichloro[2,2] paracyclophane ($\text{C}_{16}\text{H}_{14}\text{Cl}_2$) occurred at 760°C ; (C) parylene C was then structured using a 10 μm thick photoresist AZ9260 (MicroChemicals GmbH, Germany) in a RIE process with O_2 plasma to open the insulation of the soldering pads.

Fig.5.15.A shows the test set-up: (A) Assembly of IDE sensor to a pre-designed printed circuit board (PCB), whereas the sensor is glued with UHU plus endfest 300 to the PCB, then wire-bonded with 25 μm -thick AlSi1 wire to the PCB-pads (wire bonds covered also with UHU film), and a glass cylinder is mounted on top of the sensor, later to be filled with saline; (B) Cylinder mounting is realized as follows: a sealing gasket is positioned on top of the sensor, a Teflon-steel ring is mounted on top of the gasket and a second gasket is inserted into the holder; (C) Glass cylinders of 10/12mm inner/outer diameter are inserted into the Teflon-steel rings and fixed in place by a steel-frame. The cylinders are filled with 0.9%NaCl (saline) and kept @ 60°C (convection oven (SB22/160/40, Weiss Umwelttechnik GmbH, DE) for 175 days. If moisture is absorbed by the coating, the impedance between the IDE fingers is reduced, which is monitored by an electrochemical impedance spectroscopy (COMPACTSTAT.e, potentiostat, Ivium Technologies B.V., NL). In order to measure the impedance, a 10mV peak-to-peak sinus signal is applied between the interdigitated electrodes and the resulting current is measured in the same electrode configuration.

5.2.3 Results

The water-soaking properties of two polymeric films, polyimide BPDA-PPD (both Centrotherm & Bonder cured) and parylene C, were investigated by means of IDE sensors⁴⁹. Further, potential soaking accelerators such as (1) a hole in the polymeric film in the vicinity of the IDE structure, and (2) water-vapour sterilization were investigated.

Last but not least, special attention was paid to Bonder-cured BPDA-PPD polyimide and three groups of samples were cured at different ambient conditions — in vacuum, chamber evacuation+N₂ atmosphere, and N₂ atmosphere.

Preliminary IDE tests

In order to compare the water barrier of BPDA-PPD polyimide to that of parylene C, impedance data from three sample types were monitored. Fig.5.16 presents the impedance magnitudes obtained from: (1) BPDA-PPD polyimide cured in a Centrotherm oven; (2) parylene C; and (3) BPDA-PPD polyimide cured in a wafer-bonding tool (three samples per polyimide type and two samples per parylene C). The impedance data were recorded while keeping the samples in saline@60°C in the course of up to 175 days. Polyimide samples cured in Centrotherm oven decreased rapidly in impedance magnitude values within the first 7 days e.g. at 100 Hz from $3 \times 10^8 \Omega$ to $1 \times 10^6 \Omega$ (left plot in Fig.5.16), and remained in the latter impedance range for the rest of 175 days. Parylene C samples underwent a slight impedance decline during the first 3 days, e.g. at 100 Hz from $3 \times 10^8 \Omega$ to $3 \times 10^8 \Omega$, but continued to decrease at slow pace to $10^6 \Omega$ for the rest of 175 days (middle plot in Fig.5.16). Polyimide samples cured in Wafer-bonding tool underwent a negligible impedance drop at 100 Hz from $3 \times 10^8 \Omega$ to $2 \times 10^8 \Omega$ in the course of 170 days.

This first measurement shot shows that there is a high difference in the water-barrier properties of short-cured and long-cured BPDA-PPD polyimide. The latter excels even parylene C films deposited at IMSAS with Silane as adhesion promoter. The properties of these three coatings were investigated in detail in the following.

⁴⁹The lateral impedance Z_{lat} was investigated by means of IDE chips. All samples have 5 μm -thick coatings and the inter-IDE distance is 10 μm . A minor part of the of E-field lines propagates outside of the coating material and senses immediately the change of medium, namely from a dry state to a water-filled state (compare “dry” vs. “wet” in Fig.5.16). This implies 5 μm thickness as sufficient to incorporate most of the E-field lines and thus enable a detailed track of water diffusion into the coating. Hands on how to establish an IDE measurement set up is provided in the Appendix.

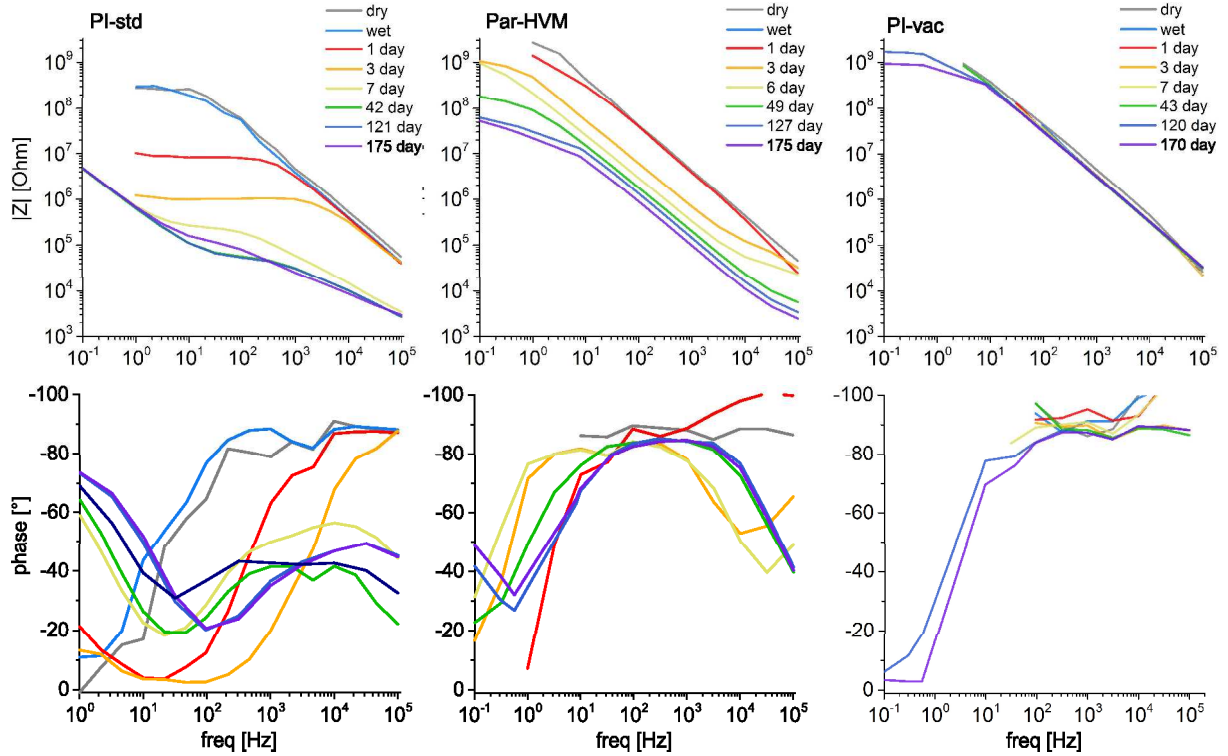


Figure 5.16: Impedance data obtained from accelerated soak tests obtained from: (A) BPDA-PPD polyimide cured in Centrotherm oven; (B) parylene C with Silane A-174 adhesion promoter; (C) BPDA-PPD polyimide cured in Wafer-bonding tool; 3 samples per each polyimide type and 2 samples per parylene C were monitored.

Long-Term Stability of Parylene C

The parylene C films were investigated of how adhesion, elevated temperatures and sterilization affect the water-barrier properties (at least two samples per condition type). Further, parylene films deposited at the SCS Coating company, a leading parylene distributor, were investigated also by means of IDE chips and used as a golden reference.

For the **parylene C samples deposited at IMSAS** we prepared the following sets of samples and derived their 100 Hz impedance magnitudes⁵⁰ ($|Z|@100\text{Hz}$), as shown in Fig.5.17:

- Samples with no adhesion promoter: $|Z|@100\text{Hz}$ of sample D1 declined very rapidly, namely from $2.14 \times 10^7 \Omega$ to $87.7 \times 10^3 \Omega$ upon saline immersion, the latter value obtained 10 min after water introduction. Additional heat treatment⁵¹ to seal the parylene surface did not provide any improvement (D2 & D3 in plot A). These results demonstrate that parylene C films, which adhere weakly to their substrates, cannot be used as water-protective

⁵⁰100 Hz is an essential frequency in ECoG measurements.

⁵¹> 24h at 60°C and 200°C in a vacuum oven

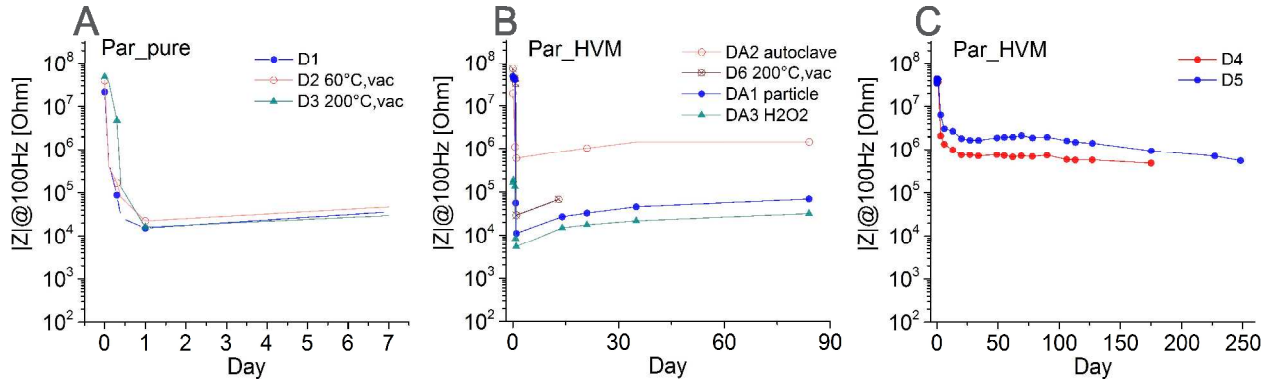


Figure 5.17: $|Z|@100\text{Hz}$ of IMSAS-parylene-C coated IDE structures: (A) without any adhesion promoter; (B) with Silane-A174 adhesion promoter and post treatment; (C) with Silane-A174 promoter, no post treatment.

coatings.

- Samples with adhesion promoter⁵² + post treatment: (1) heated in vacuum⁵³, (2) sterilization in an autoclave⁵⁴, and (3) sterilization in H_2O_2 ⁵⁵, (4) particle contamination. All these post treatments lead to a rapid decline of $|Z|@100\text{Hz}$ up to ca. $10^3 - 10^4 \Omega$ (see plot B), except for the autoclave sterilization (sample DA2), which preserved relatively high impedance within the span of 90 days. However, the latter case need to be repeated with more samples for the sake of statistics and to exclude other influence factors⁵⁶.
- Samples with adhesion promoter⁵⁷ and no post treatment: samples D4 and D5 in plot C maintained the highest $|Z|@100\text{Hz}$ in the course of 260 days⁵⁸.

In summary, the parylene C film should adhere sufficiently to its substrate in order to provide a high water-barrier. And yet, even if good adhesion is provided, particle contamination at the substrate-parylene interface or heating at 200°C can account for undesired water diffusion.

⁵²Silane A174

⁵³24h at 200°C in vacuum in a wafer-bonder machine SUESS SB6, SUESS MicroTec, DE

⁵⁴sterilization process conducted at AG Kreiter

⁵⁵for 24h conducted at AG Kreiter

⁵⁶During one of the autoclave sterilizations the samples were mistakenly packed in partially closed boxes, and little steam could enter the boxes.

⁵⁷Silane A174

⁵⁸sample D4 was stopped after 175 because of lack of sample holders

Parylene C deposited externally samples were prepared as follows: we sent IDE wafers for parylene coatings at SCS⁵⁹ to be coated with *AdProPoly* adhesion promoter + 5 μm -thick parylene C and *AdProPoly* + 15 μm -thick parylene C⁶⁰. Additionally, we sent IDE wafers to PPS⁶¹ to be coated with 5 μm -thick parylene C. The obtained $|Z|@100\text{Hz}$ data are presented in Fig.5.18:

- 5 μm -thick SCS-parylene samples performed comparably to 5 μm -thick IMSAS-parylene samples with adhesion promoter (compare Fig.5.18A with Fig.5.17C). The abrupt decline in the impedance magnitude of sample A6 occurred after mistakenly short-circuiting the pins of the IDE-structures by an ohmmeter.
- 15 μm -thick SCS-parylene samples behaved similarly to the 5 μm -thick SCS-parylene samples (no improvement in water-barrier quality due to increased thickness could be observed).
- a 5 μm -thick PPS-parylene sample, where no adhesion promoter was applied, performed in a comparable manner to the 5 μm -thick IMSAS parylene without adhesion promoter (compare Fig.5.18C with Fig.5.17A).

In summary, the parylene-C films coated at IMSAS (with Silane as adhesion promoter) performed in a comparable manner to externally deposited parylene-C films of SCS. The water-barrier of IMSAS-deposited films was even slightly higher, because most probably the externally deposited IDE-wafers were contaminated by the out-gassing wafer-carrier boxes used during transportation (ca. 2 weeks storage). Strangely enough, the water-barrier property of parylene C films was not influenced by the film thickness – both 5 μm and 15 μm thick SCS parylene films behaved in a comparable manner.

Long-Term Stability of BPDA-PPD Polyimide

Having demonstrated that IMSAS-deposited parylene-C films have water-barrier comparable to externally deposited parylene films, we set to investigate why long-cured polyimide films excelled not only short-cured polyimide films, but also parylene C.

The impact of **lateral diffusion & steam sterilization** was investigated as follows. Three sets of samples were cured in a wafer-bonding tool within vacuum ambient and micro-fabricated further as follows: (1) the polyimide fully protecting the IDE fingers and space around them, (2) a microhole etched into the polyimide film nearby the IDE fingers (see bottom plots in

⁵⁹SCS, a company situated in USA

⁶⁰we were told in a telephone conference with SCS that adhesion promotion is essential for water-barrier properties and that the thicker the parylene layer, the better the water-barrier

⁶¹PPS, a company situated in Germany

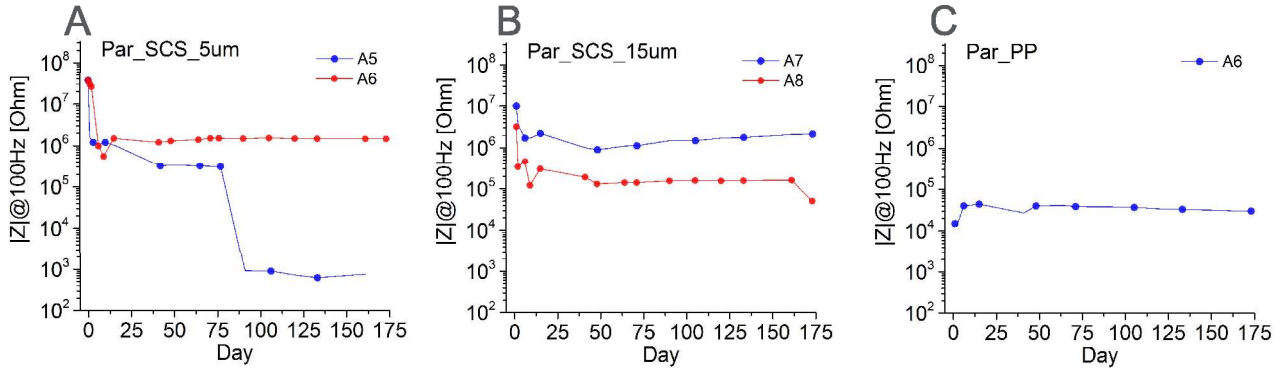


Figure 5.18: $|Z|@100\text{Hz}$ of IDE structures coated with parylene C outside of IMSAS: (A) $5\mu\text{m}$ -thick coating performed at SCS with *AdProPoly* adhesion promoter; (B) $15\mu\text{m}$ -thick coating performed at SCS with *AdProPoly* adhesion promoter; (C) $5\mu\text{m}$ -thick coating performed at PPS, no adhesion promoter.

Fig.5.12.C) to promote lateral diffusion of saline along a pyrex-polyimide interface, and (3) fully-protected IDE samples exposed to steam sterilization, the latter being a final step prior implantation of implantable biomedical devices. Fig.5.19 shows the impedance magnitudes obtained at 100 Hz of polyimide-covered IDE samples stored in saline @60°C for 175 days. From the impedance data only the magnitudes at 100 Hz were extracted for the sake of clarity and 100 Hz was chosen as it is an information-rich frequency in ECoG recordings. The IDE samples fully covered with polyimide maintained high and stable impedance magnitudes throughout the whole test period of 175 days (plot A in Fig.5.19). Samples with a microhole situated nearby the IDE fingers also maintained high impedance magnitudes without any noticeable decrease (plot B). The IDE samples, fully-protected with polyimide and exposed to steam sterilization (plot C), had comparable impedance magnitudes to non-sterilized samples (compare to plots A and B).

To shine more light to the above exceptionally high water barrier of long-cured in-vacuum BPDA-PPD PI⁶², we investigated thoroughly the differences between the two curing processes and found out that the curing profile of the N₂-furnace (short-cured PI) has a shorter pre-heating stage than the one suggested by the polyimide provider UBE (see Fig.5.14). It is known not sufficient pre-heating just before the final cure peak may result in non-satisfactory properties of the polyimide (but no direct soak test results could be found for this type of polyimide, or any other). From this finding we deduced that the insufficient pre-curing was the reason for the rapid degradation of short-cured polyimide samples. Nevertheless, it did not explain why long-cured in-vacuum polyimide has such an excellent water-barrier.

⁶²The fact that all samples with PI long-cured in-vacuum remained stable within 175 days@60°C, even after being sterilized, was unexplainable to us at that stage of the project.

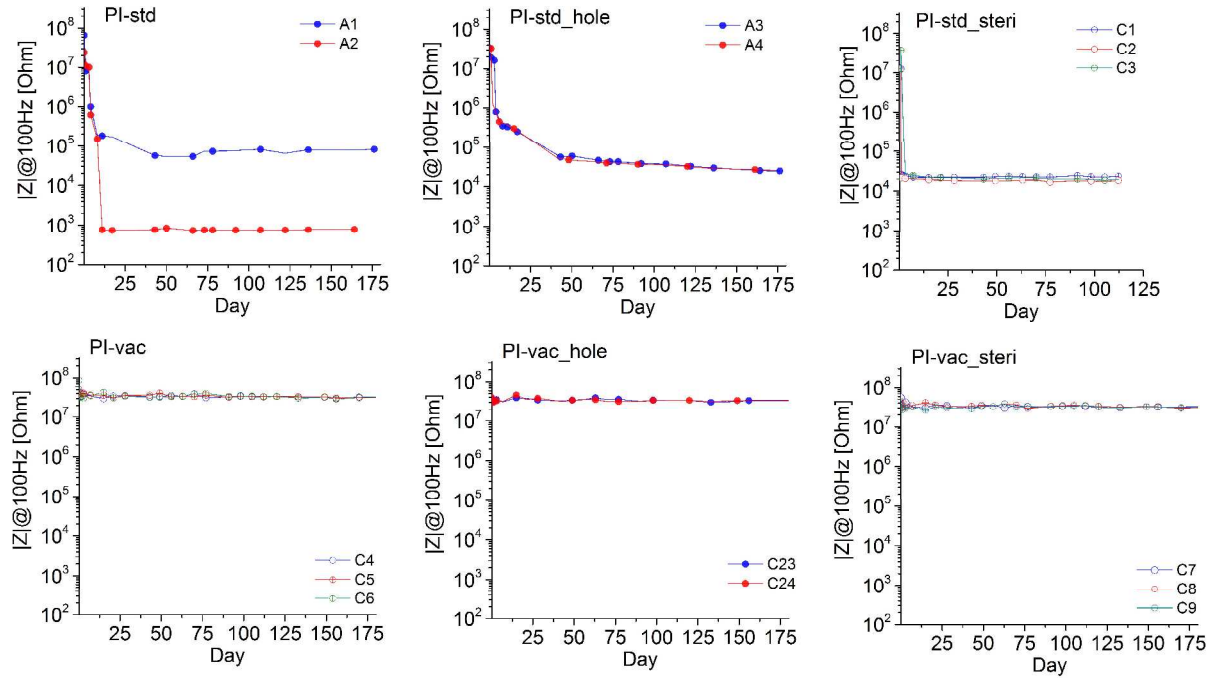


Figure 5.19: Top: Impedance magnitudes obtained at 100Hz for BPDA-PPD polyimide IDE samples cured in a Centrotherm oven under N_2 , (A) IDE samples fully covered with polyimide, (B) IDE samples with a polyimide microhole situated $100\ \mu\text{m}$ away from the outermost IDE finger, (C) IDE samples fully covered with polyimide and steam-sterilized in an autoclave. Bottom: Impedance magnitudes obtained at 100 Hz for BPDA-PPD polyimide IDE samples cured in a wafer-bonding tool within vacuum ambient, (A) IDE samples fully covered with polyimide, (B) IDE samples with a polyimide microhole situated $100\ \mu\text{m}$ away from the outermost IDE finger, (C) IDE samples fully covered with polyimide and steam-sterilized in an autoclave.

The impact of **curing ambient** on long-cured BPDA-PPD polyimide was investigated as follows. As neither lateral diffusion, nor steam sterilization had any noticeable impact on the polyimide coating cured in vacuum ambient (compare top plots in Fig.5.19), samples were cured in wafer-bonding tool in: (1) vacuum, (2) continuous N_2 flow and (3) short chamber-evacuation step to remove potential gas residues, followed by continuous N_2 flow (abbreviated as “evac+ N_2 ”). In each ambient, four types of samples were cured: fully-coated with polyimide, with a microhole, steam-sterilized, and microhole+sterilized. This time, impedance magnitudes were derived at 0.5 Hz, instead of 100 Hz⁶³. Fig.5.20 summarizes the obtained impedance magnitudes from all samples stored in saline@60°C in the course of 200 days. The magnitude

⁶³Early degradation mechanisms are observable at best at lower frequencies; 0.5 Hz was the lowest frequency at which noise-free impedance measurements were recordable with our Ivium measurement system

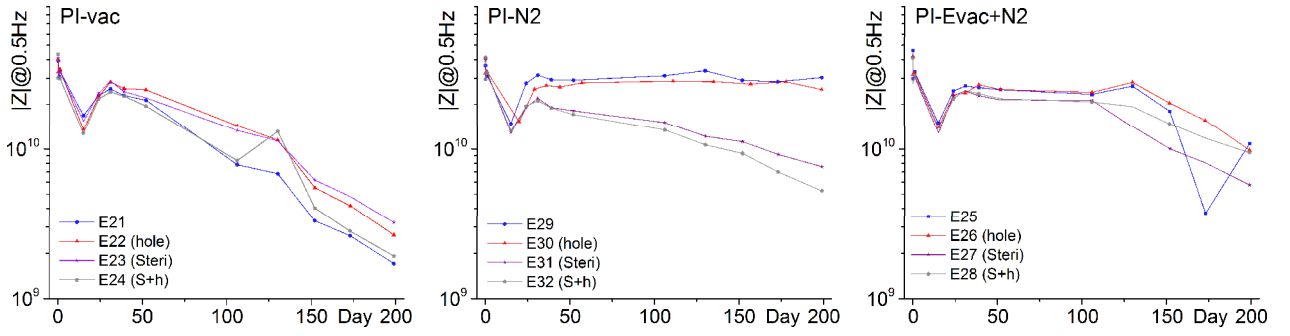


Figure 5.20: Impedance magnitudes at 0.5 Hz obtained from accelerated soak tests: (left) polyimide coatings cured in a vacuum ambient, (middle) in continuous N_2 flow, and (right) “evac+ N_2 ” (C).

values of all samples remained high ($> 10^9 \Omega$) throughout the whole test period, whereas fine differences between the different ambient sets were noticeable: (vacuum ambient, left plot) all impedance magnitudes declined at slow pace since the beginning of the soaking process; (continuous N_2 flow, middle plot) impedance magnitudes split in two groups, the unsterilized samples remained stable in the course of 200 days (samples E29 & E30), while the sterilized ones declined in impedance continuously during the whole test period (samples E31 & E32); (“evac+ N_2 ”, Right plot): all impedances remained stable for 100 days, then all declined at slow pace. From the above accelerated soak measurements it can be deduced that the ambient slightly influences the water-barrier of BPDA-PPD polyimide.

5.3 ATR-FTIR Analysis of Polyimide Foils

BPDA-PPD polyimide samples, cured in Centrotherm oven (short curing) and wafer-bonding tool (long-curing), were analyzed by means of ATR-FTIR spectroscopy. The attenuated total reflection (ATR) spectrum of the samples (1 sample per foil type) are presented in Fig.6.4. Long-cured polyimide has more pronounced FTIR-peaks and hence more specific chemical bonds are present. The later indicates a higher degree of cross-linking during the curing process.

5.4 XRD Analysis of Polyimide Foils

In order to gain more information about the chemical structure, orientation of polymer chains, and water-vapour permeation, we fabricated $5\mu\text{m}$ -thick BPDA-PPD foils and subjected them to XRD analysis.

The BPDA-PPD polyimide foils were fabricated as follows. 4” Silicon wafers were cleaned

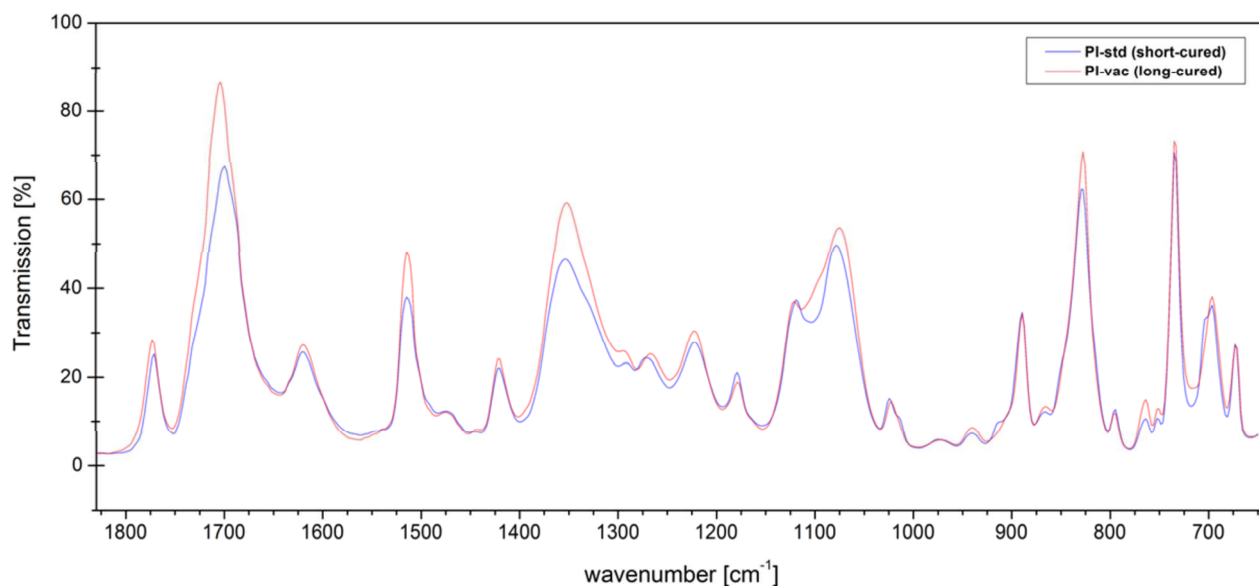


Figure 5.21: ATR-FTIR analysis of long-cured & short-cured BPDA-PPD polyimide foils.

in Caro's acid and their native oxides were stripped with a HF dip. Shortly afterwards the organosilane adhesion promoter VM651 was spin-coated for 60s@4000rpm and backed on a hotplate for 120s@120°C. A 5 μ m-thick U-Varnish-S film (BPDA-PPD) was spin-coated for 40s@3000rpm and soft-backed for 5min@80-120°C & 5min@120°C on a hotplate. Then the wafers were divided into three sets, each set containing 2 wafers, and cured in a Substratbonder SUESS SB6 (long-curing) under the following ambient conditions: (1) vacuum; (2) chamber evacuation + N₂ flow; (3) N₂ flow. After the curing, the wafers were kept for a week in a wafer box. This procedure was applied to enable adhesion loss between the polyimide film and the silicon wafer underneath. Then the polyimide films were manually peeled off the wafers as follows: (1) a razor was used to remove the polyimide residues from the wafer edges, (2) the polyimide foil was cautiously detached from the wafer using a rounded paper piece, whereas the paper piece was inserted between the polyimide and the silicon wafer, and slowly lifting the polyimide off its substrate (essential to guarantee a release without kinking the foil).

Three long-cured BPDA-PPD foils were subjected to XRD analysis, with each foil cured in a different medium. The obtained XRD spectra are shown in Fig.5.23. Both foils cured in N₂ ambient (samples 2 & 3 in Fig.5.23) – with and without chamber evacuation – have three distinct interference peaks at 18°, 21° and 25°. The peak position is related by $\lambda = 2d \sin \theta$ to the inter-distance of the polymeric chain⁶⁴ of the BPDA-PPD polyimide i.e. 0.48 nm, 0.42

⁶⁴As X-rays travel through a sample, they interact with its electrons only (not with the atomic nuclei) so that the electrons will resend the x-ray radiation in circular wavefronts. Away from the sample, X-rays passed through regions of highly ordered atoms (here polymeric chains) will superimpose constructively and give rise to interference peaks.



Figure 5.22: BPDA-PPD polyimide foil peeled off its 4" silicon wafer.

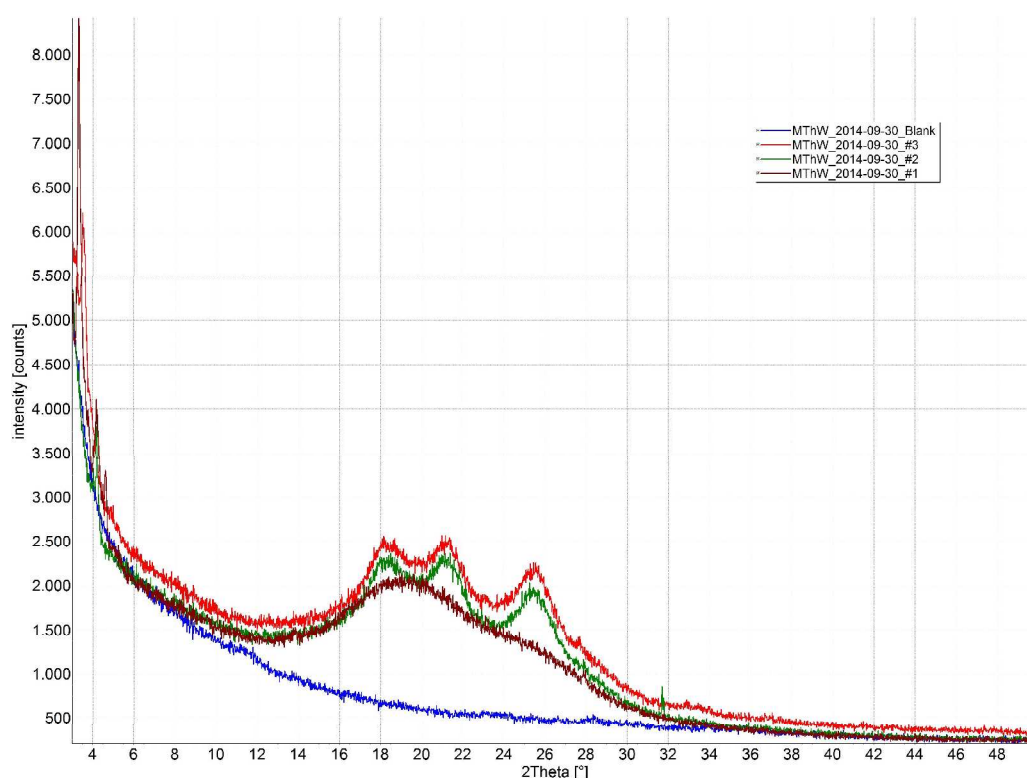


Figure 5.23: XRD spectra of three BPDA-PPD foils ($5\mu\text{m}$ -thick) cured in different ambients: (1) vacuum; (2) chamber evacuation + N_2 , (3) N_2 . The reference signal is denoted as "blank".

nm & 0.34 nm, respectively. Vacuum-cured BPDA-PPD foils do not have the above three distinct peaks, but a broader peak situated directly under the three peaks. Hence, BPDA-PPD polyimide samples cured in N_2 ambient show more pronounced crystalline order than vacuum-cured polyimide.

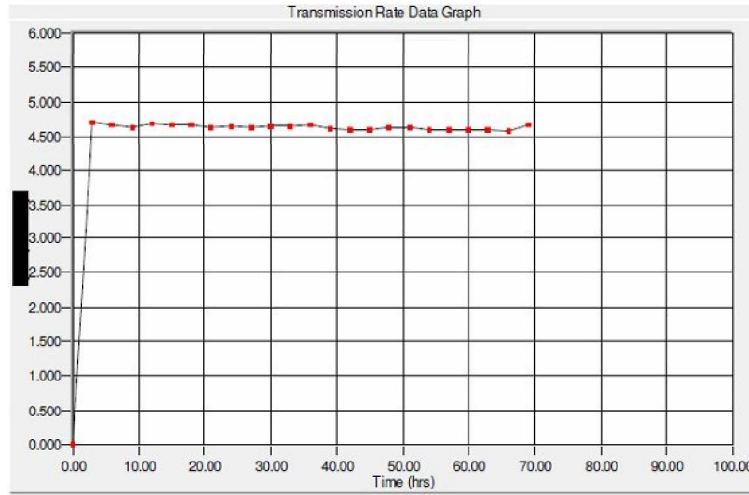


Figure 5.24: Water-vapour transmission rate of foil type B expressed in units of $\text{g} / (\text{m}^2 \cdot \text{day})$, performed at PAUL LIPPKE HANDELS-GMBH.

5.5 Water-Vapour Permeability of Polyimide Foils

A water-vapour permeability test was conducted, whereas $5\mu\text{m}$ -thick polyimide foils were exposed to a flow of water-vapour for several hours at specific temperature and humidity value (23°C , 85 %RH). The water-vapour permeation of BPDA-PPD polyimide foils cured in a wafer-bonding tool in (1) vacuum and (2) evac+N₂ ambient was measured to be $0.017 \text{ g mm/m}^2 \text{ day}$ and $0.022 \text{ g mm/m}^2 \text{ day}$, respectively (2 foils per curing ambient). The obtained water-vapour penetration data are considerably lower than that of parylene C ($0.08 \text{ g mm/m}^2 \text{ day}$ at 37°C , 90%RH [132]). The water-vapour permeation tests were performed externally at PAUL LIPPKE HANDELS-GMBH (www.mocon.eu) at 23°C , 85 %RH.

5.6 Summary

The first ECoG MEA, which was monitored in-vivo, showed signs of possible parasitic short-circuits. These parasitics appeared slowly over time, which was attributed to the diffusion of cerebrospinal liquid into the MEA, especially into the polyimide coating, used as highly-flexible and mechanically-strong insulation thin film. To pinpoint the root-cause of the parasitics, accelerated soak tests were performed on BPDA-PPD polyimide thin-films, spin coated on IDE microstructures. In parallel, parylene films of same thickness were used as reference.

BPDA-PPD polyimide maintained exceptionally high water-barrier in saline (when sufficiently pre-cured), even better than that of parylene C, based on accelerated soak tests performed by IDE micro devices in the span of 170 days and water-vapour permeability tests.

Further, neither lateral diffusion (via a microhole etched into the polyimide film), nor steam-sterilization, had any noticeable impact on the insulation property of BPDA-PPD polyimide films at 100 Hz, an essential frequency in ECoG measurements.

Curing BPDA-PPD films in N₂ ambient proved to be more advantageous for the water-barrier than curing in vacuum. To gain better measurement security, these measurements should be repeated with higher sample size.

We suggest that the excellent water-barrier properties of BPDA-PPD polyimide is caused by the fact that the material is build from polymer chains arranged in a densely-packed “poly-crystalline” blocks, which block water diffusion. This interpretation is strongly supported by XRD, which shows the partial crystallinity of the material: N₂ ambient (in contrast to vacuum) hinders the escape of solvents from polyimide bulk during its curing phase, and these solvents facilitate molecule movement and hence formation of poly-crystalline blocks.

ATR-FTIR analysis of BPDA-PPD polyimide revealed impact of curing ambient/duration on the chemical composition of the polyimide: increased degree of chemical binding and crystalline order will raise the water barrier of polyimide.

The presented accelerated-soak-test results are very useful at isolating the water adhesion and long-term adhesion of the polyimide on Au interface. Unfortunately these results cannot be used to predict the lifetime of an ECoG device since the IDE-samples do not mimic fully an implantable device, for example polyimide-polyimide or polyimide-metal interfaces.

Chapter 6

Long-Term Stability of ECoG MEAs

BPDA-PPD polyimide proved to have good insulation properties when kept soaked in saline for 200 days @ 60°C. To test how this polyimide performs in-vitro and in-vivo, we fabricated MEA samples and kept them soaked in saline for 138 days @ 60°C and implanted an ECoG MEA in a Rhesus monkey. The obtained results reveal how water diffusion degrades of the MEA device and leads to the formation of parasitic short-circuits.

6.1 Long-Term Stability of ECoG MEA In-Vitro

Three types of ECoG MEAs samples were fabricated¹, as illustrated in Fig.6.1: to investigate the long-term stability of long-cured polyimide and compare it to short-cured polyimide, as well as to test the influence of the fixating material around the connectors (GE680 epoxy or UHU epoxy). The intention of subjecting ECoG MEAs to accelerated soak test was to monitor both volume diffusion through the polyimide coating and interfacial diffusion along polyimide-polyimide and polyimide-metal interfaces (see Fig.6.2). The samples were kept in a convection oven at 60°C and taken out for electrical measurements. The impedances between the MEA electrodes were recorded by an NI multiplexer and an IVIUM impedance meter² (see Fig.6.3).

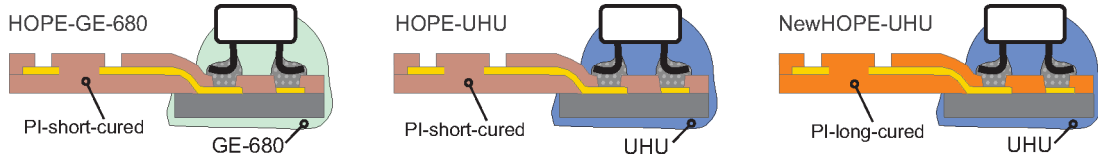


Figure 6.1: ECoG MEA samples used for accelerated soak tests.

¹For detailed fabrication flow is presented in Fig.4.12

²Same hardware was used for the characterization of the MEA electrodes in Chapter 4.5. For more details on the measurement set-up refer to Appendix.

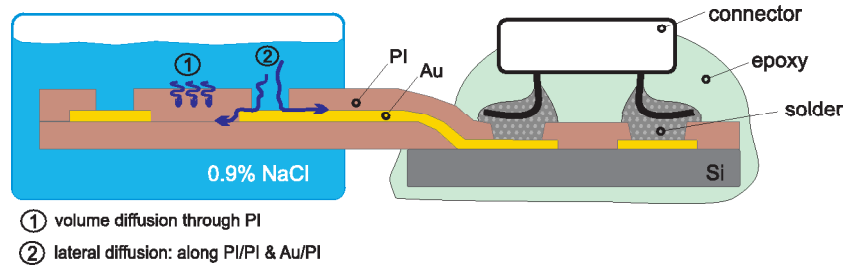


Figure 6.2: Saline diffusion into ECoG MEA: (1) polyimide absorbs saline molecules; (2) saline can access a PI/PI interface or a metal/PI interface and thus cause short-circuits.

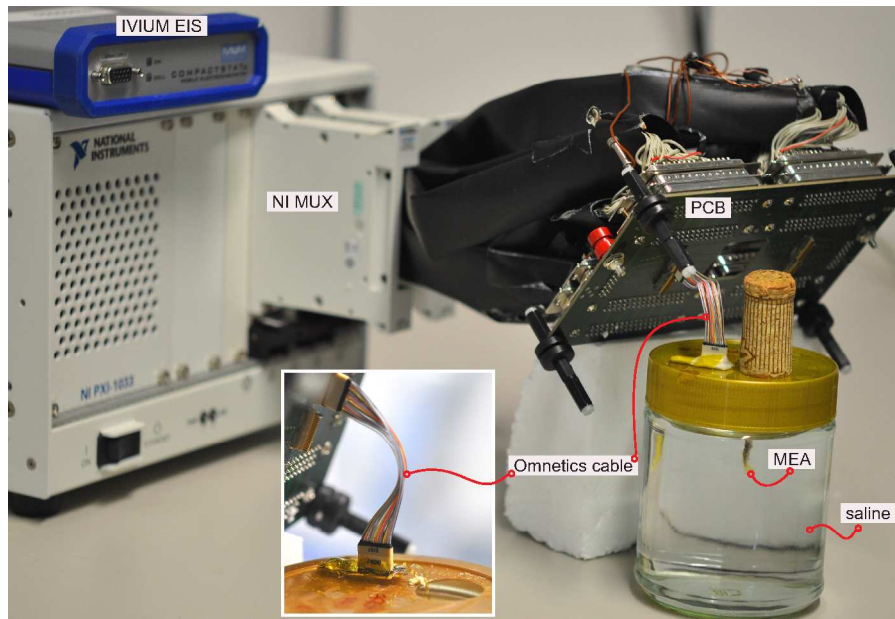


Figure 6.3: Accelerated soak test: an ECoG MEA soaked in saline, its impedances are monitored by NI multiplexer (MUX) and impedance meter (IVIUM EIS).

The obtained impedance magnitudes⁵ are plotted in Fig.6.4. Additionally, the 100Hz impedance magnitudes⁶ were extracted to better compare each MEA sample soak performance and are shown in Fig.6.5.

The long-cured polyimide MEA maintained highest impedance magnitudes from test begin until 138 days in saline for 200 days @ 60°C, as compared to short-cured polyimide⁷. This finding matches the results obtained from IDE-samples soaked in saline @ 60°C, as presented

⁵of all 300 μ m-diameter electrodes only with respect to the MEA's own reference electrode. The electrodes under test were chosen because in connector A (which we used for this test) most electrode pads were linked to this type of electrodes (see Fig.E.6)

⁶100Hz is essential frequency in ECoG recordings

⁷One ought to keep in mind that these results are not true impedances but their shunted values, as shown in the Appendix in Fig.E.5.

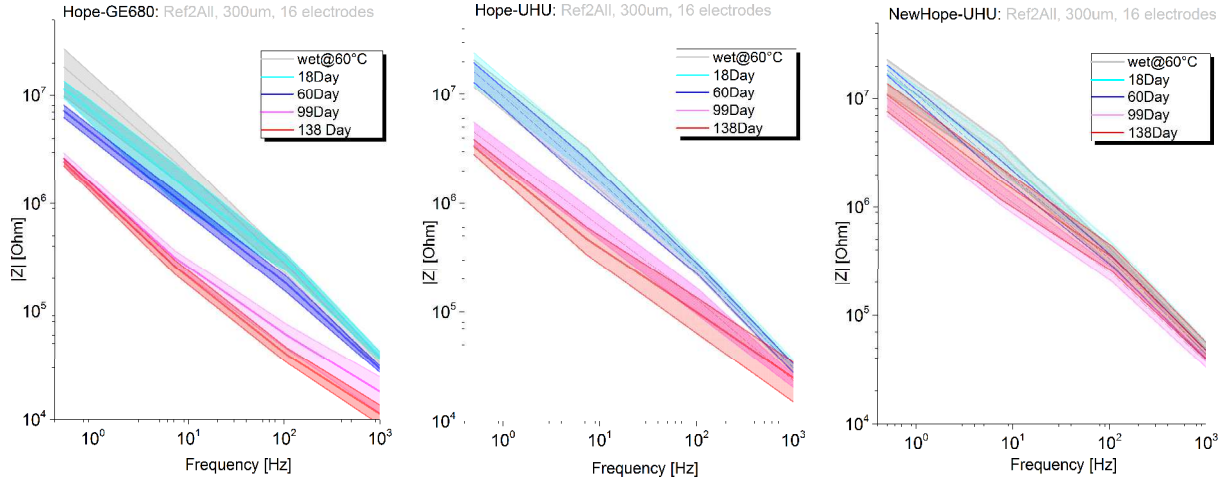


Figure 6.4: Accelerated soak-test results: Impedance magnitudes, measured between every 300um-electrode from connector A and the ECoG reference electrode³ of shortly-cured PI and GE-680 epoxy (left); shortly-cured PI and UHU epoxy (middle) and long-cured PI⁴ (right).

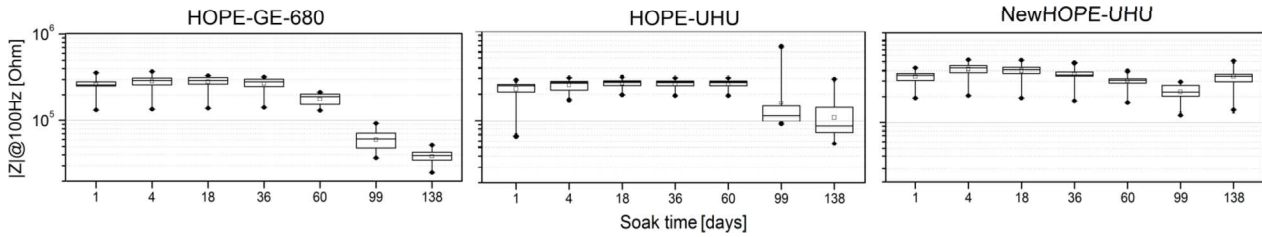


Figure 6.5: The 100Hz-impedance magnitudes extracted from the plots of Fig.6.4 of three different MEA samples (see Fig.6.1).

in a previous Chapter. Further, after 100 soaking days, the 100-Hz impedance magnitudes of the short-cured polyimide samples decreased to $4 \cdot 10^5 \Omega$ and $0.2 \cdot 10^6 \Omega$, while the long-cure polyimide sample maintained slightly higher value of $1.3 \cdot 10^6 \Omega$, but began decreasing slightly after the 60th soak day, i.e. a probable indicator for water diffusion along PI-PI or PI-Au-PI interfaces⁸. Besides, the adhesive used around the connectors, and its adhesion to the MEA, might have slight influence on the long-term stability of the MEAs (compare left and middle plot in Fig.6.4). In outlook, the sample size needs to be increased for the sake of statistics.

⁸The IDE-samples coated with long-cured polyimide remained stable throughout 170 soak days.

6.2 Long-Term Stability of ECoG MEA In-Vivo

An ECoG MEA was fabricated, relying on long-cured polyimide as a coating material. This MEA was implanted in a Rhesus monkey. The implantation and all in-vivo recordings were performed by Heiko Stemmann at Brain Research Institute, University of Bremen. The electrical performance of the MEA's electrodes was monitored for 12 months. The number of working electrodes is presented in Fig.6.6, whereas the data from the first ECoG MEA, where first parasitic short-circuits were observed, was taken as a reference. The usage of BPDA-PPD polyimide and optimized electrical contact within the connector region (Silicon-metal pad⁹), accounted for 97% working electrical connections at the onset of in-vivo recordings. This number decreased to ca. 50% after 1 year of implantation. This decrease is caused most probably by diffusion of cerebrospinal liquid along interfaces of the MEA, such as polyimide-polyimide or polyimide-metal interfaces, as similar degradation was observed during accelerated soak tests in the previous Section.

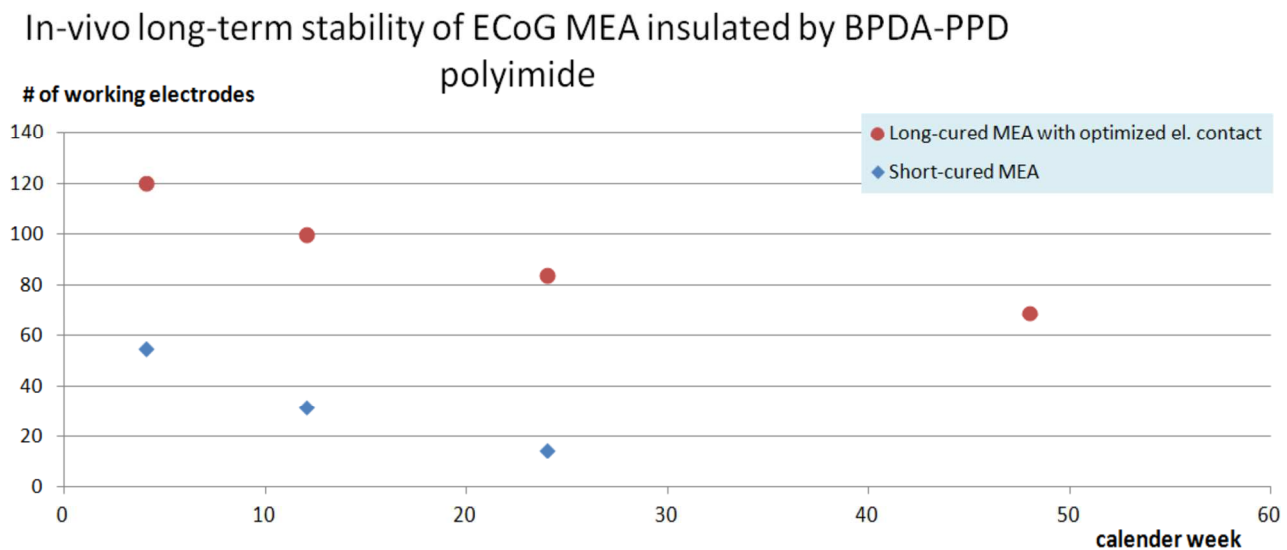


Figure 6.6: In-vivo long-term performance of ECoG MEA, with BPDA-PPD polyimide serving as flexible insulation material. Long-cured MEAs show higher stability than short-cured ones.

⁹See Fig.4.10.C

Chapter 7

Summary & Outlook

”With Love you will sell and with Love
you will buy.”

Petar Danov

When a ray of light falls on the retina, it stirs a cascade of electrochemical impulses within series of neuronal populations. When during this light perception attention is paid to a specific item, highly synchronized electrochemical impulses are generated within the visual cortex. Recording such synchronized neuronal activities from the cortical surface can serve as input signals for attention-based BCIs and provide a virtual keyboard as fast communication means for locked-in persons. This Thesis proposed an ECoG MEA which can serve as interface between the cortical surface and pre-amplifiers of attention-based BCI. This ECoG MEA is capable of recording ECoG waveforms with high spatial resolution, has stable electrical contact to external connectors and improved high-water-barrier insulation.

Stable electrical contact towards external electronics was realized by the flex-rigid mechanical design of the MEA. Its rigid Si/SiO₂/Ti/Au solder pad island, monolithically integrated within the MEA, provided a solid platform for the soldering of miniature Omnetics connectors. Rigid solder joints made of Si/SiO₂/Ti/Au were more reliable than Si/SiO₂/PI/Ti/Au ones. Further, ECoG MEA was characterized in-vitro and the obtained impedance magnitudes of its recording electrodes correlated to values reported in literature. The MEA was characterized in-vivo: electrophysiological field potentials were successfully recorded from a Rhesus macaque’s primary visual cortex. Larger electrodes recorded signals with greater spectral power in the gamma band. Further, using a skull-facing electrode provided signals with greater power than those obtained using a common average referencing technique.

However, the ECoG MEA, which was monitored in-vivo, showed also signs of possible parasitic short-circuits. These parasitics appeared slowly over time, which was attributed to the

diffusion of cerebrospinal liquid into the MEA. To pinpoint the root-cause of these parasitics, accelerated soak tests were performed on BPDA-PPD polyimide thin-films, spin coated on IDE microstructures, whereas parylene served as reference. BPDA-PPD polyimide maintained exceptionally high water-barrier in saline (when sufficiently pre-cured), even better than that of parylene C. Steam sterilization did not have any observable impact on the insulation property of the polyimide films. XRD measurements revealed that BPDA-PPD polyimide films cured in N_2 ambient have higher crystallinity than when cured in vacuum. Next, an ECoG MEA was microfabricated by using vacuum-cured¹ BPDA-PPD polyimide. The microdevice was steam sterilized and kept stored in saline. First signs of insulation degradation were recorded after 60 days @60°C, which was attributed mostly to diffusion of saline molecules along polyimide-polyimide and gold-polyimide interfaces. Finally, such an ECoG MEA was implanted in a Rhesus Macaque. After 1 year of implantation the number of functioning electrodes decreased to ca. 50%, attributed to diffusion of cerebrospinal liquid along material interfaces.

This Work described a microfabrication method for the reliable assembly of electrical connectors and investigations on the electrical insulation properties of a polyimide in vitro and in vivo. And yet, ECoG MEAs need to be miniaturized to a level at which they can become fully implantable devices, reach a long-term stability in vivo for at least 10 years, and attain higher signal-to-noise ratio.

The signal-to-noise ratio can be increased by coating the ECoG electrodes with an electrically conductive polymer (PEDOT). Its impedance, when immersed in water, is much lower than that of metals. A. Schander et. al [133], among several other research groups, demonstrated the increase of signal-to-noise ratio by coating the electrodes of micro-needles, several times smaller in area than typical ECoG electrodes, and testing their performance in vivo.

The long-term stability of ECoG MEAs can be slightly prolonged by increasing the adhesion between the flexible insulation material and the metal traces, as suggested in [134] for polyimide and in [95] for parylene C, among many other research groups.

A fully implantable ECoG MEA would require the integration of analog pre-amplifiers, digital signal-processing and electronics for wireless signal transmission and energy supply. B. Mimoun et al. [43] suggested a microfabrication method for the integration of electronic chips into flexible devices. D. Rotermund et al. [135] has developed an wireless ECoG electronic platform, based on printed-circuit-board fabrication technology. M. Yin et al. [136] has realized a wireless neural electronic platform, which is hermetically sealed and semi-implantable.

In summary, substantial amount of work was dedicated to advance neural implants to the state of mature medical applications. Nevertheless, we are far from coming in close proximity

¹At that point in time it was not obvious that N_2 -cured polyimide performs better than vacuum-cured one.

to this aim. Major barriers are reaching a highly miniaturized state of the device to make it fully implantable and at the same time providing enough neural information outwards and enough supply energy inwards, not mentioning long-term stability of at least 10 years.

At the onset of this Work, my aspiration to advance the development of neural implants was sourced by the hope that one day such devices would be able to assist in the healing process of serious mental diseases such as schizophrenia. To come close to this, we need to have the courage to open our minds and hearts to unthinkable solutions, which might seem fully ridiculous at first glance, but most probably bare a hidden treasure [137], and then follow our intuition.

Bibliography

- [1] Mark Wm Dubin. *How the brain works*. John Wiley & Sons, 2013.
- [2] Isaac Asimov. In the game of energy and thermodynamics you can't even break even: Journal of smithsonian institue. Smithsonian 1 (August), p. 10., 1970.
- [3] Michael A Arbib. *The handbook of brain theory and neural networks*. MIT press, 2003.
- [4] David Rotermund, Udo A Ernst, Sunita Mandon, Katja Taylor, Yulia Smiyukha, Andreas K Kreiter, and Klaus R Pawelzik. Toward high performance, weakly invasive brain computer interfaces using selective visual attention. *The Journal of Neuroscience*, 33(14):6001–6011, 2013.
- [5] Eberhard E Fetz. Volitional control of neural activity: implications for brain–computer interfaces. *The Journal of physiology*, 579(3):571–579, 2007.
- [6] Kabellose erfassung lokaler feldpotentiale und elektrische stimulation der großhirnrinde für medizinische diagnostik und neuroprothetik, accessed 23 august 2017, www.kalomed.info.
- [7] E Goldstein. *Sensation and perception*. Cengage Learning, 2013.
- [8] Richard Szeliski. *Computer vision: algorithms and applications*. Springer, 2010.
- [9] Eric R Kandel, James H Schwartz, Thomas M Jessell, et al. *Principles of neural science*, volume 4. McGraw-Hill New York, 2000.
- [10] David H Hubel. *Eye, brain, and vision*. Scientific American Library/Scientific American Books, 1995.
- [11] Gyorgy Buzsaki. *Rhythms of the Brain*. Oxford University Press, 2006.
- [12] Daniel J DiLorenzo and Joseph D Bronzino. *Neuroengineering, Chapter 12*. CRC Press, 2007.

- [13] Frank H. Guenther & Jonathan S. Brumberg. Unchained mind, January 1 2013.
- [14] Leigh R Hochberg, Daniel Bacher, Beata Jarosiewicz, Nicolas Y Masse, John D Simeral, Joern Vogel, Sami Haddadin, Jie Liu, Sydney S Cash, Patrick van der Smagt, et al. Reach and grasp by people with tetraplegia using a neurally controlled robotic arm. *Nature*, 485(7398):372–375, 2012.
- [15] Andreas K Kreiter. Wie wir aus einer flut von informationen das wichtigste herausfiltern: die neurobiologie der aufmerksamkeit, July, 2006.
- [16] Richard D Wright. *Visual attention*. Oxford University Press, 1998.
- [17] Jaakko Malmivuo and Robert Plonsey. *Bioelectromagnetism: principles and applications of bioelectric and biomagnetic fields*. Oxford University Press, 1995.
- [18] Gerwin Schalk and Eric C Leuthardt. Brain-computer interfaces using electrocorticographic signals. *Biomedical Engineering, IEEE Reviews in*, 4:140–154, 2011.
- [19] Peyman Adjamian. The application of electro-and magneto-encephalography in tinnitus research—methods and interpretations. *Frontiers in neurology*, 5, 2014.
- [20] Philipp Berens, Georgios A Keliris, Alexander S Ecker, Nikos K Logothetis, and Andreas S Tolias. Feature selectivity of the gamma-band of the local field potential in primate primary visual cortex. *Frontiers in neuroscience*, 2(2):199, 2008.
- [21] Rodrigo Quian Quiroga and Stefano Panzeri. *Principles of neural coding*. CRC Press, 2013.
- [22] Jonathan Wolpaw and Elizabeth Winter Wolpaw. *Brain-computer interfaces: principles and practice*. Oxford University Press, 2011.
- [23] K Taylor, S Mandon, WA Freiwald, and AK Kreiter. Coherent oscillatory activity in monkey area v4 predicts successful allocation of attention. *Cerebral Cortex*, 15(9):1424–1437, 2005.
- [24] Laura Freberg. *Discovering biological psychology*. Cengage Learning, 2009.
- [25] Dirk Schubert, Jochen F Staiger, Nichole Cho, Rolf Kötter, Karl Zilles, and Heiko J Luhmann. Layer-specific intracolumnar and transcolumar functional connectivity of layer v pyramidal cells in rat barrel cortex. *The Journal of Neuroscience*, 21(10):3580–3592, 2001.

- [26] John Milton and Peter Jung. *Epilepsy as a dynamic disease*. Springer Science & Business Media, 2002.
- [27] Juri Kropotov. *Quantitative EEG, event-related potentials and neurotherapy*. Academic Press, 2010.
- [28] Ivan Izquierdo. The art of forgetting. In *The Art of Forgetting*, pages 7–60. Springer, 2015.
- [29] György Buzsáki, Costas A Anastassiou, and Christof Koch. The origin of extracellular fields and currents—eeg, ecog, lfp and spikes. *Nature reviews neuroscience*, 13(6):407–420, 2012.
- [30] Ellen Covey and Matt Carter. *Basic Electrophysiological Methods*. Oxford University Press, 2015.
- [31] Carsten Mehring, Jörn Rickert, Eilon Vaadia, Simone Cardoso de Oliveira, Ad Aertsen, and Stefan Rotter. Inference of hand movements from local field potentials in monkey motor cortex. *Nature neuroscience*, 6(12):1253–1254, 2003.
- [32] Eric C Leuthardt, Gerwin Schalk, Jonathan R Wolpaw, Jeffrey G Ojemann, and Daniel W Moran. A brain–computer interface using electrocorticographic signals in humans. *Journal of neural engineering*, 1(2):63, 2004.
- [33] David Rotermund, Katja Taylor, Udo A Ernst, Andreas K Kreiter, and Klaus R Pawelzik. Attention improves object representation in visual cortical field potentials. *The Journal of Neuroscience*, 29(32):10120–10130, 2009.
- [34] Robert P Vertes and Robert W Stackman. *Electrophysiological recording techniques*. Humana Press, 2011.
- [35] Paul L Nunez, Ramesh Srinivasan, Andrew F Westdorp, Ranjith S Wijesinghe, Don M Tucker, Richard B Silberstein, and Peter J Cadusch. Eeg coherency: I: statistics, reference electrode, volume conduction, laplacians, cortical imaging, and interpretation at multiple scales. *Electroencephalography and clinical neurophysiology*, 103(5):499–515, 1997.
- [36] Paul S Addison. *The illustrated wavelet transform handbook: introductory theory and applications in science, engineering, medicine and finance*. CRC Press, 2002.
- [37] John L Semmlow and Benjamin Griffel. *Biosignal and medical image processing*. CRC press, 2014.

- [38] MRC Cognition and Brain Sciences Unit. Introduction to eeg and meg. imaging.mrc-cbu.cam.ac.uk/meg/IntroEEGMEG.
- [39] Sami Franssila. *Front Matter*. Wiley Online Library, 2004.
- [40] Marc J Madou. *Fundamentals of microfabrication: the science of miniaturization*. CRC press, 2002. p.32.
- [41] Joachim N Burghartz, Wolfgang Appel, Christine Harendt, Horst Rempp, Harald Richter, and Martin Zimmermann. Ultra-thin chip technology and applications, a new paradigm in silicon technology. *Solid-State Electronics*, 54(9):818–829, 2010.
- [42] R Dekker, M Dumling, J-H Fock, O Gourhant, C Jonville, TM Michielsen, H Pohlmann, W Schnitt, and AMH Tombeur. A 10 μm thick rf-id tag for chip-in-paper applications. In *Bipolar/BiCMOS Circuits and Technology Meeting, 2005. Proceedings of the*, pages 18–21. IEEE, 2005.
- [43] Benjamin Mimoun, Vincent Henneken, and Ronald Dekker. Flex-to-rigid (f2r): A novel ultra-flexible technology for smart invasive medical instruments. In *Stretchable Electronics and Conformal Biointerfaces, MRS Symp. Proc. 1271E*, 2010.
- [44] Juan Ordonez, Martin Schuettler, Christian Boehler, Tim Boretius, and Thomas Stieglitz. Thin films and microelectrode arrays for neuroprosthetics. *MRS bulletin*, 37(06):590–598, 2012.
- [45] Yong-Ak Song, Ahmed MS Ibrahim, Amr N Rabie, Jongyoon Han, and Samuel J Lin. Microfabricated nerve–electrode interfaces in neural prosthetics and neural engineering. *Biotechnology and Genetic Engineering Reviews*, 29(2):113–134, 2013.
- [46] Taylor Ware, Dustin Simon, Robert L Rennaker, and Walter Voit. Smart polymers for neural interfaces. *Polymer Reviews*, 53(1):108–129, 2013.
- [47] Jonathan Viventi, Dae-Hyeong Kim, Leif Vigeland, Eric S Frechette, Justin A Blanco, Yun-Soung Kim, Andrew E Avrin, Vineet R Tiruvadi, Suk-Won Hwang, Ann C Vanleer, et al. Flexible, foldable, actively multiplexed, high-density electrode array for mapping brain activity in vivo. *Nature neuroscience*, 14(12):1599–1605, 2011.
- [48] Leo A Bullara, William F Agnew, Ted GH Yuen, Skip Jacques, and Robert H Pudenz. Evaluation of electrode array material for neural prostheses. *Neurosurgery*, 5(6):681–686, 1979.

- [49] Tim Blakely, Kai J Miller, Stavros P Zanos, Rajesh PN Rao, and Jeffrey G Ojemann. Robust, long-term control of an electrocorticographic brain-computer interface with fixed parameters. *Neurosurgical focus*, 27(1):E13, 2009.
- [50] Spencer S Kellis, Paul A House, Kyle E Thomson, Richard Brown, and Bradley Greger. Human neocortical electrical activity recorded on nonpenetrating microwire arrays: applicability for neuroprostheses. *Neurosurgical focus*, 27(1):E9, 2009.
- [51] Birthe Rubehn, Conrado Bosman, Robert Oostenveld, Pascal Fries, and Thomas Stieglitz. A mems-based flexible multichannel ecog-electrode array. *Journal of neural engineering*, 6(3):036003, 2009.
- [52] P Ledochowitsch, RJ Félus, RR Gibboni, A Miyakawa, S Bao, and MM Maharbiz. Fabrication and testing of a large area, high density, parylene mems μ ecog array. In *Micro Electro Mechanical Systems (MEMS), 2011 IEEE 24th International Conference on*, pages 1031–1034. IEEE, 2011.
- [53] Dong-Hyun Baek, Chang-Hee Han, Ha-Chul Jung, Seon Min Kim, Chang-Hwan Im, Hyun-Jik Oh, James Jungho Pak, and Sang-Hoon Lee. Soldering-based easy packaging of thin polyimide multichannel electrodes for neuro-signal recording. *Journal of Micromechanics and Microengineering*, 22(11):115017, 2012.
- [54] Yasuhiro X Kato, Katuhiro Maki, Shigeto Furukawa, and Makio Kashino. A photosensitive polyimide based method for an easy fabrication of multichannel neural electrodes. In *Engineering in Medicine and Biology Society, 2008. EMBS 2008. 30th Annual International Conference of the IEEE*, pages 5802–5805. IEEE, 2008.
- [55] Jiwan Kim, J Adam Wilson, and Justin C Williams. A cortical recording platform utilizing μ ecog electrode arrays. In *Engineering in Medicine and Biology Society, 2007. EMBS 2007. 29th Annual International Conference of the IEEE*, pages 5353–5357. IEEE, 2007.
- [56] Ricardo Starbird, Wolfgang Bauhofer, Mario Meza-Cuevas, and Wolfgang H Krautschneider. Effect of experimental factors on the properties of pedot- π apss galvanostatically deposited from an aqueous micellar media for invasive electrodes. In *Biomedical Engineering International Conference (BMEiCON), 2012*, pages 1–5. IEEE, 2012.
- [57] Wei Wang, Alan D Degenhart, Jennifer L Collinger, Ramana Vinjamuri, Gustavo P Sudre, P David Adelson, Deborah L Holder, Eric C Leuthardt, Daniel W Moran, Michael L Boninger, et al. Human motor cortical activity recorded with micro-ecog electrodes,

- during individual finger movements. In *Engineering in Medicine and Biology Society, 2009. EMBC 2009. Annual International Conference of the IEEE*, pages 586–589. IEEE, 2009.
- [58] Matthew J Nelson and Pierre Pouget. Physical model of coherent potentials measured with different electrode recording site sizes. *Journal of neurophysiology*, 107(5):1291–1300, 2012.
 - [59] CA Gutierrez, C Lee, B Kim, and E Meng. Epoxy-less packaging methods for electrical contact to parylene-based flat flexible cables. In *Solid-State Sensors, Actuators and Microsystems Conference (TRANSDUCERS), 2011 16th International*, pages 2299–2302. IEEE, 2011.
 - [60] Keekeun Lee, Amarjit Singh, Jiping He, Stephen Massia, Bruce Kim, and Gregory Raupp. Polyimide based neural implants with stiffness improvement. *Sensors and Actuators B: Chemical*, 102(1):67–72, 2004.
 - [61] Cinzia Metallo, Robert D White, and Barry A Trimmer. Flexible parylene-based microelectrode arrays for high resolution emg recordings in freely moving small animals. *Journal of neuroscience methods*, 195(2):176–184, 2011.
 - [62] Sami Myllymaa, Katja Myllymaa, Hannu Korhonen, Juha Töyräs, Juha E Jääskeläinen, Kaj Djupsund, Heikki Tanila, and Reijo Lappalainen. Fabrication and testing of polyimide-based microelectrode arrays for cortical mapping of evoked potentials. *Biosensors and Bioelectronics*, 24(10):3067–3072, 2009.
 - [63] Dong-Hyun Baek, Ji Soo Park, Eun-Joong Lee, Su Jung Shin, Jin-Hee Moon, James Jungho Pak, and Sang-Hoon Lee. Interconnection of multichannel polyimide electrodes using anisotropic conductive films (acfs) for biomedical applications. *Biomedical Engineering, IEEE Transactions on*, 58(5):1466–1473, 2011.
 - [64] Fan Wu, Lee Tien, Fujun Chen, David Kaplan, Joshua Berke, and Euisik Yoon. A multi-shank silk-backed parylene neural probe for reliable chronic recording. In *Solid-State Sensors, Actuators and Microsystems (TRANSDUCERS & EUROSENSORS XXVII), 2013 Transducers & Eurosensors XXVII: The 17th International Conference on*, pages 888–891. IEEE, 2013.
 - [65] E Fiedler, J Ordonez, and T Stieglitz. Modular assembly of flexible thin-film electrode arrays enabled by a laser-structured ceramic adapter. In *Neural Engineering (NER), 2013 6th International IEEE/EMBS Conference on*, pages 657–660. IEEE, 2013.

- [66] Patrick J Rousche, David S Pellinen, David P Pivin Jr, Justin C Williams, Rio J Vetter, et al. Flexible polyimide-based intracortical electrode arrays with bioactive capability. *Biomedical Engineering, IEEE Transactions on*, 48(3):361–371, 2001.
- [67] André Mercanzini, Karen Cheung, Derek L Buhl, Marc Boers, Anne Maillard, Philippe Colin, Jean-Charles Bensadoun, Arnaud Bertsch, and Philippe Renaud. Demonstration of cortical recording using novel flexible polymer neural probes. *Sensors and Actuators A: Physical*, 143(1):90–96, 2008.
- [68] Viswanath Sankar, Justin C Sanchez, Edward McCumiskey, Nagid Brown, Curtis R Taylor, Gregory J Ehlert, Henry A Sodano, and Toshikazu Nishida. A highly compliant serpentine shaped polyimide interconnect for front-end strain relief in chronic neural implants. *Frontiers in neurology*, 4, 2013.
- [69] R Dekker, S Braam, V Henneken, A van der Horst, S Khoshfetrat Pakazad, M Louwerse, B van Meer, B Mimoun, A Savov, and A van de Stolpe. Living chips and chips for the living. In *Bipolar/BiCMOS Circuits and Technology Meeting (BCTM), 2012 IEEE*, pages 1–9. IEEE, 2012.
- [70] Liang Guo and Stephen P DeWeerth. Implementation of integratable pdms-based conformable microelectrode arrays using a multilayer wiring interconnect technology. In *Engineering in Medicine and Biology Society, 2009. EMBC 2009. Annual International Conference of the IEEE*, pages 1619–1622. IEEE, 2009.
- [71] William D Callister and David G Rethwisch. *Materials science and engineering: an introduction*, volume 7. Wiley New York, 2007.
- [72] Volker Lehmann. *Electrochemistry of silicon*, volume 16. Wiley-VCH Verlag GmbH Weinheim, Germany, 2002.
- [73] Shekhar Bhansali and Abhay Vasudev. *MEMS for biomedical applications*. Elsevier, 2012.
- [74] CY Shih, Theodore A Harder, and Yu-Chong Tai. Yield strength of thin-film parylene-c. *Microsystem Technologies*, 10(5):407–411, 2004.
- [75] Ping Du, Hongbing Lu, and Xin Zhang. Measuring the young’s relaxation modulus of pdms using stress relaxation nanoindentation. In *MRS Proceedings*, volume 1222, pages 1222–DD02. Cambridge Univ Press, 2009.
- [76] University of cambridge, material selection and processing, accessed on 25.08.2017, www-materials.eng.cam.ac.uk/mpsite/physics/introduction.

- [77] Roger T Fenner and JN Reddy. *Mechanics of solids*. CRC Press, 1991.
- [78] Dae-Hyeong Kim, Jonathan Viventi, Jason J Amsden, Jianliang Xiao, Leif Vigeland, Yun-Soung Kim, Justin A Blanco, Bruce Panilaitis, Eric S Frechette, Diego Contreras, et al. Dissolvable films of silk fibroin for ultrathin conformal bio-integrated electronics. *Nature materials*, 9(6):511–517, 2010.
- [79] WC Bolton. *Mechanical science*. John Wiley & Sons, 2013.
- [80] Krishan K Chawla. *Composite materials: science and engineering*. Springer, 2012.
- [81] Edward McCafferty. *Introduction to corrosion science*. Springer, 2010.
- [82] Elena Tolstosheeva, Víctor Gordillo-González, Volker Biefeld, Ludger Kempen, Sunita Mandon, Andreas K Kreiter, and Walter Lang. A multi-channel, flex-rigid ecog micro-electrode array for visual cortical interfacing. *Sensors*, 15(1):832–854, 2015.
- [83] Subhash Chandra Bhatnagar. *Neuroscience for the study of communicative disorders*. Lippincott Williams & Wilkins, 2002.
- [84] Jonathan Wolpaw and Elizabeth Winter Wolpaw. *Brain-computer interfaces: principles and practice*. BCIs that use electrocorticographic activity, Gerwin Schalk, Oxford University Press, 2011.
- [85] Olga F Lazareva, Toru Shimizu, and Edward A Wasserman. *How animals see the world: comparative behavior, biology, and evolution of vision*. Oxford University Press, 2012.
- [86] William CO Mara. *Liquid crystal flat panel displays: manufacturing science & technology*. Springer Science & Business Media, 2012.
- [87] LA Geddes. Historical evolution of circuit models for the electrode-electrolyte interface. *Annals of biomedical engineering*, 25(1):1–14, 1997.
- [88] Pedro E Maldonado, Stacia Friedman-Hill, and Charles M Gray. Dynamics of striate cortical activity in the alert macaque: II. fast time scale synchronization. *Cerebral Cortex*, 10(11):1117–1131, 2000.
- [89] Elena Tolstosheeva, Víctor Gordillo-González, Volker Biefeld, Ludger Kempen, Sunita Mandon, Andreas K Kreiter, and Walter Lang. A multi-channel, flex-rigid ecog micro-electrode array for visual cortical interfacing. *Sensors*, 15(1):832–854, 2015.

- [90] John D Yeager, Derrick J Phillips, David M Rector, and David F Bahr. Characterization of flexible ecog electrode arrays for chronic recording in awake rats. *Journal of neuroscience methods*, 173(2):279–285, 2008.
- [91] Patrick J Rousche and Richard A Normann. Chronic recording capability of the utah intracortical electrode array in cat sensory cortex. *Journal of neuroscience methods*, 82(1):1–15, 1998.
- [92] JD Simeral, SP Kim, MJ Black, JP Donoghue, and LR Hochberg. Neural control of cursor trajectory and click by a human with tetraplegia 1000 days after implant of an intracortical microelectrode array. *Journal of neural engineering*, 8(2):025027, 2011.
- [93] Swarup Bhunia, Steve Majerus, and Mohamad Sawan. *Implantable Biomedical Microsystems: Design Principles and Applications*. Elsevier, 2015.
- [94] Specialty coating systems, accessed on 25.08.2017, scscoatings.com.
- [95] John P Seymour, Yaseen M Elkasabi, Hsien-Yeh Chen, Joerg Lahann, and Daryl R Kipke. The insulation performance of reactive parylene films in implantable electronic devices. *Biomaterials*, 30(31):6158–6167, 2009.
- [96] Jui-Mei Hsu. Investigation of amorphous silicon carbide: hydrogen and parylene-c thin films as encapsulation materials for neural interface devices. 2008.
- [97] Rene Patrick Von Metzen and Thomas Stieglitz. The effects of annealing on mechanical, chemical, and physical properties and structural stability of parylene c. *Biomedical microdevices*, 15(5):727–735, 2013.
- [98] Wen Li, Damien C Rodger, Ellis Meng, James D Weiland, Mark S Humayun, and Yu-Chong Tai. Flexible parylene packaged intraocular coil for retinal prostheses. In *Microtechnologies in Medicine and Biology, 2006 International Conference on*, pages 105–108. IEEE, 2006.
- [99] Christina Hassler, Rene P von Metzen, Patrick Ruther, and Thomas Stieglitz. Characterization of parylene c as an encapsulation material for implanted neural prostheses. *Journal of Biomedical Materials Research Part B: Applied Biomaterials*, 93(1):266–274, 2010.
- [100] XZ Xie, L Rieth, P Tathireddy, and F Solzbacher. Long-term in-vitro investigation of parylene-c as encapsulation material for neural interfaces. *Procedia Engineering*, 25:483–486, 2011.

- [101] Malay Ghosh. *Polyimides: fundamentals and applications*, p.759, volume 36. CRC Press, 1996.
- [102] DuPont, *Material Data Sheet Kapton*.
- [103] Parylene Coating Services Inc., *Material Data Sheet Parylene Version 2011*.
- [104] HD Microsystems, *Material Data Sheet PI-2600 Series, Version 2009*.
- [105] UBE Europe GmbH *Material Data Sheet UBE U-Varnish-S*.
- [106] Birthe Rubehn and Thomas Stieglitz. In vitro evaluation of the long-term stability of polyimide as a material for neural implants. *Biomaterials*, 31(13):3449–3458, 2010.
- [107] UBE Europe GmbH *Material Data Sheet Upilex25S*.
- [108] Martin Schubert, Sabine Kirsten, Tetiana Voitsekhivska, and Karlheinz Bock. Characterization of polymeric encapsulation for implantable microsystems applying dynamic fluidic and electrical load. In *Electronics Technology (ISSE), 2015 38th International Spring Seminar on*, pages 129–133. IEEE, 2015.
- [109] Sabine Kirsten, Martin Schubert, Jürgen Uhlemann, and Klaus-Jürgen Wolter. Characterization of ionic permeability and water vapor transmission rate of polymers used for implantable electronics. In *Engineering in Medicine and Biology Society (EMBC), 2014 36th Annual International Conference of the IEEE*, pages 6561–6564. IEEE, 2014.
- [110] Suehiro Sugitani, Takao Ishii, and Masami Tokumitsu. Improved moisture resistance for three-dimensional interconnects for mmic.
- [111] Suehiro Sugitani, Takao Ishii, and Masami Tokumitsu. Three-dimensional interconnect with excellent moisture resistance for low-cost mmics. *Advanced Packaging, IEEE Transactions on*, 26(2):133–140, 2003.
- [112] Joseph F Keithley. *The story of electrical and magnetic measurements: from 500 BC to the 1940s*. John Wiley & Sons, 1999.
- [113] Peter Fairley. *Electricity and magnetism*. Twenty-First Century Books, 2007.
- [114] Ken Gilmore. The capacitor: What it is, what it does, how it works. *Popular Electronics*, 11(4), April 1960. Accessed on 25.08.2017, www.rfcafe.com/references/popular-electronics.
- [115] Wayne M Saslow. *Electricity, Magnetism, and Light*. Academic press, 2002.

- [116] RimstarOrg. Dissectible capacitor/leyden jar - how it works. Accessed on 25.08.2017, www.youtube.com.
- [117] Michael Melloch. Leyden jar & dielectric breakdown. Accessed on 25.08.2017, www.youtube.com.
- [118] RimStarOrg. Electrostatic soap bubble science experiment. Accessed on 25.08.2017, www.youtube.com.
- [119] J Z Chen, A A Darhuber, S M Troian, and S Wagner. Capacitive sensing of droplets for microfluidic devices based on thermocapillary actuation. *Lab on a Chip*, 4(5):473–480, 2004.
- [120] Wolfram Mathworld. Laplace’s equation. Accessed on 25.08.2017, math-world.wolfram.com.
- [121] W Olthuis, W Streekstra, and P Bergveld. Theoretical and experimental determination of cell constants of planar-interdigitated electrolyte conductivity sensors. *Sensors and Actuators B: Chemical*, 24(1):252–256, 1995.
- [122] Wolfram Demonstrations Project. Electrostatic fields using conformal mapping. Accessed on 25.08.2017, demonstrations.wolfram.com.
- [123] Simon Ramo, John R Whinnery, and Theodore Van Duzer. *Fields and Waves in Communication Electronics– Third Edition*, JOHN WILEY&SONS. INC, 1993.
- [124] S Robinson and MC Escher. More mathematics than meets the eye. *SIAM News*, 35.
- [125] M.C. Escher Foundation. Mystery print of gallery solved: Escher and the droste effect. accessed on 25.08.2017, www.mcescher.com.
- [126] HarryCarry5. Escher’s print gallery explained. Accessed on 25.08.2017, www.youtube.com.
- [127] Wolfram Mathworld. Schwarz-christoffel mapping. Accessed on 25.08.2017, math-world.wolfram.com.
- [128] Daniel Fleisch. *A Student’s guide to Maxwell’s equations*. Cambridge University Press, 2008.
- [129] The Open Door Web Site. The relation between potential difference and electric field strength. accessed on 25.08.2017, www.saburchill.com, a reference source for both students and teachers.

- [130] Darren L. Weber. Eeg scalp current density and source current modelling notes. Accessed on 25.08.2017, psdlw.users.sourceforge.net/career.
- [131] Amedeo Troiano, Eros Pasero, and Luca Mesin. *A Road Ice Sensor*. INTECH Open Access Publisher, 2012.
- [132] Liesl K Massey. *Permeability properties of plastics and elastomers: a guide to packaging and barrier materials*. William Andrew, 2003.
- [133] A Schander, H Stemann, E Tolstosheeva, R Roese, V Biefeld, L Kempen, AK Kreiter, and W Lang. Design and fabrication of novel multi-channel floating neural probes for intracortical chronic recording. *Sensors and Actuators A: Physical*, 247:125–135, 2016.
- [134] Frederik Ceysens and Robert Puers. Insulation lifetime improvement of polyimide thin film neural implants. *Journal of neural engineering*, 12(5):054001, 2015.
- [135] David Rotermund, Jonas Pistor, Janpeter Hoeffmann, Tim Schellenberg, Dmitriy Boll, Elena Tolstosheeva, Dieter Gauck, Dagmar Peters-Drolshagen, Andreas K Kreiter, Martin Schneider, et al. Open hardware: Towards a fully-wireless sub-cranial neuro-implant for measuring electrocorticography signals. *bioRxiv*, page 036855, 2016.
- [136] Ming Yin, David A Borton, Juan Aceros, William R Patterson, and Arto V Nurmikko. A 100-channel hermetically sealed implantable device for chronic wireless neurosensing applications. *IEEE transactions on biomedical circuits and systems*, 7(2):115–128, 2013.
- [137] Gerald H Pollack. The fourth phase of water. *Ebner & Sons publishers, Seattle*, 2013.
- [138] E Tolstosheeva, E Barborini, EM Meyer, M Shafi, S Vinati, and W Lang. Micropatterning of nanoparticle films by bilayer lift-off. *Journal of Micromechanics and Microengineering*, 24(1):015001, 2013.
- [139] E Tolstosheeva, V Gordillo-González, T Hertzberg, L Kempen, I Michels, A Kreiter, and W Lang. A novel flex-rigid and soft-release ecog array. In *Engineering in Medicine and Biology Society, EMBC, 2011 Annual International Conference of the IEEE*, pages 2973–2976. IEEE, 2011.
- [140] Elena Tolstosheeva, Víctor Gordillo-González, Volker Biefeld, Ludger Kempen, Sunita Mandon, Andreas K Kreiter, and Walter Lang. A multi-channel, flex-rigid ecog micro-electrode array for visual cortical interfacing. *Sensors*, 15(1):832–854, 2015.
- [141] Elena Tolstosheeva, Volker Biefeld, and Walter Lang. Accelerated soak performance of bpda-ppd polyimide for implantable meas. *Procedia Engineering*, 120:36–40, 2015.

- [142] Elena Tolstosheeva, João V Pimentel, Andreas Schander, Ludger Kempen, Michael Vellekoop, and Walter Lang. Fabrication of parylene channels embedded in silicon using a single parylene deposition step. In *SPIE Microtechnologies*, pages 951811–951811. International Society for Optics and Photonics, 2015.
- [143] E Tolstosheeva, J Hoeffmann, J Pistor, D Rotermund, T Schellenberg, D Boll, T Hertzberg, V Gordillo-Gonzalez, S Mandon, D Peters-Drolshagen, et al. Towards a wireless and fully-implantable ecog system. In *Solid-State Sensors, Actuators and Microsystems (TRANSDUCERS & EUROSENSORS XXVII), 2013 Transducers & Eurosensors XXVII: The 17th International Conference on*, pages 384–387. IEEE, 2013.
- [144] A Schander, E Tolstosheeva, V Biefeld, L Kempen, H Stemmann, A Kreiter, and W Lang. Design and fabrication of multi-contact flexible silicon probes for intracortical floating implantation. In *Solid-State Sensors, Actuators and Microsystems (TRANSDUCERS), 2015 Transducers-2015 18th International Conference on*, pages 1739–1742. IEEE, 2015.
- [145] João Vitor Pimentel, Elena Tolstosheeva, Ludger Kempen, Walter Lang, and Michael J Vellekoop. An easy fabrication process of fully-sealed parylene microfluidic channels with a single deposition step. *Microsystem Technologies*, 22(7):1927–1932, 2016.
- [146] Thomas Hertzberg, Víctor Gordillo-González, Elena Tolstosheeva, Andreas Kreiter, and Walter Lang. Fabrication and characterization of different electrode configurations on neural probes. In *Proceedings MEA Meeting*, pages 366–367, 2012.
- [147] Janpeter Hoeffmann, Jonas Pistor, Dagmar Peters-Drolshagen, Elena Tolstosheeva, Walter Lang, and Steffen Paul. Biomedical-asic with reconfigurable data path for in vivo multi/micro-electrode recordings of bio-potentials. In *8th International Meeting on Substrate-Integrated Microelectrode Arrays Symposium (MEA Meeting)*, page 220, 2012.
- [148] Jonas Pistor, Janpeter Hoeffmann, David Rotermund, Elena Tolstosheeva, Tim Schellenberg, Dmitriy Boll, Victor Gordillo-Gonzalez, Sunita Mandon, Dagmar Peters-Drolshagen, Andreas Kreiter, et al. Development of a fully implantable recording system for ecog signals. In *Proceedings of the Conference on Design, Automation and Test in Europe*, pages 893–898. EDA Consortium, 2013.
- [149] Walter Lang, Frank Jakobs, Elena Tolstosheeva, Hannes Sturm, Azat Ibragimov, Antonia Kesel, Dirk Lehmkus, and Ursula Dicke. From embedded sensors to sensorial materials—the road to function scale integration. *Sensors and Actuators A: Physical*, 171(1):3–11, 2011.

- [150] Walter Lang, Dmitriy Boll, Elena Tolstosheeva, Azat Ibragimov, Konstantin Schubert, Christoff Brauner, and Christoph Pille. Embedding without disruption: The basic challenge of sensor integration. In *Sensors, 2012 IEEE*, pages 1–4. IEEE, 2012.

Appendices

Appendix A

ECoG MEA's Design

A.1 Bending of a Beam in an Arc

A beam subjected to a bending moment will experience stress due to bending. The stress will vary across the beam cross-section as illustrated in Fig.A.1A: the stress will be zero at the neutral axis of the beam, and it will linearly increase toward the beam edges.

A beam subjected to a bending moment will also experience a force F_s which will act normal to a section of area dA as indicated in Fig.A.1B. The force F_s can be expressed in terms of stress due to bending as follows:

$$F_s = \sigma_b dA = \frac{yE}{R} \cdot dA \quad (\text{A.1})$$

where y is the distance to the neutral axis, as shown in Fig.A.1B, E is the Young's modulus of the beam material and R is the radius of curvature.

Consequently, the total force F_t applied at the beam is the sum of the forces F'_s acting on all sections of the beam

$$F_t = \int \sigma_b dA = \frac{E}{R} \int y dA \quad (\text{A.2})$$

Using the above equation the following relation for the bending moment M applied at the beam is obtained

$$M = F_t \cdot y = \frac{E}{R} \underbrace{\int y^2 dA}_I = \frac{EI}{R} \quad (\text{A.3})$$

where I is the second moment of inertia, which implies the following relations

$$\frac{M}{I} = \frac{E}{R} = \frac{\sigma_b}{y} \quad (\text{A.4})$$

The value of I depends on the specific shape of the beam and the position of the neutral

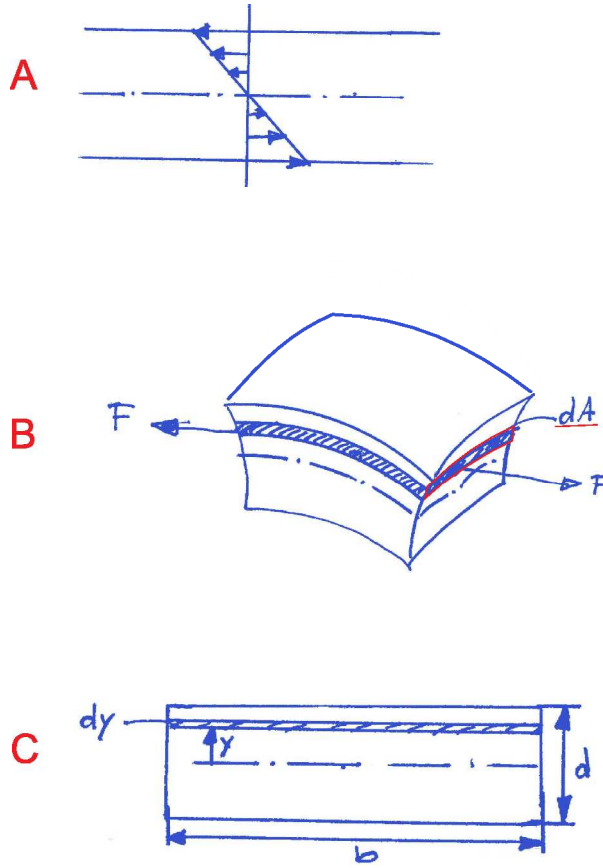


Figure A.1: (A) Bending stress variation across a beam cross-section subjected to a bending moment; (B) Bending force applied at a beam portion. (C) A rectangular beam cross-section [79].

axis. For a regular cross-section, as illustrated in Fig.A.1C, the value of I can be derived as follows

$$I = \int y^2 dA = \int y^2 b dy = b \int_{-d/2}^{d/2} y^2 dy = b \left[\frac{d^3}{24} + \frac{d^3}{24} \right] = \frac{b d^3}{12} \quad (\text{A.5})$$

where b is the width of the beam cross-section and d is its thickness, as illustrated in Fig.A.1C.

The above relation implies a corresponding bending moment M

$$M = \frac{E}{R} \cdot \frac{b d^3}{12} \quad (\text{A.6})$$

which in turn can be used to define the flexibility of a beam $\frac{1}{MR}$ as follows

$$\frac{1}{MR} = \frac{12}{E b d^3} \quad (\text{A.7})$$

i.e. the flexibility of a beam is mostly influenced by its thickness d .

A.2 Electrode Layout of the ECoG MEA

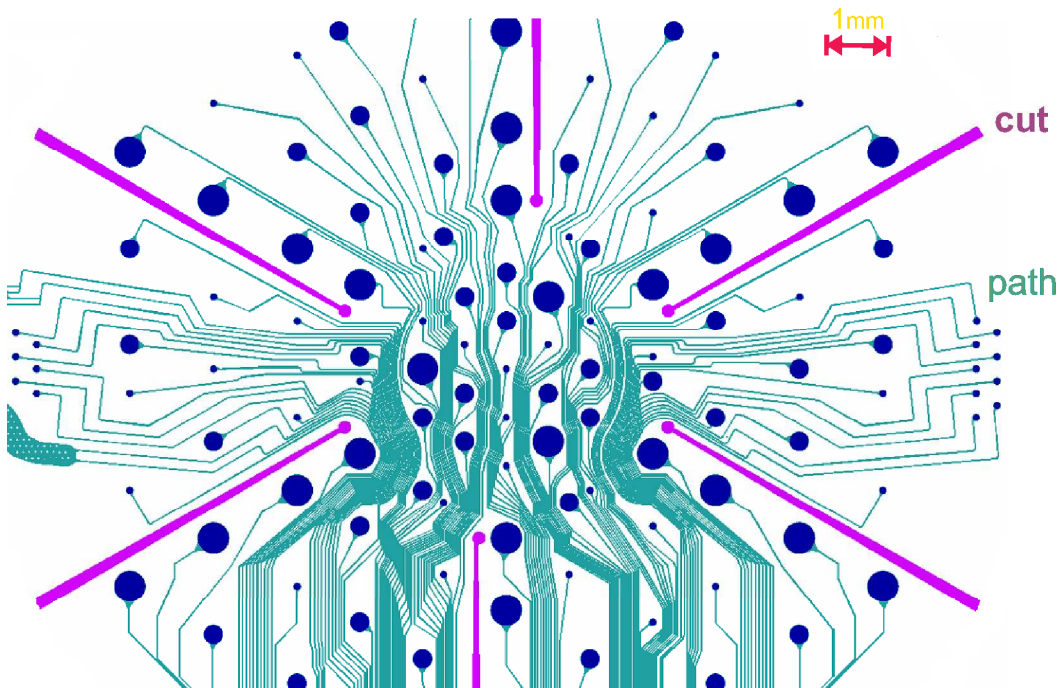


Figure A.2: ECoG MEA layout: circular electrodes and their connection paths. Most paths are squeezed in the middle of the array to allow the integration of several radial cuts. The radial cuts enable the MEA to obtain a foldless hemispherical shape.

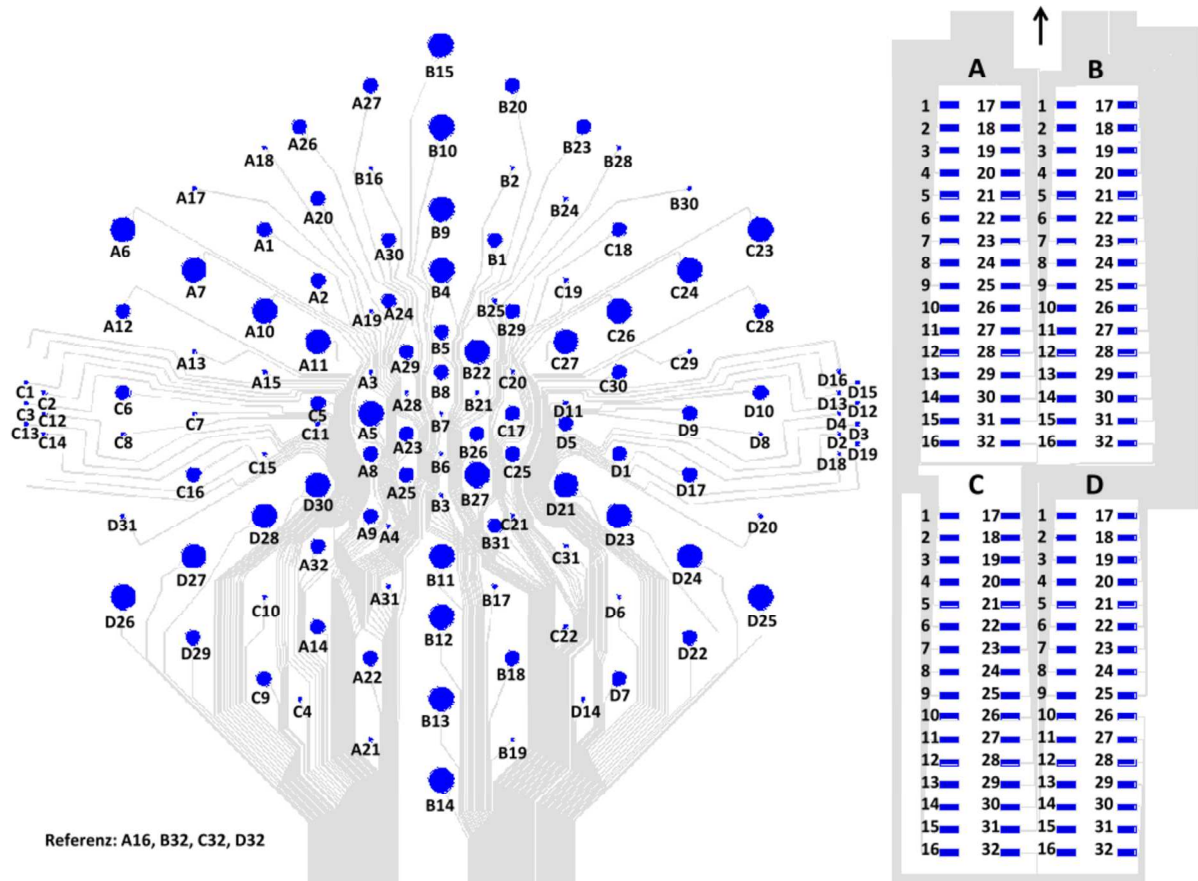


Figure A.3: ECoG MEA layout: each electrode (left) is mapped to a specific pad on the connector (right).

Appendix B

ECoG MEA's Microfabrication Flow

Schritt	Bereich	Prozess	Bemerkung
1	LOS GRUENDE	<100> 100mm, 525µm SSP	
2	LOS GRUENDE	<100> 100mm, 380µm DSP	
3	OT	Thermisches Oxid (feucht), 1000 nm	750nm Isolation (Vorderseite) und Maske für Rückseitenätzung
4	FL	PR 1,8 µm, Gesamtprozess	Rückseite, Strukturierung Oxid. Maske: ET_Silizium Ti-Prime aufspinnen, Ausheizen nicht erforderlich #1, AZ1518, 1,8µm 30min @ 90°C oder 100°C, 110sec 3s @ 12mW/cm², Hartkontakt # "K" Ausheizen nicht erforderlich mit schmalen Abdeckring process: "oxid", 5mTorr, t=7min
5	DRIE	Oxid, 1000 nm, STS	
6	NC	Lackentfernung, AZ 100 Remover	T = 50°C t = 15min
7	NC	Reinigung, Carosche Säure	
8	FL	Polyimid, Gesamtprozess	1) Haftvermittler 100ml H2O + 0,1ml HD in 250ml-Kolben mischen Hotplate 120°C, 120sec mit Prog12 auf HB aufspinnen Hotplate 120 °C, 120sec 2) Polyimid Chuck und Hotplate auf Verunreinigungen prüfen rechter Belacker, Prog"3" Exsikator, 7min bei 80°C auf Hotplate legen, dann setpoint 120°C und Uhr mit 10min starten Ausheizen im Bonder ! (Vakuum) Temp. Pl. VB
9	FL	PR 10,0 µm, Gesamtprozess SoT	Rückseitenjustage "D2" Schlüssel/Schlüssel Maske: PL_Step descum: prog "14" AZ9260, prog "7" 30min @ 90°C, min. 60min Rehydrieren 80s @ 12mW/cm² prog "G" Ausheizen zum Abschrägen der Lackflanke !!! 60min @ 120°C
10	DRIE	Polyimid	schmalen Abdeckring process: polyimid ca. 11min Oxiddicke in den geöffneten Bereichen kontrollieren
11	NC	Lackentfernung, AZ 100 Remover	T = 50°C t = 15min
12	PVD	Titan, 50nm, Balzers	1) Ausheizen HotPlate 120°C, 120sec 2) Barrel Prog "14" 3) 20nm auf Polyimid, schmaler Rand Programm: ti_15.tec OHNE Sputterätzen 200W Sputterleistung, 72sec
13	PVD	Gold, 500nm, Balzers	300nm Programm: Au_80.tec OHNE Sputterätzen 100W Sputterleistung, t = 174sec

14	FL	PR 1,8 µm, Gesamtprozess	descum, Barrel Prog "14" #3, AZ1518, 3,9µm 30min @ 90°C 12s @ 12mW/cm² 1x "K" KEIN Ausheizen, da Mikroform für Galvanik
15	GALVANIK	Gold, 1-5 µm	kein Ausheizen freiliegendes Gold im Randbereich mit AZ1518 dünn abpinseln, kurzes Ausheizen auf Hotplate bei 70°C descum Prog "14" Plater 2 2mA preset 0,2 auf Zeit: t=20min
16	NC	Lackentfernung, AZ 100 Remover	T = 50°C t = 5min
17	FL	PR 3,9 µm, Gesamtprozess	Vorderseitenjustage, Maske: Au_on_PiStep Strukturierung der Leiterbahnen descum prog "14" #3, AZ1518, 3,9µm 30min @ 90°C 14sec @ 12mW/cm² 1x "K"
18	NC	Au Etch 200	descum, Prog "14" T = 50°C t = ca. 3-4 min Ätzung auf Sicht
19	NC	Oxide Etch 7: 1, modified	Ti-Haftschrift ätzen
20	NC	Lackentfernung, AZ 100 Remover	
21	FL	Oberflächenreinigung nach Litho Barrel (Descumming)	Ausheizen + descum prog "14"
22	FL	Polyimid, Gesamtprozess	1) Haftvermittler 100ml H2O + 0,1ml HD in 250ml-Kolben mischen Hotplate 120°C, 120sec mit Prog12 auf HB aufspinnen Hotplate 120 °C, 120sec 2) Polyimid Chuck und Hotplate auf Verunreinigungen prüfen rechter Belacker, Prog"3" Excikator, 7min bei 80°C auf Hotplate legen, dann setpoint 120°C und Uhr mit 10min starten Ausheizen im Bonder ! (Vakuum) Temp. Pl_VB
23	FL	PR 10,0 µm, Gesamtprozess SoT	Maske: Pl_on_AuPiStep descum: prog "14" AZ9260, prog "7" 30min @ 90°C, min. 60min Rehydrieren 80s @ 12mW/cm² prog "G"
24	DRIE	Polyimid	
25	NC	Lackentfernung, AZ 100 Remover	

26	FL	PR 10,0 μm , Gesamtprozess SoT	Maske: PI_new descum: prog "14" AZ9260, prog "7" 30min @ 90°C. min. 60min Rehydrieren 80s @ 12mW/cm ² prog "G"
27	DRIE	Polyimid	
28	NC	Lackentfernung, AZ 100 Remover	
29	FL	PR 10,0 μm , Gesamtprozess SoT	Maske: ET_Silizium descum: prog "14" AZ9260, prog "7" 30min @ 90°C. min. 60min Rehydrieren 80s @ 12mW/cm ² prog "G"
30	DRIE	Mono-Si-trench, 380 μm STS	
31	NC	Lackentfernung, AZ 100 Remover	
32	NC	Oxide Etch 7: 1, modified	

Appendix C

Resist Reflow

A tapered slope can be realized first in photoresist by resist reflow and transferred into polyimide by RIE-plasma etching. The reflow properties of two photoresists (AZ9260 and AZ4562) were investigated. A target thickness of 10 μm was set, because it is sufficient to etch a 5 μm -thick polyimide in an $\text{O}_2 + \text{CF}_4$ RIE-plasma. The wafers were cleaned in Caro's acid and coated with TiPrime, to ensure better Si-photoresist adhesion. AZ9260 was spin-coated at 2000rpm and AZ4560 at 1850 rpm. All samples were soft-baked for 30min@90°C and let rehydrate for 1h. The samples were exposed for 80s and 40 s, respectively, at 12 mWatt/cm² and developed in AZ726 MIF. One sample was exposed to O_2 plasma. The resist reflow was performed in an oven for 1h at 90°C and 120°C. The step widths, acquired by profilometry, are presented in Tables A. AZ9260 has better resist reflow behaviour than AZ4560, most probably due to lower viscosity. Exposure to an O_2 plasma increases the step width from 26 to 42 μm , while resist reflow at 120°C results in a 70 μm width. Thus higher temperature bake has higher influence on reflow than O_2 plasma.

Next, the influence of O_2 plasma on the AZ9260 reflow was tested. A 500 nm-thick thermal oxide was grown on a silicon wafer. The wafer was coated with a HD adhesion promoter (VM-651), and polyimide U-Varnish was spin-coated at 300 rpm. The polyimide was soft-baked at 120°C for 10 min and cured at 450°C in N_2 atmosphere. The polyimide surface was shortly exposed to O_2 plasma in order to improve the adhesion. Then this photoresist was spun on the polyimide and treated same as the previous samples. AZ 9260 was reflowed at 120°C, whereas two of the samples were treated with a short O_2 plasma beforehand. The step-width of a reflowed AZ9260 resist on polyimide for 1h@120°C is 65 μm . Oxygen plasma treatment slightly increased the step-width to 69 μm . However, in the microfabrication flow of the electrode arrays, we omitted oxygen plasma, because of bubble formation in some samples observed directly after the plasma treatment. We transferred the reflow profile into polyimide by etching half of the layer for 5 min in $\text{O}_2 + \text{CF}_4$ RIE-plasma. Half of the samples we treated further in AZ100 to

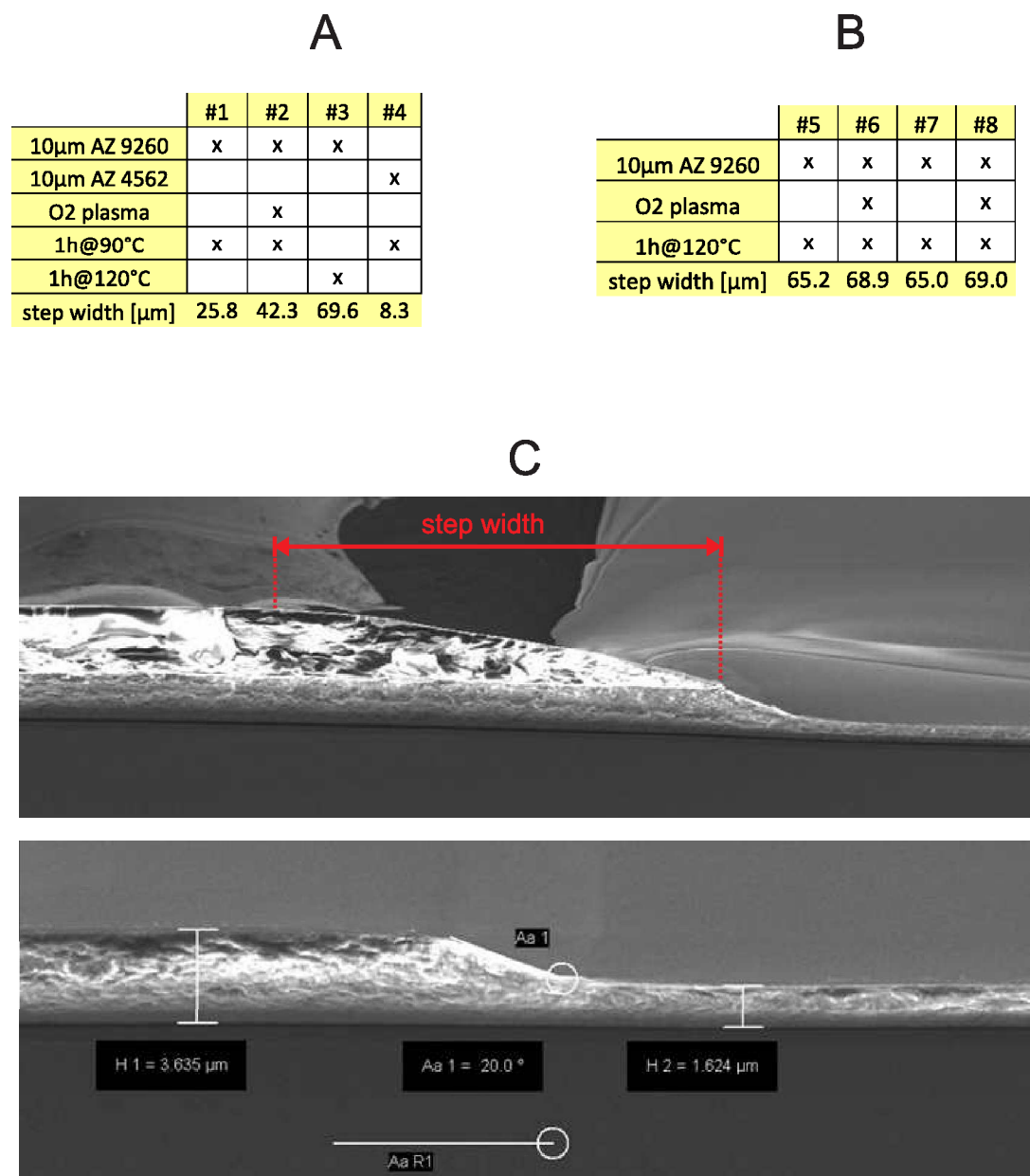


Figure C.1: Reflow of photoresist to achieve a tapered profile in polyimide: (Table A) Reflow Results 1, (Table B) Reflow Results 2, (Top SEM image) Reflowed photoresist, (Bottom SEM image) tapered profile of polyimide.

remove the reflowed photoresist. The slope angle of polyimide slope is 20 µm.

Appendix D

Pull Tests

Pull tests were conducted to investigate the mechanical strength of the soldering pads. Samples were prepared with Si/SiO₂/PI/TiAu and Si/SiO₂/TiAu configurations. Omnetics connectors were soldered. Pull forces of 5 N and 12.9 N were obtained, respectively. Solder-joints of Si/SiO₂/TiAu samples broke at the SiO₂-TiAu interface, while the Si/SiO₂/PI/TiAu samples broke at the PI-TiAu interface. Three samples were prepared as shown in Fig.D.1. The force required to pull a female connector out of its male counterpart (32-pin) was measured with the first sample to be ca. 12 N. The force a 32-pin soldered connector can sustain before fracture was determined with the second sample to be 29 N, which corresponds to 10.7 MPa tensile stress distributed over a single soldering pad of $160 \times 520 \mu\text{m}^2$ area. In practice, the connector will be fixed with UHU adhesive, which can sustain 170 N force before fracture (surface area of sample/UHU interface ca. 50 mm²). Additional adhesion tests performed with scotch tape revealed that the adhesion of Si/SiO₂/TiAu decreases when it is exposed to elevated temperature as in case of polyimide curing peak of 450°C.

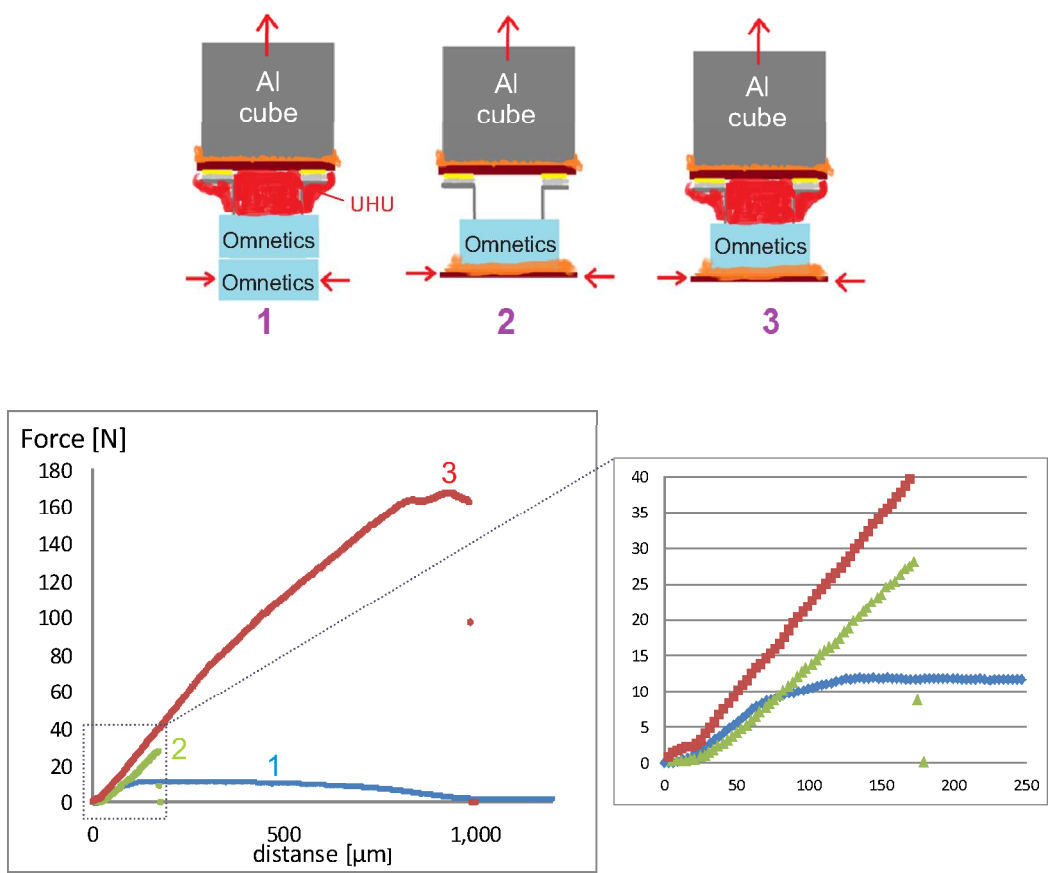


Figure D.1: Pull tests performed on Si/SiO₂/TiAu samples.

Appendix E

Long-Term Stability of Polyimide

E.1 E-Field Distribution of Coplanar-Plate Capacitor

The E-field distribution is not uniform along the y -axis: it is max at $y = 0$ and decreases for larger y -values. An expression for this distribution at $x = 0$ can be obtained by using Eq.5.30. The equipotentials, represented by u' -hyperbola (see Fig.5.9), run parallel to y , hence $\frac{\partial u'}{\partial y} = 0$ which results in

$$\partial y = -a \cdot \sin u'' \cdot \frac{\partial (\sinh v'')}{\partial y} \Leftrightarrow -\frac{\partial v'}{\partial y} = \frac{2V_0}{a\pi} \cdot \frac{1}{\cosh\left(\frac{\pi}{2V_0}v'\right)} \quad (\text{E.1})$$

using the fact that for $x = 0$ $u' = 0$ and substituting back $u'' = \frac{\pi(V_0 - u')}{2V_0}$ and $v'' = \frac{\pi}{2V_0}$ from Eq.5.27.

Expressing cosh in terms of y gives

$$y = a \cdot \sinh v'' = a \cdot \sqrt{\cosh v'' - 1} \Rightarrow \cosh v'' = \left(\frac{y}{a}\right)^2 + 1 \quad (\text{E.2})$$

and

$$-\frac{\partial v'}{\partial y} = \frac{2V_0}{a\pi} \cdot \frac{1}{\left(\frac{y}{a}\right)^2 + 1} \quad (\text{E.3})$$

As $\epsilon_0 v$ relates to the flux function in $[C/m]$ [123], therefore $\partial v'/\partial y$ is the distribution of electrical flux along the y -axis. This distribution is plotted for different inter-plate distances in Fig.5.11, right image.

E.2 Hands on Measurements of IDE sensors

To establish a proper measurement configuration for the IDE-samples, two impedance paths – lateral Z_{lat} and vertical Z_v – were measured (see Fig.E.1A): Z_{lat} corresponds to the coplanar capacitance of the IDE micro-structures and upon water diffusion is an inverse measure for the crosstalk between the IDE electrodes [95]. The vertical impedance Z_v corresponds to signal attenuation due to "shunting", provided the water medium is connected to ground [95]. These impedances were tracked in the course of one week on a polyimide-covered IDE sample, soaked in saline and kept at 60°C. Z_{lat} declined more rapidly than Z_v , as shown in Fig.E.1, corresponding to results reported in literature [95]. These results imply that volume diffusion of water into the polyimide coating is one of the reasons for the formation of the observed short-circuited electrode in the *in-vivo* array tests.

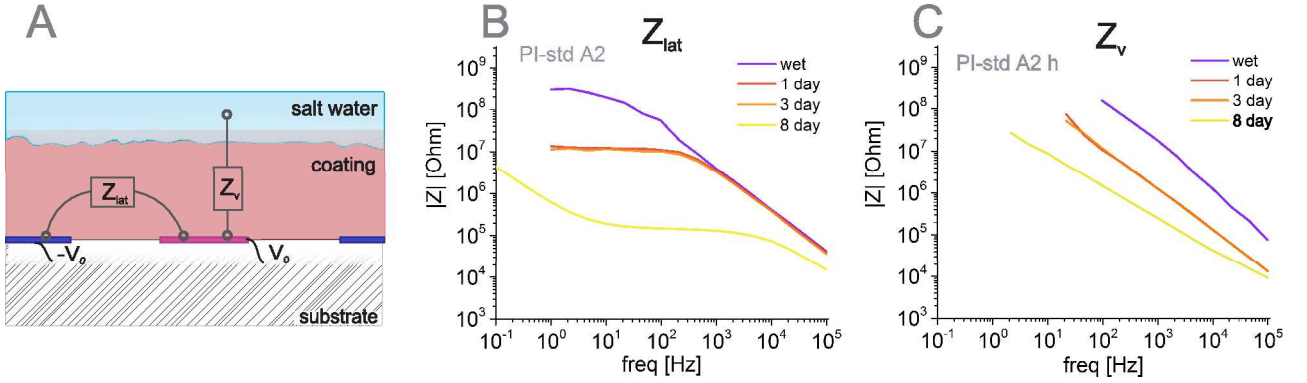


Figure E.1: (A) Electrical tests of an IDE sensor: lateral Z_{lat} and vertical Z_v impedance paths, adopted from [95]; (B) Z_{lat} and (C) Z_v of a polyimide-coated IDE sensor, with Z_{lat} being much more sensitive to water diffusion than Z_v .

E.3 Long-term Stability of Parylene vs. Polyimide

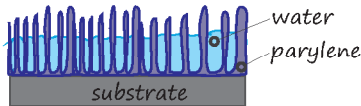
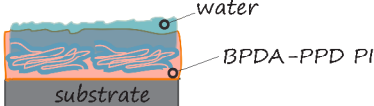
	Parylene C	BPDA-PPD PI
adhesion promoter	Silane-A174 or AdProPoly*	VM 651**
substrate surface	particles -> loss of water-barrier	particles -> no influence on water-barrier
T° stability	200°C -> loss of water-barrier	high T° stability (PI cured up to 450°C)
film thickness	water-barrier independent of film thickness (5µm & 15µm)	5µm thickness offers an excellent water-barrier
film morphology		

Figure E.2: Water-barrier properties of Parylene C vs. BPDA-PPD Polyimide, *adhesion promoter developed by SCS Coatings, **organosilane adhesion promoter developed by DuPont. The morphology of the parylene C film was adopted from a SCS Workshop on Parylene.

E.4 Hands on Inter-Electrode Impedance Measurements

Provided water diffuses into the MEA and a parasitic current path is formed e.g. between two neighbouring electrodes, what is the best way to measure the parasitic impedance of this path? To answer this question, two test scenarios were considered, which are illustrated in Fig.E.5:

- **test scenario A** an external Pt wire is used a counter electrode and a MEA electrode as a reference; when they are connected to an impedance meter (see left image) the impedance Z_{el2} is measured¹ along the path of i_{main} ; once water diffuses into the polyimide coating, a parasitic current i_p arises across the series impedance $Z_{el1} + Z_p$. This parasitic current can be expressed as follows

$$i_p^A = \frac{Z_{el2}}{Z_{el1} + Z_p} \cdot i_{main} \quad (E.4)$$

- **test scenario B** one MEA electrode is used as a counter and another MEA electrode as a reference. The impedance along the path of i_{main} is measured (see right image) and the parasitic current i_p across Z_p can be expressed as

$$i_p^B = \frac{Z_{el2} + Z_{el1}}{Z_p} \cdot i_{main} \quad (E.5)$$

Provided $Z_{el1} \approx Z_{el2} = Z$, then $i_p^A < i_p^B$, which implies test scenario B as more appropriate method to measure the formation of parasitic short-circuits upon water diffusion.

This implication was tested in practice as follows: discrete resistances were linked with wires to the pins of a MEA Omnetics connector, thus bridging every two MEA electrodes² (R_p in Fig.E.3). The change in impedance due to a bridging resistance was measured in both test scenario A and B, as shown in Fig.E.3: impedance measurements obtained from two MEA electrodes, both $100\mu\text{m}$ in diameters, confirm test scenario B as a more sensitive measurement method e.g. a $22\text{M}\Omega$ resistor induces a measurable change in both magnitude and phase plots (see right image).

Next, when the impedance between larger MEA electrodes – $500\mu\text{m}$ and the MEA own reference electrode – were measured, the sensitivity of both test scenarios dropped e.g. only resistances below $1\text{M}\Omega$ resistor induced change in the impedance plots of test scenario B (see right plots in Fig.E.4). This observation is explained as follows: MEA electrodes of larger surface area posses lower electrode-electrolyte impedances and higher amount of current (main current) passes through them; when a parasitic current arises, it is partially “shunted” by the main current.

¹Here the Pt-electrolyte impedance and saline resistance are both neglected.

²Ohmic resistances were chosen for the sake of simplicity; discrete capacitors were also tested but had a negligible influence on the total impedance.

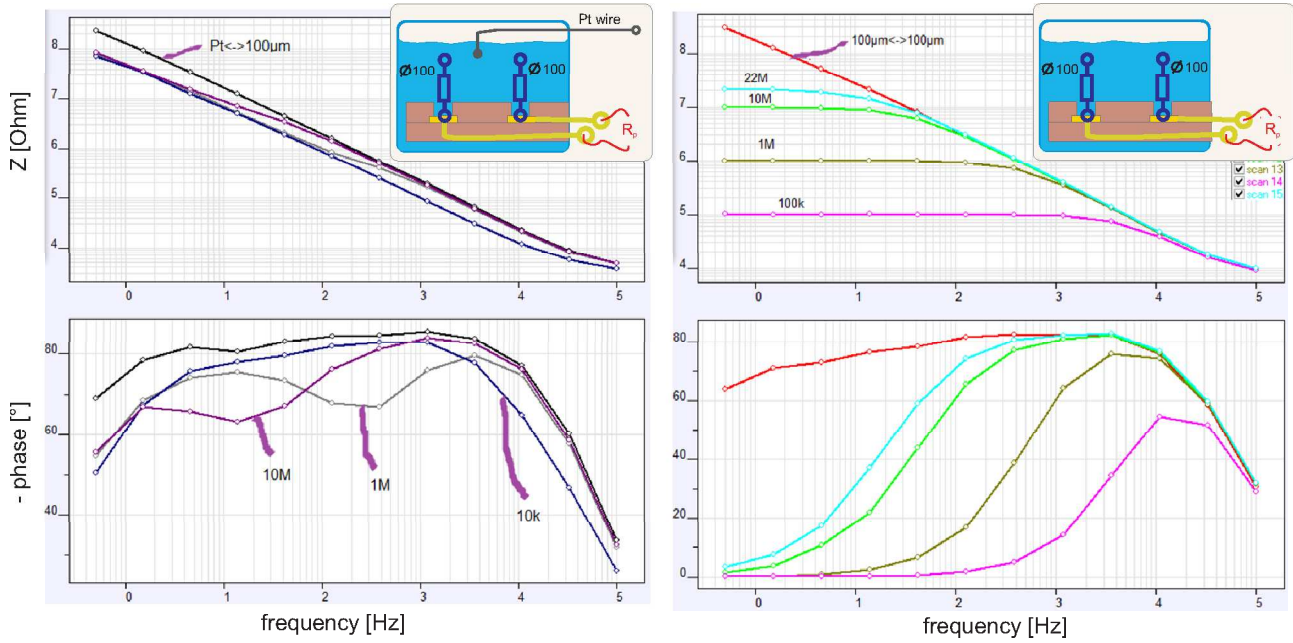


Figure E.3: Magnitude and phase plots of two MEA electrodes (both $100\mu\text{m}$ in diameter), when a bridging resistor R_p was introduced in order to simulate parasitics. The resistor value of R_p was varied from $22\text{M}\Omega$ to $10\text{k}\Omega$. The impedances were measured in two different test scenarios (compare with Fig.E.5). The test scenario used in the right plot (B in Fig.E.5) is more sensitive e.g. a $22\text{M}\Omega$ resistor induces a measurable change in both magnitude and phase plots.

In short, test scenario B is more sensitive than A with respect to the introduction of bridging resistances, as confirmed by both theory and practice. It should be kept in mind, however, that when measuring electrode pairs of larger surface area (as in the case of $500\mu\text{m}$ and the MEA reference) and therefore lower impedances, parasitics of resistance values $> 1\text{M}\Omega$ will not be traceable.

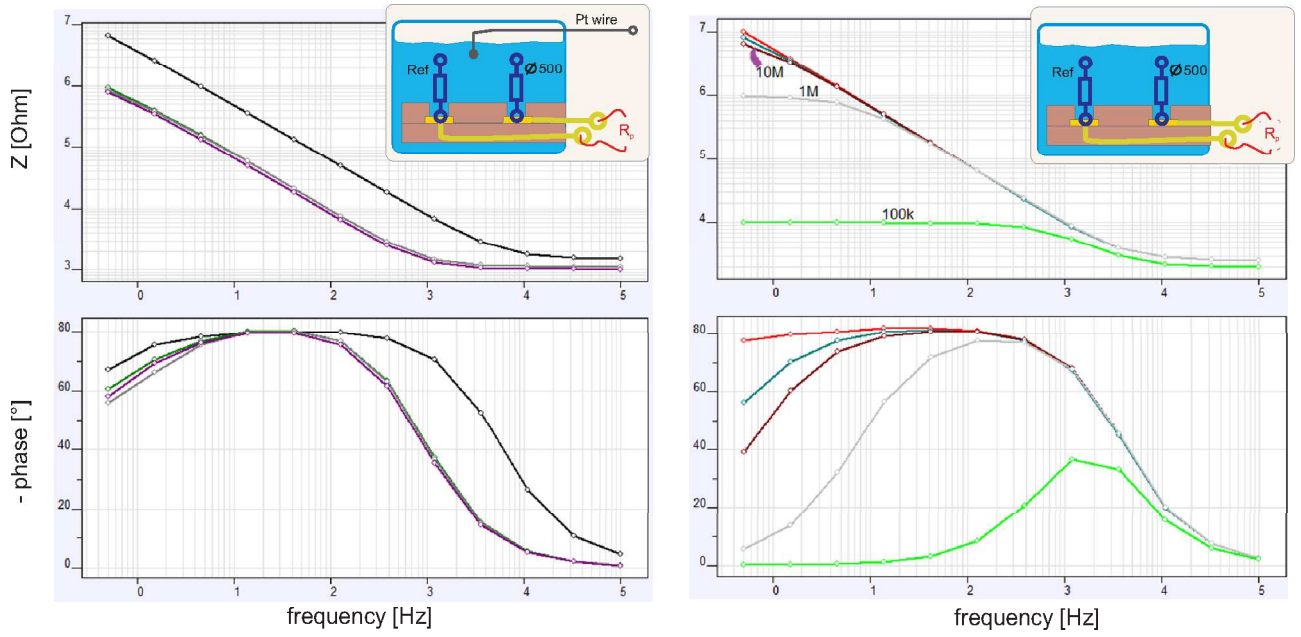


Figure E.4: Magnitude and phase plots of two MEA electrodes (a 500 μ m-one and the MEA reference). Resistor R_p simulated a parasitic path. The impedances were measured in two different test scenarios (see Fig.E.5). The scenario of the right plot (B in Fig.E.5) is more sensitive.

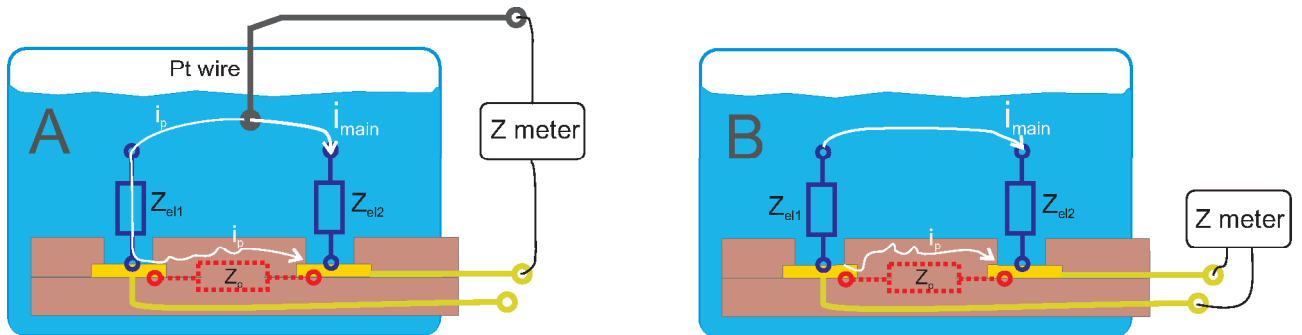


Figure E.5: Optimal sensing of inter-electrode impedances: (A) across a Pt-wire and a MEA-electrode; (B) between two MEA-electrodes.

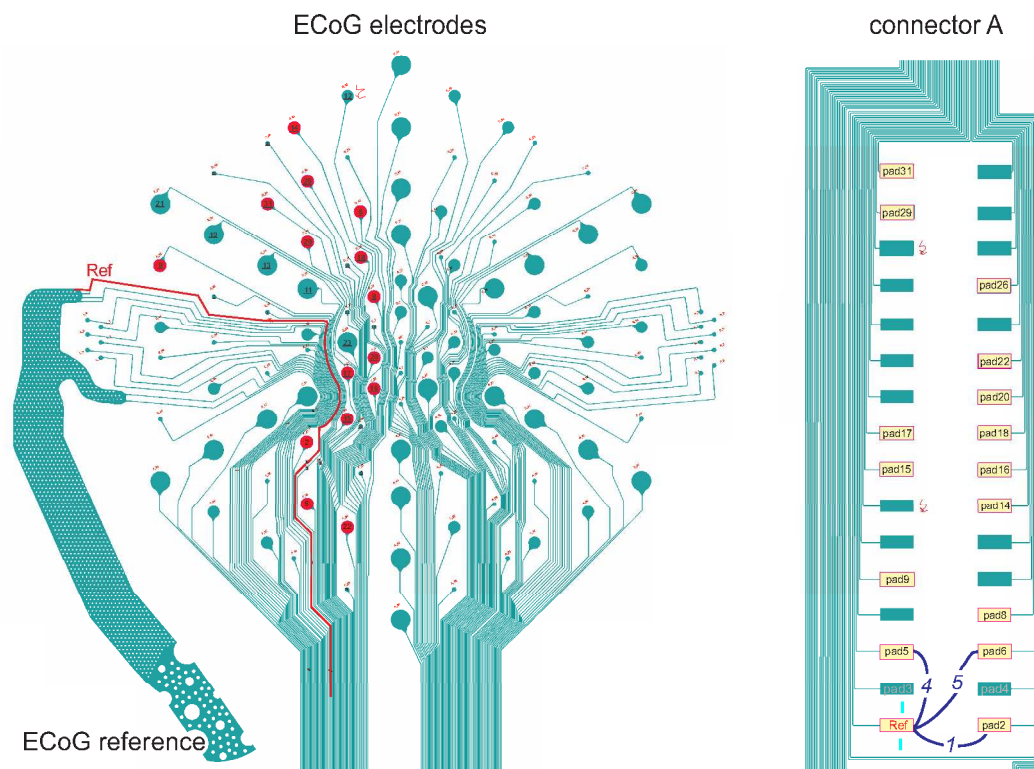


Figure E.6: ECoG MEA layout: 300 μ m-type electrodes belonging to connector “A” plus the reference electrode.

Appendix F

Author's Publication List

- E Tolstosheeva, E Barborini, EM Meyer, M Shafi, S Vinati, and W Lang. Micropatterning of nanoparticle films by bilayer lift-off. *Journal of Micromechanics and Microengineering*, 24(1):015001, 2013
- E Tolstosheeva, V Gordillo-González, T Hertzberg, L Kempen, I Michels, A Kreiter, and W Lang. A novel flex-rigid and soft-release ecog array. In *Engineering in Medicine and Biology Society, EMBC, 2011 Annual International Conference of the IEEE*, pages 2973–2976. IEEE, 2011
- Elena Tolstosheeva, Víctor Gordillo-González, Volker Biefeld, Ludger Kempen, Sunita Mandon, Andreas K Kreiter, and Walter Lang. A multi-channel, flex-rigid ecog micro-electrode array for visual cortical interfacing. *Sensors*, 15(1):832–854, 2015
- Elena Tolstosheeva, Volker Biefeld, and Walter Lang. Accelerated soak performance of bpda-ppd polyimide for implantable meas. *Procedia Engineering*, 120:36–40, 2015
- Elena Tolstosheeva, João V Pimentel, Andreas Schander, Ludger Kempen, Michael Vellekoop, and Walter Lang. Fabrication of parylene channels embedded in silicon using a single parylene deposition step. In *SPIE Microtechnologies*, pages 951811–951811. International Society for Optics and Photonics, 2015
- E Tolstosheeva, J Hoeffmann, J Pistor, D Rotermund, T Schellenberg, D Boll, T Hertzberg, V Gordillo-Gonzalez, S Mandon, D Peters-Drolshagen, et al. Towards a wireless and fully-implantable ecog system. In *Solid-State Sensors, Actuators and Microsystems (TRANSDUCERS & EUROSENSORS XXVII), 2013 Transducers & Eurosensors XXVII: The 17th International Conference on*, pages 384–387. IEEE, 2013

- A Schander, E Tolstosheeva, V Biefeld, L Kempen, H Stemmann, A Kreiter, and W Lang. Design and fabrication of multi-contact flexible silicon probes for intracortical floating implantation. In *Solid-State Sensors, Actuators and Microsystems (TRANSDUCERS), 2015 Transducers-2015 18th International Conference on*, pages 1739–1742. IEEE, 2015
- João Vitor Pimentel, Elena Tolstosheeva, Ludger Kempen, Walter Lang, and Michael J Vellekoop. An easy fabrication process of fully-sealed parylene microfluidic channels with a single deposition step. *Microsystem Technologies*, 22(7):1927–1932, 2016
- Thomas Hertzberg, Víctor Gordillo-González, Elena Tolstosheeva, Andreas Kreiter, and Walter Lang. Fabrication and characterization of different electrode configurations on neural probes. In *Proceedings MEA Meeting*, pages 366–367, 2012
- A Schander, H Stemmann, E Tolstosheeva, R Roese, V Biefeld, L Kempen, AK Kreiter, and W Lang. Design and fabrication of novel multi-channel floating neural probes for intracortical chronic recording. *Sensors and Actuators A: Physical*, 247:125–135, 2016
- Janpeter Hoeffmann, Jonas Pistor, Dagmar Peters-Drolshagen, Elena Tolstosheeva, Walter Lang, and Steffen Paul. Biomedical-asic with reconfigurable data path for in vivo multi/micro-electrode recordings of bio-potentials. In *8th International Meeting on Substrate-Integrated Microelectrode Arrays Symposium (MEA Meeting)*, page 220, 2012
- Jonas Pistor, Janpeter Hoeffmann, David Rotermund, Elena Tolstosheeva, Tim Schellenberg, Dmitriy Boll, Victor Gordillo-Gonzalez, Sunita Mandon, Dagmar Peters-Drolshagen, Andreas Kreiter, et al. Development of a fully implantable recording system for ecog signals. In *Proceedings of the Conference on Design, Automation and Test in Europe*, pages 893–898. EDA Consortium, 2013
- David Rotermund, Jonas Pistor, Janpeter Hoeffmann, Tim Schellenberg, Dmitriy Boll, Elena Tolstosheeva, Dieter Gauck, Dagmar Peters-Drolshagen, Andreas K Kreiter, Martin Schneider, et al. Open hardware: Towards a fully-wireless sub-cranial neuro-implant for measuring electrocorticography signals. *bioRxiv*, page 036855, 2016
- Walter Lang, Frank Jakobs, Elena Tolstosheeva, Hannes Sturm, Azat Ibragimov, Antonia Kesel, Dirk Lehmhus, and Ursula Dicke. From embedded sensors to sensorial materials—the road to function scale integration. *Sensors and Actuators A: Physical*, 171(1):3–11, 2011

- Walter Lang, Dmitriy Boll, Elena Tolstosheeva, Azat Ibragimov, Konstantin Schubert, Christoff Brauner, and Christoph Pille. Embedding without disruption: The basic challenge of sensor integration. In *Sensors, 2012 IEEE*, pages 1–4. IEEE, 2012